

# Benchmarking of Computational Fluid Dynamics for multiphase flows in pipelines

MSC THESIS

DELFT UNIVERSITY OF TECHNOLOGY  
FACULTY OF APPLIED SCIENCES  
DEPARTMENT OF MULTI-SCALE PHYSICS

*Author:*

Mahinder RAMDIN  
Student number: 1396099  
Start: September 2009  
End: October 2010

*Supervisor:*

Prof. dr. ir. R.A.W.M. HENKES

*Reviewers:*

Prof. dr. ir. R.A.W.M. HENKES  
Prof. dr. ir. R.F. Mudde  
Dr. S. Kenjereš, Dipl.-Ing  
Ir. L.J.A.M. van Campen

October 14, 2010



---

# Summary

The current design of multiphase flow through pipelines is based on one-dimensional steady state or dynamic simulation methods. However, there is an increasing interest from a wide range of industries to use Computational Fluid Dynamics (CFD) codes for design purposes. Recently some journal papers were published, which claim that current commercial CFD codes are able to predict the different multiphase flow regimes in a horizontal two phase flow. Due to the complexity of multiphase flows and the lack of fundamental understanding of these kind of flows, CFD could be very advantageous. However, the question is whether existing CFD codes are indeed reliable enough to model such multiphase flows.

Consequently the present study was started to investigate the reliability of a selected commercial CFD code, FLUENT, to model multiphase flow in pipelines. For this assessment two benchmark cases were considered. The first benchmark case was the simulation of the Benjamin bubble, which is a single bubble moving into a stagnant liquid in a *horizontal* pipe or channel. Secondly, the Dumitrescu or the Taylor bubble was modeled. This is a single bubble, which rises in a stagnant liquid in a *vertical* pipe. The reason for specifically selecting these two benchmark cases is twofold. Firstly both cases are closely related to the slug flow regime, which is a common flow regime in pipelines found in the oil and gas industry. Secondly analytical solutions exist for the two benchmark cases when the effect of viscosity and the effect of surface tension are neglected, which makes the assessment more straightforward.

The Volume of Fluid (VOF) multiphase model, implemented in FLUENT, was used to model the benchmark cases. Both 2D and 3D simulations were performed and the simulation results were compared with the analytical solutions and with experimental data from the literature. For convenience the simulation results for the Benjamin bubble and the Dumitrescu/Taylor bubble are summarized separately.

## Summary of the simulation results for the Benjamin bubble

The analytical value for the dimensionless bubble velocity and the dimensionless liquid height for the 2D channel flow was derived by Benjamin (1968) to be  $v_b/\sqrt{gH} = 0.5$  and  $y/H = 0.5$ , respectively. The FLUENT simulations for the 2D Benjamin bubble with zero viscosity and zero surface tension with the finest grid gave a dimensionless bubble velocity of  $v_b/\sqrt{gH} = 0.494$ , where  $v_b$  is the bubble velocity,  $g$  the gravitational acceleration and  $H$  the channel height. This value for the dimensionless bubble velocity is in good agreement with the analytical value of 0.5. The corresponding dimensionless liquid height, which is the thickness of the liquid layer beneath the bubble, was  $y/H = 0.495$ . The latter is also in very good agreement with the theoretical value of 0.5. Benjamin (1968) also derived an analytical expression for the dimensionless bubble velocity and the dimensionless liquid height for the 3D pipe flow when the flow was inviscid and the effect of surface tension was neglected. The analytical value for the dimensionless bubble velocity and the dimensionless liquid height was given by Benjamin (1968) to be  $v_b/\sqrt{gD} = 0.542$  and  $y/D = 0.563$ , respectively. In the latter  $D$  is the diameter of the pipe. The FLUENT simulations for the 3D Benjamin bubble with zero viscosity and zero surface tension with the finest grid gave a dimensionless bubble velocity of  $v_b/\sqrt{gD} = 0.516$ . This value is in fair agreement with the analytical value of 0.542. The corresponding dimensionless liquid height was  $y/D = 0.551$ , also in good agreement with the analytical value of 0.563. Extrapolation of the simulation results to a zero grid size gives a value of 0.531 and 0.554 for the dimensionless bubble velocity and the dimensionless liquid height, respectively. Thus the simulation results are in good agreement with the analytical solutions of Benjamin (1968).

In addition to these special conditions of zero viscosity and zero surface tension, simulations were performed to investigate the effect of viscosity and surface tension on the 2D and 3D Benjamin bubbles. Several simulations, with corresponding experimental conditions from the literature, were performed. The dimensionless number used in this study to account for surface tension was either the Eötvös number  $Eo = \rho g L^2 / \sigma$  or the inverse Eötvös number defined as  $\Sigma = 4\sigma / \rho g L^2$ . The dimensionless numbers used to account for the viscous effects were either the Morton number  $Mo = g \mu^4 / \rho \sigma^3$  or the Reynolds number defined as either  $Re = \rho v_b L / \mu$  or as  $Re = \rho L \sqrt{g L} / \mu$ . The dimensionless number to account for inertial effects was the Froude number defined as  $v_b / \sqrt{g L}$ . In these equations  $\rho$  and  $\mu$  are the density and the viscosity of the liquid, respectively, and  $g$  the gravitational acceleration,  $\sigma$  the surface tension,  $v_b$  the bubble velocity and  $L$  the characteristic length. The characteristic length  $L$  was the channel height  $H$  in the 2D simulations and the pipe diameter  $D$  in the 3D simulations. The simulation results for low surface tension or low  $\Sigma$  are in good agreement with the experimental data. For example the simulation for the 2D Benjamin bubble with  $\Sigma = 3.0 \times 10^{-3}$  and  $Mo = 2.53 \times 10^{-11}$  gave a dimensionless bubble velocity of  $v_b / \sqrt{g H} = 0.459$ , which is in good agreement with the experimental value of 0.468. Simulations for the 3D Benjamin bubble with  $\Sigma = 0.01$  and  $Re = 9290$  gave a dimensionless bubble velocity of  $v_b / \sqrt{g D} = 0.494$  in fair agreement with the experimental value of 0.462. However in flows dominated by the surface tension the simulation results do not agree with the experimental data. For example the simulation for the 2D Benjamin bubble with  $\Sigma = 246 \times 10^{-3}$  and with  $Mo = 2.53 \times 10^{-11}$  gave a dimensionless bubble velocity of  $v_b / \sqrt{g H} = 0.349$ , while the experimental value was 0.2. The reason for the deviation of the simulation results from the experimental data when the flow is dominated by the surface tension is due to the presence of the so-called parasite currents in the CFD simulations. These parasite currents are vortices in the neighbourhood of interface region despite the absence of any external forcing. It is known from the literature that these parasite currents scale with the viscosity and the surface tension. Thus the parasite currents are a numerically artifact when the Continuum Surface Force (CSF) method is applied, appearing in flows dominated by the surface tension. Furthermore the simulations shows that the bubble velocity decreases as the surface tension (or  $Eo$ ) is increased, which is in agreement with experimental observation.

The simulation results for the 2D and 3D Benjamin bubble with a very high viscosity show that the bubble velocity decreases with increasing time when the bubble moves along the length of the pipe. The comparison of the simulation results for this case was not straightforward, since the bubble velocity was measured at a single position in the experiments. No experimental data in the literature could be found which report the bubble velocity along the length of the pipe. Furthermore, as expected, the bubble velocity decreases when the viscosity increases.

### Summary of the simulation results for the Dumitrescu or Taylor bubble

The Dumitrescu or Taylor bubble has an axisymmetric nature, but both 2D axisymmetric and 3D simulations were performed. By neglecting the effect of viscosity and the surface tension Dumitrescu (1943) was able to obtain an analytical expression for the dimensionless bubble velocity and the radius of curvature close to the bubble nose. The analytical value of the dimensionless bubble velocity is  $v_b / \sqrt{g D} = 0.352$  and the value for the radius of curvature is  $\varrho / D = 0.75$ . The simulation results for the 2D axisymmetric bubble with zero viscosity and zero surface tension do not agree with the analytical result of Dumitrescu (1943). For example the simulations for the 2D axisymmetric bubble with a second order scheme gave a dimensionless bubble velocity of  $v_b / \sqrt{g D} = 0.409$  on a coarse mesh, while this value was 0.427 for the finest mesh. The corresponding radius of curvature was  $\varrho / D = 0.56$  for the coarse mesh and  $\varrho / D = 0.25$  for the finest mesh. The disagreement between the simulations and the analytical solutions is most likely due to the existence of multiple solutions for the inviscid problem. The existence of multiple solutions is also reported in the literature by Mao and Dukler (1990), in which the authors claim that the surface tension is responsible for obtaining the physically relevant solution. Keeping this in mind a simulation with a small surface tension and viscosity ( $Eo = 200$  and  $Mo = 1.6 \times 10^{-11}$ ) corresponding with the experimental conditions of White and Beardmore (1962) was performed. This simulation gave a dimensionless bubble velocity of  $v_b / \sqrt{g D} = 0.344$ , which is in very good agreement with the experimental value of 0.345 given by White and Beardmore (1962) and the analytical value of 0.352. This result supports the claim of Mao and Dukler (1990) that the surface tension is most likely responsible for obtaining the physically relevant solution.

---

In addition to the 2D axisymmetric simulations also 3D simulations were performed. These 3D simulations show that the bubble becomes unstable at a certain bubble length. In the present simulations this critical length was about  $6D$ , where  $D$  is the diameter of the pipe. Furthermore the instability causes the bubble to become asymmetric and as a consequence the bubble velocity increases. Obviously, the instability and the asymmetry are not seen in the 2D axisymmetric simulations.

One simulation with an Eötvös number of 100 and a Morton number of 0.015, corresponding with the experimental conditions of Bugg and Saad (2002), was performed. The results of this simulation, e.g. the axial and radial velocities at several locations relative to the bubble nose, are in excellent agreement with the PIV measurements of Bugg and Saad (2002).



---

# Acknowledgements

I would like to thank Professor Ruud Henkes for giving me the opportunity to learn more about multi-phase flows and for his supervision of my master end project. Our weekly appointment and discussion really helped me finishing this project. Thanks for always being patient and for the positive way of thinking (also when multiplicity came into the game for the Taylor bubble). I want to thank Ruud more specifically for his support when I was sick for a long time period.

I would like to thank my roommates at the Kramers Lab. Sander thank you for helping me with FLUENT related problems. Bernhard thanks for helping me with the UDF's and for playing the "piano man" song. Dries thanks for solving my LATEX related problems. Alex thanks for organizing social activities, like mountain biking at a beautiful location and movie nights.

Finally, I would like to thank my parents and my girlfriend for their support. Pa, Ma and Warsha thanks a lot!



---

# Contents

Summary	ii
Acknowledgments	vi
List of symbols	x
<b>1 Introduction</b>	<b>1</b>
1.1 Multiphase flow in pipelines	1
1.1.1 Flow regimes in multiphase flow	1
1.1.2 Flow description in vertical pipes	2
1.1.3 Flow description in horizontal pipes	2
1.2 Problem description	3
1.3 Project motivation and goals	5
1.4 Literature review	5
1.5 Report structure	9
<b>2 Flow equations</b>	<b>11</b>
2.1 Governing fluid dynamics equations	11
2.1.1 Continuity equation	11
2.1.2 Equation of motion	12
2.1.3 Equations in terms of the substantial time derivative	12
2.1.4 Navier-Stokes equation	12
2.1.5 Stokes flow equation	12
2.1.6 Euler equation	13
2.1.7 Bernoulli equation	13
<b>3 Benjamin bubble</b>	<b>15</b>
3.1 Two-dimensional flow	15
3.1.1 Mass and momentum balance for 2D flow	15
3.1.2 Intersection angle near the stagnation point	17
3.2 Three-dimensional flow	18
3.2.1 Mass and momentum balance for 3D flow	18
3.3 Summary	21
<b>4 Dumitrescu or Taylor bubble</b>	<b>23</b>
4.1 Analytical solution	23
4.1.1 Series expansion for the potential	25
4.1.2 Determination of the coefficients	27
4.2 Summary	30
<b>5 Numerical methods</b>	<b>31</b>
5.1 Finite Volume Method	31
5.1.1 Discretization of the transport equations	31
5.1.2 Temporal discretization	32
5.1.3 Spatial discretization	33
5.2 Volume Of Fluid Method	34

5.2.1	Volume fraction equation . . . . .	34
5.2.2	Geometric reconstruction scheme . . . . .	34
5.2.3	Momentum equation . . . . .	35
5.2.4	Properties of the phases . . . . .	35
5.2.5	Surface tension . . . . .	35
5.3	Simulation setup . . . . .	36
5.3.1	Simulation setup for the Benjamin bubble . . . . .	36
5.3.2	Simulation setup for the Dumitrescu or Taylor bubble . . . . .	39
<b>6</b>	<b>Simulation results for the Benjamin bubble</b>	<b>41</b>
6.1	Results for the 2D Benjamin bubble . . . . .	41
6.1.1	Effect of viscosity and surface tension . . . . .	45
6.2	Results for the 3D Benjamin bubble in a pipe . . . . .	53
6.2.1	Effect of viscosity and surface tension for the 3D Benjamin bubble in a pipe . . .	56
6.3	Conclusions . . . . .	60
<b>7</b>	<b>Simulation results for the Dumitrescu or Taylor bubble</b>	<b>61</b>
7.1	2D Axisymmetric Dumitrescu bubble . . . . .	61
7.1.1	Bubble velocity . . . . .	61
7.1.2	Effect of surface tension . . . . .	64
7.2	3D Dumitrescu bubble . . . . .	66
7.2.1	Bubble velocity . . . . .	66
7.2.2	Effect of viscosity and surface tension . . . . .	68
7.3	Conclusions . . . . .	72
<b>8</b>	<b>Conclusions and Recommendations</b>	<b>73</b>
8.1	Conclusions . . . . .	73
8.2	Recommendations . . . . .	75
	<b>Bibliography</b>	<b>77</b>
<b>A</b>	<b>Dimensional analysis for rise of a Dumitrescu or Taylor bubble</b>	<b>81</b>
<b>B</b>	<b>User Defined Function</b>	<b>83</b>
<b>C</b>	<b>Analysis of the falling film around a Dumitrescu bubble</b>	<b>85</b>

---

# List of symbols

## Roman Symbols

Symbol	Description	S.I. Units
<i>A</i>	Area	( $m^2$ )
<i>B</i>	Integration coefficient	(-)
<i>C</i>	Constant	(-)
<i>D</i>	Pipe diameter	( $m$ )
<i>H</i>	Channel height	( $m$ )
<i>J</i>	Bessel function	(-)
<i>L</i>	Characteristic length	( $m$ )
<i>P</i>	Pressure	( $Pa$ )
$\mathcal{P}$	Modified pressure	( $Pa$ )
<i>R</i>	Pipe radius	( $m$ )
<i>R</i>	Residual	(-)
<i>S</i>	Source term	(-)
<i>T</i>	Transpose	(-)
<i>V</i>	Volume	( $m^3$ )
<i>a</i>	Integration coefficient	(-)
<i>c</i>	Speed of sound	( $ms^{-1}$ )
<i>g</i>	Gravitational acceleration	( $ms^{-2}$ )
<i>h</i>	Height	( $m$ )
<i>k</i>	Integration coefficient	(-)
<i>l</i>	Length	( $m$ )
<i>n</i>	Surface normal	(-)
$\hat{n}$	Unit normal	(-)
<i>p</i>	Pressure	( $kgm^{-1}s^{-2}$ )
<i>t</i>	Time	( $s$ )
<i>u</i>	Radial velocity	( $ms^{-1}$ )
<i>v</i>	Axial velocity	( $ms^{-1}$ )
<i>w</i>	Bubble velocity	( $ms^{-1}$ )
<i>x</i>	Cartesian x-coordinate	( $m$ )
<i>y</i>	Cartesian y-coordinate	( $m$ )
<i>z</i>	Cartesian z-coordinate	( $m$ )

## Greek Symbols

Symbol	Description	S.I. Units
$\alpha$	Volume fraction	(-)
$\beta$	Root of Bessel function	(-)
$\delta$	Film thickness	(m)
$\zeta$	Dimensionless radial coordinate	(-)
$\eta$	Dimensionless axial coordinate	(-)
$\theta$	Angle	(°)
$\kappa$	Curvature	(m <sup>-1</sup> )
$\lambda$	Dimensionless bubble velocity	(-)
$\mu$	Dynamic viscosity	(Pa · s)
$\rho$	Fluid density	(kgm <sup>-3</sup> )
$\varrho$	Radius of curvature	(m)
$\sigma$	Surface tension	(Nm <sup>-1</sup> )
$\tau$	Shear stress	(Pa)
$\phi$	Velocity potential or a field variable	(-)
$\varphi$	Velocity potential	(m <sup>2</sup> s <sup>-1</sup> )
$\psi$	Stream function	(m <sup>2</sup> s <sup>-1</sup> )
$\Delta$	Grid size	(m)

## Subscripts

Symbol	Description
$b$	Bubble
$f$	Face
$h$	Heavier fluid
$i$	Interface or index
$l$	Lighter fluid
$m$	Minimum
$max$	Maximum
$nb$	Neighbouring cells
$p$	Central point
$q$	Phase

## Superscripts

Symbol	Description
*	Dimensionless quantity
$\sim$	Dimensionless quantity
m	Index
n	Index
TM	Trademark

## Abbreviations

Abbreviation	Description
CFD	Computational Fluid Dynamics
CSF	Continuum Surface Force
FVM	Finite Volume Method
LDV	Laser Doppler Velocimetry
PIV	Particle Image Velocimetry
PISO	Pressure Implicit with Splitting of Operators
QUICK	Quadratic Upstream Interpolation for Convective Kinetics
UDF	User Defined Function
VOF	Volume Of Fluid
2D	Two-dimensional
3D	Three-dimensional

## Dimensionless groups

Symbol	Description	Definition
Co	Courant number	$\frac{\Delta t}{\Delta x_{grid\ cell}/u_{local}}$
Eo	Eötvös number	$\frac{\rho g L^2}{\sigma}$
Fr	Froude number	$\frac{v}{\sqrt{gL}}$
Ga	Galileo number	$\frac{\rho L \sqrt{gL}}{\mu}$
$\Sigma$	Inverse Eötvös number	$\frac{\sigma}{\rho g L^2}$
K	Characteristic number for parasite currents	$\frac{u_{max} \mu}{\sigma}$
Ma	Mach number	$\frac{v_f}{c}$
Mo	Morton number	$\frac{g \mu^4}{\rho \sigma^3}$
Re	Reynolds number	$\frac{\rho v L}{\mu}$
Re	Reynolds number	$\frac{\rho L \sqrt{gL}}{\mu}$



---

# Chapter 1

## Introduction

This introductory chapter will give a short overview of multiphase flow in pipelines, together with the related problems. Further, a summary of an extensive literature study is given and the project goals are outlined.

### 1.1 Multiphase flow in pipelines

Multiphase flows may be defined as flows that consist of two or more phases, which can be combinations of gases, liquids and solids. In this project we will confine ourselves to gas-liquid multiphase flow systems, specifically in pipelines. Gas-liquid flow in pipelines can adopt different flow structures, also known as flow patterns or flow regimes. The nature of these flow regimes is very complex and this explains why most of the research relies on experiments. However, these flow regimes are of importance in pipeline design and a short overview is given below.

#### 1.1.1 Flow regimes in multiphase flow

The main flow regimes in vertical and horizontal pipeflow are given in figure 1.1 and figure 1.2, respectively. These flow regimes are dictated by the pipeline configuration (e.g. diameter, inclination) and by the operating conditions (e.g. superficial gas and liquid velocities, pressure and temperature). A useful tool to find the relevant flow regime at certain conditions is the well-known flow pattern map. An example of this flow pattern map can be seen in figure 1.3. In figure 1.3(a) the superficial gas velocity  $u_{gs}$  and the superficial liquid velocity  $u_{ls}$  are used to define the transition boundaries between the flow regimes. In figure 1.3(b) dimensionless quantities ( $K$ ,  $X$ ,  $T$  or  $F$ ) based on  $u_{gs}$  and  $u_{ls}$ , are used. The idea of the flow pattern map is that for given flow conditions one easily can obtain the corresponding flow regime. Other types of flow pattern maps can be found in the literature, for instance the Baker chart after Baker (1954), but the key idea behind them is the same.

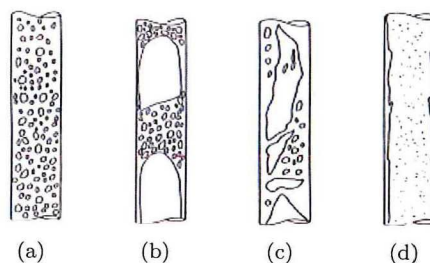


**Figure 1.1:** *Flow patterns in vertical upward two-phase flow; (a) Bubbly flow, (b) Slug flow, (c) Churn flow, (d) Annular flow (Taitel and Barnea, 1980).*

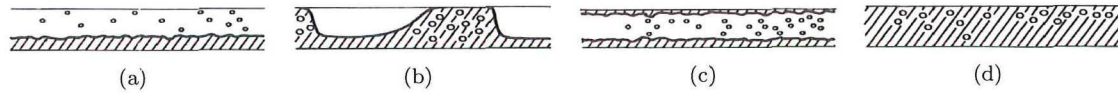
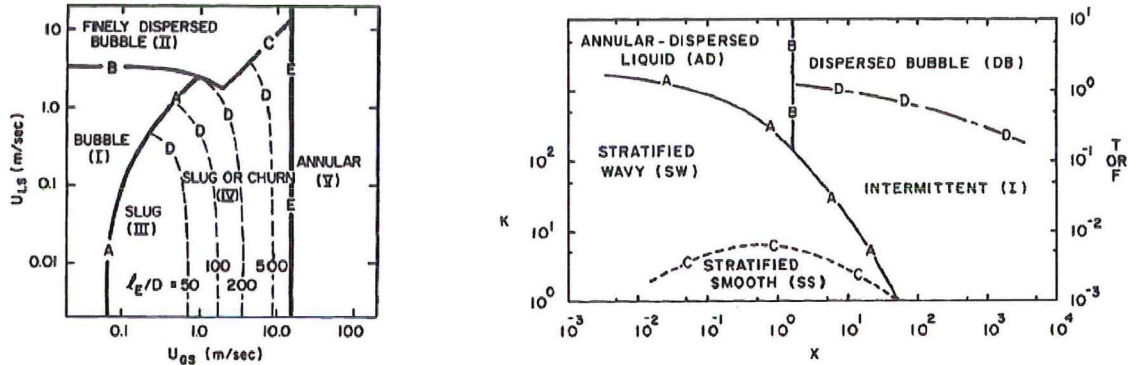


**Figure 1.2:** Flow patterns in horizontal two-phase flow; (a) Stratified (wavy) flow, (b) Slug or intermittent flow, (c) Annular flow, (d) Bubbly flow.



(a) Vertical upward flow (Taitel and Barnea, 1980).

(b) Horizontal flow (Taitel and Dukler, 1976).

**Figure 1.3:** Flow pattern map

### 1.1.2 Flow description in vertical pipes

As stated earlier, the different flow regimes are very complex in nature and the actual mechanisms that are responsible for the transition between flow regimes are not exactly known. However, several (simplified) models based on physical mechanisms are suggested to predict flow pattern transitions, see Taitel and Dukler (1976), Taitel and Barnea (1980) and Barnea (1987). A qualitative description of the flow regimes is given below:

- Bubbly flow: small bubbles are approximately uniformly distributed in the continuous liquid phase. This regime occurs at low gas velocities and an increase in gas flow will cause a transition to slug flow.
- Slug flow: contains large bullet-shaped bubbles with a diameter almost equal to the pipe diameter. These large bubbles are also called Taylor bubbles. These Taylor bubbles are separated by liquid slugs, which contain small bubbles. The suggested transition mechanism that governs the transition from bubbly flow to slug flow is coalescence of small bubbles to form large bubbles. Increasing the gas flow further will cause a transition to churn or froth flow.
- Churn flow: is a flow of chaotic nature. The Taylor bubbles are ruptured continuously and the flow becomes totally disordered. Due to this rupturing of the Taylor bubbles, liquid slugs will fall downward and will be lifted again by the gas. This oscillatory behaviour of the liquid is typical for churn flow. A higher gas flow rate, at this point, will result in a transition to the annular flow pattern.
- Annular flow: in this regime gas flows in the core of the pipe, while the liquid flows as a thin film around the perimeter of the pipe. The liquid film can be wavy and liquid droplets can be entrained in the gas core. The gas rate should be sufficient to lift the entrained droplets, otherwise these droplets will fall back and accumulate to cause a transition to churn or slug flow.

### 1.1.3 Flow description in horizontal pipes

The flow patterns observed in a horizontal pipe are different, due to gravitational effects, from the corresponding vertical flow patterns. The responsible mechanisms that cause the transition from one regime to the another are also different. A description of the horizontal flow regimes is given below:

- Stratified (smooth or wavy) flow: this flow regime is observed at low gas and liquid velocities. The liquid flows over the bottom of the tube and the gas flows over it maintaining the gas-liquid interface smooth. By increasing the gas velocity the smoothness of the interface is disturbed resulting in a wavy pattern. In the wavy regime liquid droplets may be entrained in the gas and increasing the gas velocity further will cause a transition to the slug flow regime.
- Slug flow: this flow regime contains large gas bubbles that cover almost completely the cross-section of the pipe. These large bubbles are separated by liquid slugs, which may be aerated at certain conditions. Higher gas velocities will result in a transition from slug flow to annular flow.
- Annular flow: in this flow pattern gas flows in the core of the pipe and the liquid forms a continuous film around the perimeter of the pipe. The liquid film at the top of the pipe may be thinner than the liquid film at the bottom of the pipe.
- Bubbly flow: this flow regime occurs at low gas velocities in which gas bubbles are dispersed in the continuous liquid phase. Due to buoyancy most of the gas bubbles will flow along the upper part of the pipe.

All these flow regimes may occur simultaneously in long pipelines or transition between flow regimes, due to changing operating conditions in time, may take place. The latter is very common in oil and gas production. Since, the pressure of an oil reservoir is high at the beginning of the field life, initially dispersed bubble flow may occur. When the well becomes older, however, the pressure drops and this will cause a transition to slug or churn flow. The predominant flow regime is slug flow in oil production and annular flow in gas production.

## 1.2 Problem description

Multiphase flow is not restricted to oil and gas transport in pipelines, but it is found in a wide variety of industrial applications. Examples are: bubble columns, vapour-liquid contactors or absorbers, reboilers, spraying systems, gas-liquid separators, chemical reactors and others. The design of all these industrial multiphase systems is based on simplified models, due to the complexity and lack of fundamental understanding. For instance, the current design of multiphase flow through pipelines is based on one-dimensional steady state or dynamic simulation methods. These methods are validated with experiments within a certain range of often idealized operating conditions and may be inaccurate for operating conditions outside this range. For example, Jepson and Taylor (1993) investigated the slug flow transitions in large diameter horizontal pipes and concluded that the transitions are not accurately predicted by the widely used Taitel and Dukler map (Taitel and Dukler, 1976). Probably, this was often overlooked, because smaller diameter pipes were used to validate the Taitel and Dukler map.

Clearly, a better understanding of multiphase flow is needed to improve the design of multiphase systems. Here, Computational Fluid Dynamics (CFD) may be a valuable tool. The advantage of CFD is that any operating conditions can be used and detailed information, which is often difficult to achieve in experiments, can be extracted. This is one of the reasons for the increasing interest, from a wide range of industries, to use CFD for design purposes. This is also noticed by the oil and gas industry, but application of CFD is still often restricted to the research environment. Reasons for the limited use of CFD for multiphase flow in pipelines are: (i) the large computer times, (ii) the complexity of the flow requiring proper turbulence models and interface models, (iii) the uncertainty of the reliability of the CFD predictions. In a recently published journal paper (De Schepper et al., 2008) the authors claimed that current CFD codes are able to predict the different multiphase flow patterns and transitions in a horizontal pipe. This claim seems to be somewhat premature, since not many validation studies, specifically to model multiphase flows in pipelines, can be found in the literature. Actually, much more validation is required to give a sensible judgement on the performance of current CFD codes for modeling multiphase flows in pipelines. This is the main motivation for the present project.

In the present study benchmark simulations are performed to assess the reliability of a selected CFD code for modeling multiphase flows in pipelines. The focus is on flow structures related to the slug flow regime. Hence, two benchmark cases, both closely related to the slug flow regime, are considered. The two cases are the so-called:

1. Benjamin bubble, which is a single large bubble in a stagnant or flowing liquid in a horizontal pipe and
2. Taylor bubble, which is a single large bubble in a stagnant or flowing liquid in a vertical pipe.

An example for both can be seen in figure 1.4 and may be compared with the slug flow pattern in figure 1.1 and figure 1.2, respectively. The structure of the bubble in slug flow is very similar to the structure of a single Benjamin or Taylor bubble. For instance, the velocity of Taylor bubbles in moving liquids can be expressed as:

$$u_t = C_0 u_m + u_b \quad (1.1)$$

where  $u_t$  is the translational velocity of the Taylor bubble in a flowing liquid,  $C_0$  is a dimensionless coefficient,  $u_m$  the mixture velocity and  $u_b$  the bubble velocity in stagnant liquid. Note that  $u_b$  equals the drift velocity of a Taylor bubble or Benjamin bubble. The same expression (1.1) is used to model slug flow. This explains our choice for the two benchmark cases. The dimensionless coefficient  $C_0$ , also known as the distribution parameter, depends on the velocity profile of the liquid ahead of the bubble. For turbulent flows  $C_0 \cong 1.2$  and  $C_0 \cong 2$  for laminar pipe flow (Polonsky et al., 1999). The relation 1.1 was first recognised by Nicklin et al. (1962) and since then it is used in slug flow models.

Validation of a CFD code can be done for problems that have an analytical solution or when highly detailed experimental data are available. Indeed, the two benchmark cases considered here have analytical solutions under some idealized conditions and experimental data can be found in the literature. Furthermore the quality of the numerical solutions can be assessed through successive grid refinement.

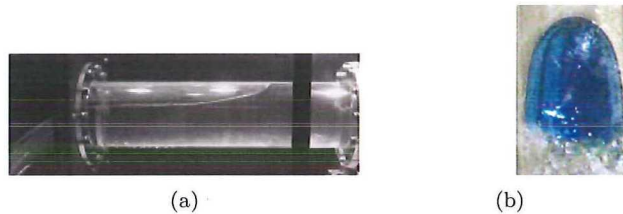


**Figure 1.4:** Example of; (a) Benjamin bubble (Hager, 1999), (b) Taylor bubble (Mandal et al., 2008)

### 1.3 Project motivation and goals

The motivation for the present project is the journal paper published by De Schepper et al. (2008), in which they claim that current CFD codes are able to predict the transition between the different flow regimes in a horizontal pipe. This can be very interesting for the oil and gas industry, since up to now the design of pipelines for multiphase flows are based on simplified 1D models, which could be improved if the claim is justified. This claim seems to be somewhat premature, because not many validation studies for modeling multiphase flow in pipelines can be found in the literature. Therefore, more research is required to be able to assess the reliability of CFD codes for modeling multiphase systems and to be able give a sensible judgement on the claim. Consequently the present project was started.

The goals of this project are as follows:

- Study the literature on multiphase flow to understand the physics;
- Model two benchmark cases, namely the Benjamin bubble and the Taylor bubble, with the commercial CFD code FLUENT. Compare the results of FLUENT with analytical solutions and with experimental data;
- Investigate the effect of viscosity and surface tension on the bubble motion;
- Give an overall assesement of current CFD codes for modeling multiphase flows in pipelines.

### 1.4 Literature review

An extensive literature study reveals that the problem associated with the motion of a single bubble in a stagnant liquid has been investigated in great detail in the past. A wide literature exists on the subject and a summary of selected papers can be found in table 1.1-1.3. A trend may be seen in these tables: until the eighties the problem was mostly investigated theoretically or experimentally, but since the eighties the computers became faster and researchers started to use numerical tools to study the problem.

The study on large bubbles was started almost one century ago by Gibson (1913). Gibson developed an empirical equation for the bubble rise velocity and reported the remarkable fact that the bubble velocity does not depend on the length of the bubble. Barr (1926) investigated the applicability of large bubbles as a tool for measuring viscosity of the liquid in which the bubble rises. Sir G.I. Taylor, after Davies and Taylor (1950), is often credited for the theoretical description of a single large bubble (Taylor bubble) that rises in a vertical tube in stagnant liquids, but in fact Dumitrescu (1943) was the first to solve the problem theoretically. Dumitrescu obtained an analytical expression for the bubble rise velocity and the bubble shape by neglecting viscous and surface tension effects. Experiments of various authors, listed in the tables below, support the theoretical result of Dumitrescu.

The first theoretical treatment for the motion of a large bubble in a horizontal pipe was given by Benjamin (1968). Assuming inviscid flow Benjamin obtained analytical solutions for the bubble velocity and the bubble shape. Benjamin's theory is also supported by experiments, see Zukoski (1966) and Gardner and Crow (1970). However, the experimental results in the somewhat older literature (before the eighties) are restricted to the terminal bubble velocity. The obvious reason for this is the available technique to do measurements in that specific time period. After the eighties several more sophisticated measurement techniques, such as laser Doppler velocimetry (LDV) (Kvernfold et al., 1984), photochromic dye activation (DeJesus, 1997) and particle image velocimetry (PIV) (Polonsky et al., 1999), (van Hout et al., 2002), (Bugg and Saad, 2002), (Nogueira et al., 2006a) and (Nogueira et al., 2006b), were used to study the motion of single large bubbles. Hence, detailed information on the velocity field around a large bubble and the bubble shape could be obtained.

**Table 1.1:** Literature summary and research history for a bubble moving into a liquid

Author (year)	Pipe/channel configuration	Nature of study	Results of investigation
Gibson (1913)	vertical	Theoretical & Experimental	Developed empirical equation for bubble rise velocity and described the shape in terms of tube size.
Barr (1926)	vertical	Experimental	Described the effect of bubble length, tube size and viscosity on the bubble rise velocity.
Hattori (1935)	vertical	Experimental	Found that the rise velocity of a cylindrical bubble is independent of its length and zero for $Eo < 3.36$ .
Dumitrescu (1943)	vertical	Theoretical & Experimental	Calculated the bubble rise velocity and shape assuming inviscid flow and a spherical nose of the bubble.
Davies and Taylor (1950)	vertical	Theoretical & Experimental	Calculated the bubble rise velocity assuming inviscid flow.
Laird and Chisholm (1956)	vertical	Experimental	Studied the forces and pressures acting on a large bubble.
Harmathy (1960)	vertical	Theoretical & Experimental	Gave an empirical correlation for the bubble rise velocity.
Bretherton (1961)	horizontal & vertical	Theoretical & Experimental	Studied large bubbles in capillary horizontal tubes and found that the bubble will not rise for $Eo < 3.37$ .
White and Beardmore (1962)	vertical & inclined	Experimental	Investigated the influence of fluid properties on the bubble velocity.
Goldsmith and Mason (1962)	vertical	Theoretical & Experimental	Described the motion of a single large bubble in viscous and inertial flow regime.
Nicklin et al. (1962)	vertical	Theoretical & Experimental	Described two-phase slug flow for bubbles rising in both stationary and flowing liquid.
Brown (1965)	vertical	Theoretical	Developed correlation for bubble rise velocity in viscous fluids by modifying Davies-Taylor results.
Brown and Govier (1965)	vertical	Theoretical	Developed a correlation for the voidage in two-phase slug flow.
Zukoski (1966)	horizontal, vertical & inclined	Experimental	Investigated the effect of surface tension, viscosity and tube inclination on the bubble velocity.
Benjamin (1968)	horizontal	Theoretical	Derived analytical expressions for the bubble drift velocity and shape assuming inviscid flow.

**Table 1.2:** Literature summary and research history for a bubble moving into a liquid (table 1.1 continued)

Author (year)	Pipe/channel configuration	Nature of study	Results of investigation
Gardner and Crow (1970)	horizontal	Experimental	Investigated the effect of surface tension on the bubble velocity and shape.
Collins et al. (1978)	vertical	Theoretical	Described the motion of large bubbles rising in both laminar and turbulent liquid flows.
Wilkinson (1982)	horizontal	Experimental	Investigated the effect of surface tension and throttling of the flow at the outlet.
Bendiksen (1984)	inclined	Experimental	Developed a correlation for bubble rise velocity in inclined pipes.
Baines (1985)	horizontal	Experimental	Described three regimes of motion of bubbles in horizontal tubes.
Bendiksen (1985)	vertical	Theoretical	Extended the work of Dumitrescu by taking surface tension into account.
Weber et al. (1986)	inclined	Experimental	Developed a correlation for bubble rise velocity in inclined tubes.
Nickens and Yannitell (1987)	vertical	Theoretical & Numerical	Studied the effect of surface tension and viscosity on the rise velocity by extending the work of Dumitrescu.
Markovich (1988)	horizontal	Theoretical	Investigated the effect of surface tension on the free outflow of a liquid.
Campos and Guedes de Carvalho (1988)	vertical	Experimental	Described the wakes of slugs in terms of the Reynolds number and the slug length.
Meiron (1989)	vertical	Numerical	Studied the stability of gas bubbles rising in inviscid fluids.
Mao and Dukler (1990)	vertical	Numerical	Calculated rise velocity and shape of Taylor bubble and showed that multiple solutions exist.
Mao and Dukler (1991)	vertical	Experimental & Numerical	Simulated Taylor bubbles in laminar and turbulent flow.
Tomiyama et al. (1993)	vertical	Numerical	Analyzed bubble motion using the VOF method.
Alves et al. (1993)	inclined	Theoretical & Experimental	Extended Benjamin's work to calculate bubble drift velocity in inclined and vertical pipes.

**Table 1.3:** Literature summary and research history for a bubble moving into a liquid (table 1.2 continued)

Author (year)	Pipe/channel configuration	Nature of study	Results of investigation
Tomiyaama et al. (1996)	vertical	Experimental & Numerical	Examined the feasibility of VOF method to model Taylor bubbles.
Montes (1996)	vertical	Theoretical & Experimental	Described the transition to a free-surface flow at the outlet of a horizontal pipe.
Ubbink (1997)	vertical	Numerical	Developed the CICSAM scheme and simulated the Taylor bubble as a validation case.
Bugg (1998)	vertical	Numerical	Investigated numerically the rise of a Taylor bubble through stagnant liquids.
Hager (1999)	horizontal	Theoretical & Experimental	Described cavity formation at the outlet of a horizontal pipe.
Shosho and Ryan (2001)	inclined	Experimental	Investigated the effect of pipe inclination on the bubble velocity for (non-)Newtonian fluids.
Bugg and Saad (2002)	vertical	Experimental & Numerical	Measured the velocity field around a Taylor bubble with PIV.
Viana et al. (2003)	vertical	Experimental	Provide a correlation for the bubble rise velocity.
Clanet et al. (2004)	vertical	Experimental	Studied the bubble rise velocity in pipes of arbitrary cross-section.
Taha (2006)	vertical	Numerical	Used a commercial CFD tool to model slug flow.
Nogueira et al. (2006a)	vertical	Experimental	Used PIV to determine velocity profiles in the nose region and annular film of a Taylor bubble.
Nogueira et al. (2006b)	vertical	Experimental	Studied the wake and near wake region of a Taylor bubble.
Gokcal (2008)	horizontal	Experimental	Investigated the effect of high oil viscosity on the bubble drift velocity.
Lu and Prosperetti (2009)	vertical	Numerical	Simulated Taylor bubbles with an in-house code.
Ben-Mansour et al. (2010)	horizontal	Numerical	Investigated the effect of pipe diameter and high oil viscosity on bubble drift velocity.

## 1.5 Report structure

The introduction was meant to give some general information on multiphase flow in pipelines and to formulate the problem. Next, in chapter 2 the basic equations of fluid dynamics are summarized, which can be helpful in later chapters. Chapter 3 and 4 describe the theory of the two benchmark cases, the Benjamin bubble and the Taylor bubble, respectively. Chapter 5 gives an overview of the numerical methods used to model the benchmark cases. In chapter 6 the results for the Benjamin bubble are presented, while chapter 7 contains the results of the Taylor bubble. In the final chapter conclusions are drawn and recommendations are given for future work.



---

## Chapter 2

# Flow equations

The intention of this chapter is to state some of the basic equations of fluid mechanics that will be useful in the upcoming chapters. The detailed derivations of these equations can be found in advanced fluid mechanics textbook, see for example Lamb (1932) or Batchelor (1967).

### 2.1 Governing fluid dynamics equations

The governing equations of fluid dynamics are based on the laws of conservation of mass, momentum and energy. These conservation laws are derived using the continuum hypothesis, which assumes that on macroscopic level fluids behaves the same as if they were perfectly continuous in structure. Furthermore the continuum hypothesis implies that the physical quantities such as mass and momentum associated with the fluid are uniformly distributed within a small volume. In reality this is not exactly true, for example mass is concentrated in the nuclei of a atom of a certain fluid and not uniformly distributed over the volume occupied by the fluid. In this report the focus will be on the macroscopic behaviour of the fluids, therefore the continuum hypothesis can be applied without any problem, see Batchelor (1967).

#### 2.1.1 Continuity equation

The continuity equation follows from the fact that it is impossible to create or destroy matter in any process (although it is possible, in nuclear reactions, to convert mass into energy). The continuity equation is given by, see e.g. Bird et al. (1960)

$$\frac{\partial}{\partial t}\rho = -(\nabla \cdot \rho\mathbf{v}), \quad (2.1)$$

where the term on the left hand side of equation 2.1 denotes the rate of change of mass per unit volume. The term on the right hand side of equation 2.1 describes the net rate of mass addition by convection per unit volume and  $(\nabla \cdot \rho\mathbf{v})$  is called the divergence of  $\rho\mathbf{v}$ . The bold symbols refer to vector quantities.

#### Incompressible fluid flow

When the density of a fluid does not change due to pressure changes during the motion, the fluid is said to be incompressible. The compressibility of a gaseous fluid is related to the Mach number (Lamb, 1932), which is a dimensionless number defined by:

$$\text{Ma} = \frac{v_f}{c}, \quad (2.2)$$

where  $v_f$  is the speed of the fluid and  $c$  the speed of sound in the fluid. Hence, the Mach number is the ratio of the speed of the fluid and the speed of sound in this fluid. Incompressibility can be assumed when  $\text{Ma} \ll 1$ . Practically all liquids can be regarded as incompressible, since large pressures

are required to compress liquids. In the case of an incompressible fluid the continuity equation 2.1 takes the simple form

$$\nabla \cdot \mathbf{v} = 0. \quad (2.3)$$

The Mach number in all the cases in this study is expected to be much smaller than unity and equation 2.3 can be applied.

### 2.1.2 Equation of motion

The equation of motion describes the motion of a fluid particle under influence of surface and body forces. The equation of motion in its general form is given by, see e.g. Bird et al. (1960)

$$\frac{\partial}{\partial t} \rho \mathbf{v} = -[\nabla \cdot \rho \mathbf{v} \mathbf{v}] - \nabla p - [\nabla \cdot \bar{\tau}] + \rho \mathbf{g}. \quad (2.4)$$

The term on the left hand side of equation 2.4 denotes the rate of change of momentum. The first term on the right hand side of equation 2.4 describes the rate of momentum addition by convection, the second and the third term on the right hand side describe the rate of momentum addition by molecular transport. The last term in equation 2.4 accounts for the action of an external force, such as gravity. All the terms in equation 2.4 are evaluated per unit volume. The symbols  $[\nabla \cdot \rho \mathbf{v} \mathbf{v}]$ ,  $\nabla p$  and  $[\nabla \cdot \bar{\tau}]$  are all vectors and are often called the divergence of  $\rho \mathbf{v} \mathbf{v}$ , the gradient of scalar  $p$  and the divergence of the viscous stress tensor  $\bar{\tau}$ , respectively. The viscous stress tensor  $\bar{\tau}$  for a Newtonian fluid is given by

$$\bar{\tau} = -\mu \left( \nabla \mathbf{v} + (\nabla \mathbf{v})^T \right) + \left( \frac{2}{3} \mu - \kappa \right) (\nabla \cdot \mathbf{v}) \delta \quad (2.5)$$

with  $\mu$  the dynamic viscosity,  $\nabla \mathbf{v}$  the velocity gradient tensor,  $(\nabla \mathbf{v})^T$  the transpose of the velocity gradient tensor,  $\kappa$  the dilatational viscosity,  $\nabla \cdot \mathbf{v}$  the divergence of the velocity vector and  $\delta$  the unit tensor.

### 2.1.3 Equations in terms of the substantial time derivative

The equation of continuity 2.1 and the equation of motion 2.4 can be expressed in terms of the substantial derivative,  $D/Dt = \partial/\partial t + \mathbf{v} \cdot \nabla$ , which denotes the time rate of change relative to an observer that is travelling with the fluid particle. The continuity equation and the equation of motion in terms of the substantial derivative are, see Bird et al. (1960)

$$\frac{D\rho}{Dt} = -\rho(\nabla \cdot \mathbf{v}), \quad (2.6)$$

$$\rho \frac{D\mathbf{v}}{Dt} = -\nabla p - [\nabla \cdot \bar{\tau}] + \rho \mathbf{g}. \quad (2.7)$$

### 2.1.4 Navier-Stokes equation

In the case of constant  $\rho$  and  $\mu$  and by inserting equation 2.5 in the equation of motion 2.7 leads to the Navier-Stokes equation:

$$\rho \frac{D\mathbf{v}}{Dt} = -\nabla p + \mu \nabla^2 \mathbf{v} + \rho \mathbf{g}. \quad (2.8)$$

This can also be written as

$$\rho \frac{D\mathbf{v}}{Dt} = -\nabla \mathcal{P} + \mu \nabla^2 \mathbf{v}, \quad (2.9)$$

where  $\mathcal{P} = p + \rho gh$  and is called the modified pressure.

### 2.1.5 Stokes flow equation

The Stokes flow equation is obtained by neglecting the acceleration terms in the Navier-Stokes equation 2.8, that is  $\rho(D\mathbf{v}/Dt) = 0$ , which gives

$$0 = -\nabla p + \mu \nabla^2 \mathbf{v} + \rho \mathbf{g}. \quad (2.10)$$

Stokes flow is obtained when the flow is extremely slow (or more precisely: when the Reynolds number is very low).

### 2.1.6 Euler equation

The Euler equation for inviscid fluids is obtained by neglecting the viscous forces in the Navier-Stokes equation:

$$\rho \frac{D\mathbf{v}}{Dt} = -\nabla p + \rho \mathbf{g}. \quad (2.11)$$

In real life there exist no inviscid fluids, but there are many flows in which viscous forces are negligible and equation 2.11 applies. In flows with high Reynolds number the viscous forces are often negligible in most parts of the domain, except close to walls. This fact is easily seen by making the Navier-Stokes equation dimensionless with a characteristic length  $l_0$ , a characteristic velocity  $v_0$  and a characteristic modified pressure  $\mathcal{P}_0 = p_0 + \rho g h_0$ . Then the following dimensionless quantities can be found:

$$\begin{aligned} \check{x} &= \frac{x}{l_0} & \check{y} &= \frac{y}{l_0} & \check{z} &= \frac{z}{l_0} \\ \check{\mathbf{v}} &= \frac{\mathbf{v}}{v_0} & \check{p} &= \frac{\mathcal{P} - \mathcal{P}_0}{\rho v_0^2} & \check{t} &= \frac{v_0 t}{l_0} \\ \check{\nabla} &= l_0 \nabla & \check{\nabla}^2 &= l_0^2 \nabla^2 & \frac{D}{D\check{t}} &= \frac{l_0}{v_0} \frac{D}{Dt} \end{aligned}$$

Inserting these dimensionless quantities in the Navier-Stokes equation 2.9 gives

$$\frac{D\check{\mathbf{v}}}{D\check{t}} = -\check{\nabla}\check{p} + \left[ \frac{\mu}{l_0 v_0 \rho} \right] \check{\nabla}^2 \check{\mathbf{v}} \quad (2.12)$$

in which one immediately can recognize the Reynolds number, which is defined as

$$\text{Re} = \left[ \frac{l_0 v_0 \rho}{\mu} \right]. \quad (2.13)$$

The Reynolds number is a dimensionless number that gives an indication of the relative importance of inertial forces versus viscous forces in a system. Indeed, at high Reynolds numbers the second term or viscous term on the right hand side of equation 2.12 will be negligible.

### 2.1.7 Bernoulli equation

The Bernoulli equation for steady flow is obtained by omitting the time derivative in the Euler equation 2.11 and using the vector identity  $[\mathbf{v} \cdot \nabla \mathbf{v}] = \frac{1}{2} \nabla(\mathbf{v} \cdot \mathbf{v}) - [\mathbf{v} \times [\nabla \times \mathbf{v}]]$  to rewrite the equation as

$$\rho \nabla \frac{1}{2} v^2 - \rho [\mathbf{v} \times [\nabla \times \mathbf{v}]] = -\nabla p - \rho g \nabla h. \quad (2.14)$$

The  $\mathbf{g}$  in equation 2.11 is expressed as  $-\nabla \Phi = -g \nabla h$  (Landau and Lifshitz, 1987), where  $h$  is the elevation in the gravitational field. The vector  $\mathbf{v} \times [\nabla \times \mathbf{v}]$  is perpendicular to the velocity  $\mathbf{v}$ , hence perpendicular to the streamline. A streamline is a line such that the tangent to that line at any point gives the direction of the velocity at that point. So from this  $\mathbf{v} \times [\nabla \times \mathbf{v}]$  will be zero along a streamline and equation 2.14 gives

$$\nabla \left( \frac{1}{2} \rho v^2 + p + \rho g h \right) = 0. \quad (2.15)$$

It follows from equation 2.15 that  $\frac{1}{2} \rho v^2 + p + \rho g h$  is constant along a streamline and Bernoulli's equation follows as

$$\frac{1}{2} \rho v^2 + p + \rho g h = C. \quad (2.16)$$

In general the constant  $C$  in equation 2.16 is different for different streamlines, but when the flow is irrotational, which means that  $\nabla \times \mathbf{v} = 0$  everywhere, the constant  $C$  has the same value everywhere in the flow.



---

## Chapter 3

# Benjamin bubble

The motion of a gas bubble or an empty cavity in a stagnant liquid in a horizontal flow is called the Benjamin bubble (Benjamin, 1968). The name is due to Benjamin, who was the first to describe the characteristics of such a flow and the related phenomena. In this report we will only consider gas flowing in a liquid, although the equations derived by Benjamin are applicable more generally to two immiscible fluids, where a lower density fluid replaces a heavier fluid. First the 2D channel problem will be illustrated followed by the 3D pipe flow. Analytical expressions of these two cases are given by Benjamin under the specification that the flow is steady and irrotational everywhere. Furthermore the effects of viscosity and surface tension are ignored. In addition it is assumed that the density of the lighter fluid  $\rho_2$  is much smaller than the density of the heavier fluid  $\rho_1$ .

### 3.1 Two-dimensional flow

The flow under consideration is illustrated in figure 3.1. In the actual configuration the bubble is moving to the left into a stagnant liquid. A Galilei translation is used to find a stagnant bubble in a moving liquid. The bubble is kept stationary by imposing a liquid velocity  $v_1$ , which equals the bubble drift velocity. The liquid flows between two infinite horizontal plates separated by a height  $H$ . Far upstream the liquid fills the space between the planes and has a constant velocity  $v_1$ . Far downstream at height  $h$  the flow with a free boundary is uniform and the velocity is  $v_2$ . The mass and momentum balances are used to derive analytical expressions for the liquid velocity  $v_2$  and the liquid height  $h$ .

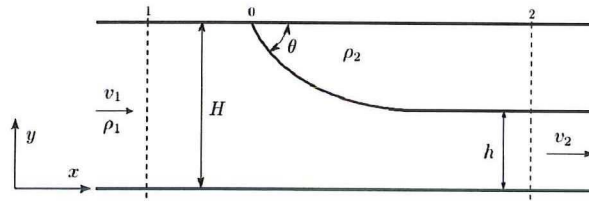


**Figure 3.1:** Analogous steady flow for a bubble moving into a stagnant liquid in a horizontal channel (Benjamin, 1968).

#### 3.1.1 Mass and momentum balance for 2D flow

As the flow is incompressible, equation 2.3 can be used. By neglecting the velocity gradient in the  $y$ -direction continuity requires

$$v_1 H = v_2 h. \quad (3.1)$$

The assumptions for the flow under consideration reduce the Navier-Stokes equation to the Bernoulli equation. The point 0 in figure 3.1 is a stagnation point, i.e. the velocity of the fluid is zero here. Applying the Bernoulli theorem, i.e. assuming no viscous dissipation, along the free surface (the free

surface is a streamline) gives for the heavier fluid

$$P_h = P_0 - \frac{1}{2}v^2\rho_1 + g(H - y)\rho_1. \quad (3.2)$$

Similarly applying Bernoulli's equation for the stationary bubble gives

$$P_l = P_0 + g(H - y)\rho_2. \quad (3.3)$$

There is no pressure drop across the interface, since surface tension is neglected, and therefore  $P_h$  should be equal to  $P_l$ . Therefore equating equation 3.2 and equation 3.3 gives the liquid velocity at the interface

$$v_i = \sqrt{2g(H - y)\frac{\rho_1 - \rho_2}{\rho_1}}. \quad (3.4)$$

Since we are considering a gas bubble here ( $\rho_2 \ll \rho_1$ ) equation 3.4 yields

$$v_i = \sqrt{2g(H - y)}. \quad (3.5)$$

The analysis of Benjamin starts from here. Benjamin assumed that the flow far downstream becomes uniform at a depth  $h$  and with velocity  $v_2$ . Subsequently, he applied Bernoulli's equation along the free surface between the stagnation point (point 0 in figure 3.1) and a point far downstream, point 2 in figure 3.1

$$\frac{P_0}{\rho} + gh_0 + \frac{1}{2}v_0^2 = \frac{P_2}{\rho} + gh_2 + \frac{1}{2}v_2^2. \quad (3.6)$$

The pressure  $P_2$  along the free surface is constant and equal to  $P_0$ , whereas the velocity at the stagnation point is equal to zero. The density was already assumed to be constant and with  $h_0$  is  $H$  and  $h_2$  is  $h$  equation 3.6 yields:

$$v_2^2 = 2g(H - h). \quad (3.7)$$

Applying Bernoulli's theorem between point 1 and stagnation point 0 along the upper boundary gives:

$$\frac{P_1}{\rho} + gh_1 + \frac{1}{2}v_1^2 = \frac{P_0}{\rho} + gh_0 + \frac{1}{2}v_0^2. \quad (3.8)$$

With  $h_1 = h_0 = H$  and  $P_0$  is zero equation 3.8 gives the pressure at the upper boundary far upstream

$$P_1 = -\frac{1}{2}\rho v_1^2 \quad (3.9)$$

and the pressure in the liquid below has a hydrostatic variation with depth. The flow far downstream is uniform and the pressure variation with depth is again hydrostatic. Therefore the momentum balance, per unit span, between point 1 and point 2 is given by

$$\int_0^H P_1 dy + \int_0^H \rho gy dy + \rho v_1^2 H = \int_0^h \rho gy dy + \rho v_2^2 h, \quad (3.10)$$

$$P_1 H + \frac{1}{2}\rho g H^2 + \rho v_1^2 H = \frac{1}{2}\rho g h^2 + \rho v_2^2 h. \quad (3.11)$$

Inserting equation 3.9 into equation 3.11 gives

$$2v_2^2 h + v_1^2 H = g(H^2 - h^2). \quad (3.12)$$

Making use of the continuity equation 3.1 we obtain

$$v_2^2 = \frac{g(H^2 - h^2)H}{(2H - h)h}. \quad (3.13)$$

By equating equations 3.7 and 3.13 a quadratic function for  $h$  is obtained,

$$\begin{aligned} 2g(H - h) &= \frac{g(H^2 - h^2)H}{(2H - h)h}, \\ 2(H - h) &= \frac{(H - h)(H + h)H}{(2H - h)h}, \\ 2h^2 - 3Hh + H^2 &= 0. \end{aligned} \quad (3.14)$$

The roots of equation 3.14 are  $h = H$ , which is a trivial solution, and the non-trivial one is

$$\frac{h}{H} = \frac{1}{2}. \quad (3.15)$$

This means that in the non-trivial case the flow downstream should occupy half of the space between the two parallel plates. Substitution of equation 3.15 into equation 3.7 and into the continuity equation 3.1 gives the following expression for the bubble velocity

$$v_1 = \frac{1}{2} \sqrt{gH}. \quad (3.16)$$

The dimensionless bubble velocity is given by

$$\frac{v_1}{\sqrt{gH}} = \frac{1}{2}. \quad (3.17)$$

The Froude number for the downstream liquid flow, which is the ratio of the inertia force and the gravity force, can be found by inserting equation 3.15 into equation 3.7:

$$\text{Fr} = \frac{v_2}{\sqrt{gH}} = \sqrt{2}. \quad (3.18)$$

Since the Froude number is larger than unity, the flow is supercritical. This flow may be realized by filling a channel of rectangular cross section with liquid and closing both ends. After the channel is fixed horizontally, one end is opened and under the action of gravity the liquid discharges freely from this end. Gas from the ambient enters the channel at the same time by replacing the volume of the discharged liquid. Similar experiments were done by Gardner and Crow (1970) and by Wilkinson (1982) and two photographs are given below. The experiments were done under well defined conditions to minimize the effect of viscosity and surface tension.

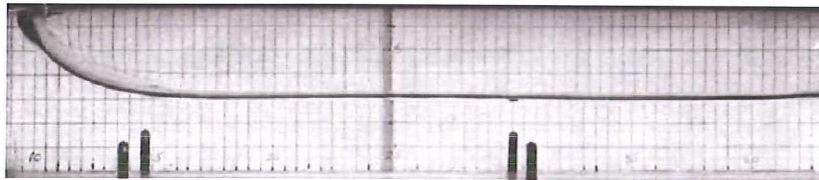


**Figure 3.2:** Motion of a large bubble in a horizontal channel (Gardner and Crow, 1970).

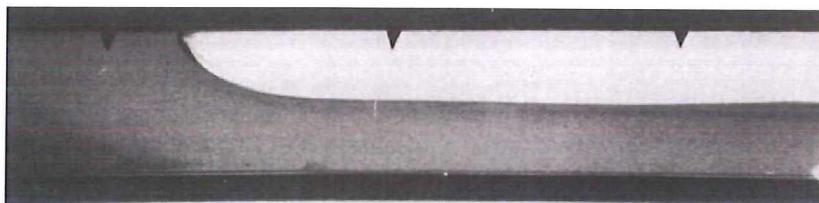


**Figure 3.3:** Motion of a large bubble in a horizontal duct (Wilkinson, 1982).

The flow shows the same characteristics as described by Benjamin, except for the nose of the bubble near the top wall. A surface elevation is seen and both authors attribute this to surface tension effects.

### 3.1.2 Intersection angle near the stagnation point

The angle of intersection,  $\theta$  in figure 3.1, should be  $60^\circ$  as determined by von Kármán (1940). Von Kármán used a similar reasoning as employed by Stokes (1847) for the determination of the highest possible slope occurring in waves of finite height. Consider the complex variable  $z = x + iy$  and an

analytical function of  $z$ , namely  $f = \phi + i\psi$ , where  $\phi$  denotes the velocity potential and  $\psi$  the stream function. Then the complex velocity potential for the flow in the neighbourhood of the stagnation point  $z = x + iy = 0$  has the form (Batchelor, 1967)

$$f = Az^\alpha \quad (3.19)$$

where  $A$  and  $\alpha$  are real constants. The magnitude of the velocity is given by  $|df/dz| = A\alpha|z|^{\alpha-1}$ , hence  $v$  is proportional to  $y^{\alpha-1}$ . According to equation 3.4,  $v$  is proportional to  $y^{\frac{1}{2}}$  and we must have  $\alpha - 1 = \frac{1}{2}$  or  $\alpha = \frac{3}{2}$ . Then from equation 3.19 we have

$$z = \left(\frac{f}{A}\right)^{\frac{2}{3}}. \quad (3.20)$$

The streamline  $\psi = 0$  consist of the top wall and the free surface, where  $f = 0$  corresponds to the point of intersection, i.e. point 0 in figure 3.1. The angle between the two branches (the top wall and the free surface) of the streamline  $\psi = 0$  is the change in the value of the imaginary part of  $\log z = \frac{2}{3}\log(f/A)$ , when passing from  $\phi < 0$  to  $\phi > 0$ , that is equal to  $2\pi/3 = 120^\circ$ . Thus the angle  $\theta$  should be  $60^\circ$ .

## 3.2 Three-dimensional flow

Consider the liquid draining from a horizontal pipe with circular cross section, as shown in figure 3.4. This 3D pipe flow problem will be treated in the same manner as done for the 2D channel problem. The flow is again assumed to be steady, inviscid, irrotational and free of energy dissipation. Furthermore surface tension effects are ignored and the density of the heavier fluid  $\rho_1$  is much greater than the density of the lighter fluid  $\rho_2$ . The pipe has a radius  $r$  and the flow is uniform far upstream and far downstream. Moreover, the liquid height far upstream and far downstream is  $2r$  and  $h$ , respectively.

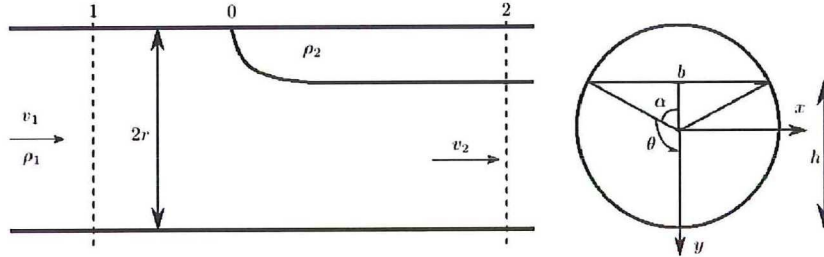


Figure 3.4: Steady flow in a horizontal pipe with circular cross section (Benjamin, 1968).

### 3.2.1 Mass and momentum balance for 3D flow

The free surface far downstream intersects the pipe wall at an angle of  $2\alpha$  from the centre of the pipe. Therefore the width  $b$  of the free surface is given by

$$b = 2r \sin \alpha \quad (3.21)$$

and the cross sectional area  $A_2$  beneath it is given by

$$A_2 = (\pi - \alpha + \frac{1}{2} \sin 2\alpha) r^2 = \pi r^2 (1 - \zeta), \quad (3.22)$$

where  $\zeta = (\alpha - \frac{1}{2} \sin 2\alpha) / \pi$ . The continuity equation leads to

$$A_1 v_1 = A_2 v_2 \quad (3.23)$$

which can also be expressed as:

$$\frac{v_1}{v_2} = \frac{A_2}{A_1} = 1 - \zeta. \quad (3.24)$$

Similar to the 2D problem, application of the Bernoulli theorem along the free surface, between the stagnation point 0 and point 2, gives:

$$\frac{P_0}{\rho} + gh_0 + \frac{1}{2}v_0^2 = \frac{P_2}{\rho} + gh_2 + \frac{1}{2}v_2^2. \quad (3.25)$$

The pressure along the free surface and the velocity at the stagnation point is zero. The heights  $h_0$  and  $h_2$  are  $2r$  and  $h$ , respectively. Therefore equation 3.25 yields:

$$v_2^2 = 2g(2r - h). \quad (3.26)$$

The liquid height  $h$  far downstream is given by

$$h = r(1 + \cos\alpha). \quad (3.27)$$

Inserting equation 3.27 into equation 3.26 gives

$$v_2^2 = 2gr(1 - \cos\alpha). \quad (3.28)$$

Applying the Bernoulli theorem between point 1 and point 0 gives the pressure at the uppermost point of the cross section far upstream. This is equivalent to equation 3.8 and results again into:

$$P_1 = -\frac{1}{2}\rho v_1^2. \quad (3.29)$$

The momentum balance between point 1 and point 2 is given by

$$(P_1 + \rho gr + \rho v_1^2)\pi r^2 - \int_{\alpha}^{\pi} \rho gr(\cos\alpha - \cos\theta)b d\theta - \rho v_2^2 A_2 = 0. \quad (3.30)$$

The integral term in equation 3.30 represents the hydrostatic force far downstream and since the width  $b$  is varying with  $\theta$  the  $\alpha$  in equation 3.21 is replaced by  $\theta$ . Therefore the integral term in equation 3.30 can be written as

$$2\rho gr^3 \int_{\alpha}^{\pi} (\cos\alpha - \cos\theta)\sin^2\theta d\theta \quad (3.31)$$

which can be integrated by splitting the integral into

$$2\rho gr^3 \left[ \cos\alpha \int_{\alpha}^{\pi} \sin^2\theta d\theta - \int_{\alpha}^{\pi} \cos\theta \sin^2\theta d\theta \right]. \quad (3.32)$$

The first integral in equation 3.32 can be solved by using the goniometric relation

$$\sin^2\theta = \frac{1 - \cos 2\theta}{2} \quad (3.33)$$

and the second integral by substitution. Therefore the solution of equation 3.31 is

$$2\rho gr^3 \int_{\alpha}^{\pi} (\cos\alpha - \cos\theta)\sin^2\theta d\theta = \rho gr \left( A_2 \cos\alpha + \frac{2}{3}r^2 \sin^3\alpha \right). \quad (3.34)$$

Inserting the result of equation 3.34 into equation 3.30 yields

$$(P_1 + \rho gr + \rho v_1^2)\pi r^2 - \rho gr \left( A_2 \cos\alpha + \frac{2}{3}r^2 \sin^3\alpha \right) - \rho v_2^2 A_2 = 0. \quad (3.35)$$

Equations 3.24 and 3.28 are used to eliminate  $v_1$  and  $v_2$  in equation 3.35 and finally this leads to

$$\zeta^2(1 - \cos\alpha) + \zeta \cos\alpha - \frac{2}{3\pi} \sin^3\alpha = 0. \quad (3.36)$$

The last equation 3.36 is only a function of  $\alpha$  and is solved numerically to yield  $\alpha = 82.78^\circ$ , for which the corresponding  $\zeta = 0.42$ . Now  $v_2$  can be calculated from equation 3.28, which is given in dimensionless form by

$$\frac{v_2}{\sqrt{gD}} = 0.935. \quad (3.37)$$

Accordingly the bubble velocity  $v_1$  can be calculated using equation 3.24. In dimensionless form the bubble velocity is given by

$$\frac{v_1}{\sqrt{gD}} = 0.542. \quad (3.38)$$

The dimensionless liquid height far downstream is obtained by using equation 3.27

$$\frac{h}{D} = 0.563. \quad (3.39)$$

The Froude number of the flow can be defined by

$$\text{Fr} = \frac{v_2}{C} \quad (3.40)$$

where  $C$  is the speed of long infinitesimal waves relative to the liquid. In the case of shallow water waves,  $C$  is given by (Lamb, 1932)

$$C = \sqrt{\frac{gA_2}{b}} = \sqrt{\frac{\pi gr(1-\zeta)}{2\sin\alpha}} = 0.996\sqrt{gr} = 0.704\sqrt{gD}. \quad (3.41)$$

Therefore equation 3.40 gives

$$F = \frac{0.935\sqrt{gD}}{0.704\sqrt{gD}} = 1.328. \quad (3.42)$$

The Froude number is again larger than unity, so the flow is again supercritical.

The Benjamin bubble in a pipe is obtained by filling a horizontal pipe with liquid. The pipe is initially closed at both ends. Then one end of the pipe is suddenly opened and liquid flows freely out at this end. Similar to the 2D case, gas from the ambient will replace the volume of the discharged liquid. When the starting effects have disappeared the motion of the bubble will appear to be steady. Figure 3.5 shows two experimental pictures (Hager, 1999). Here the conditions were such that surface tension and viscosity effects were negligible.

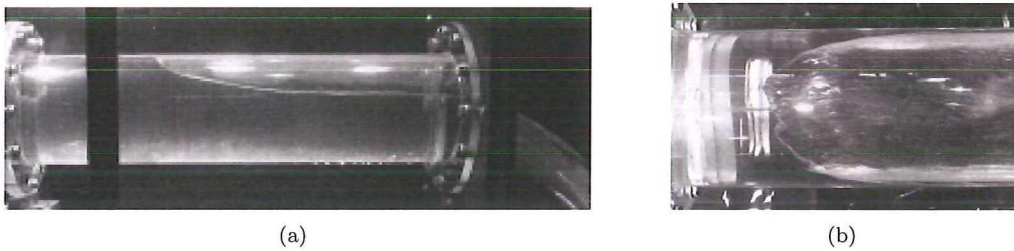


**Figure 3.5:** *Liquid outflow from a pipe;(a) side view, (b) top view.*

### 3.3 Summary

The problem of a single large bubble in stagnant liquid in a horizontal pipe (Benjamin bubble) has an analytical solution when the flow is irrotational and inviscid. In addition this analytical solution requires that the effect of surface tension is negligible and that the density of the gas is much smaller than the density of the liquid. Using these flow features Benjamin (1968) was able to solve the problem analytically. For a 2D channel flow Benjamin obtained a dimensionless bubble velocity of  $v/\sqrt{gH} = 0.5$  and a dimensionless liquid layer, which becomes constant away from the bubble nose, being equal to  $h/H = 0.5$ . For the 3D pipe flow a dimensionless bubble velocity of  $v/\sqrt{gD} = 0.542$  was obtained by Benjamin. The corresponding liquid height, which has a constant value far downstream from the bubble, is equal to  $h/D = 0.563$ . The theoretical results of Benjamin are supported by experimental data.



---

## Chapter 4

# Dumitrescu or Taylor bubble

The motion or rise of a single large bubble in a stagnant liquid in a vertical pipe is called a Taylor bubble, after Davies and Taylor (1950). Although Dumitrescu's investigation (Dumitrescu, 1943) on the motion of a large bubble in a vertical pipe was earlier and very similar to Taylor's analysis, it seems that his contribution is not sufficiently acknowledged.

### 4.1 Analytical solution

The flow is regarded to be inviscid, steady, irrotational and axisymmetric. Furthermore, the effect of surface tension is ignored and the density of the gas is much smaller than the density of the liquid. Although the problem and assumptions might seem to be similar to the Benjamin bubble problem, the solution for the Dumitrescu bubble is more complex. Consider a vertical pipe completely filled with liquid and closed at both ends. Now the lower end of the pipe is opened to the atmosphere and due to gravity the liquid freely flows out of the pipe. At the same time gas, in the form of a bubble, enters the pipe replacing the volume of the discharged liquid. The bubble obtained in this way may look like the one given in figure 4.1(a). It should be noted that in this case the bubble does not have a lower surface followed by a wake region as in figure 4.1(b). The problem solved by Dumitrescu and Taylor was for a type of bubble as shown in figure 4.1(a), which does not have a complex lower surface and wake. In fact the theoretical treatment of Dumitrescu and Taylor applies for an infinitely long bubble that rises in an infinitely long pipe of circular cross-section.

The problem is solved in a frame of reference attached to the bubble. This means that the bubble is kept stationary by applying a downward velocity, which is equal to the bubble rise velocity, to the whole system. The coordinate-system is given in figure 4.2.



**Figure 4.1:** Rise of a Dumitrescu bubble; (a) infinitely long bubble (Clanet et al., 2004), (b) finite bubble with a wake (Viana et al., 2003).

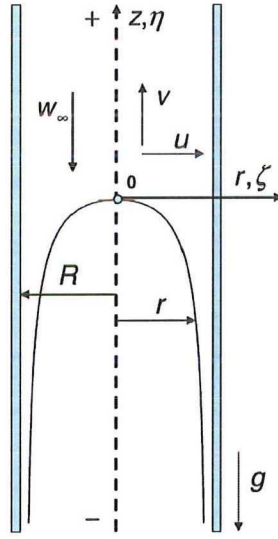


Figure 4.2: Coordinate-system of the Dumitrescu bubble (Dumitrescu, 1943).

Applying the Bernoulli equation along the liquid side of the interface gives

$$\frac{P_1}{\rho_1} - g|z| + \frac{1}{2}w^2 = \frac{P_0}{\rho_1} + gz_0 + \frac{1}{2}w^2 \quad (4.1)$$

where  $z_0 = 0$  is the stagnation point,  $P_0$  the pressure at  $z_0$ ,  $\rho_1$  is the density of the liquid,  $g$  the gravity constant and  $w$  the liquid velocity at the gas-liquid interface. From equation 4.1 follows that

$$P_1 = P_0 + \rho_1 g|z| - \frac{1}{2}\rho_1 w^2. \quad (4.2)$$

Similarly, applying Bernoulli equation to the stationary bubble and requiring that  $P_2 = P_0$  for  $z = 0$  gives

$$\frac{P_2}{\rho_2} - g|z| = \frac{P_0}{\rho_2}. \quad (4.3)$$

From equation 4.3 follows that

$$P_2 = P_0 + \rho_2 g|z| \quad (4.4)$$

and the assumption of zero surface tension requires that  $P_1 = P_2$ , which states that there is no pressure drop across the interface. Equating equation 4.2 and equation 4.4 gives the velocity at the bubble interface

$$w = \sqrt{2g|z| \left(1 - \frac{\rho_2}{\rho_1}\right)}. \quad (4.5)$$

With  $\rho_2 \ll \rho_1$  equation 4.5 reduces to

$$w = \sqrt{2g|z|}. \quad (4.6)$$

So far the easy part of the problem has been discussed, but the main difficulty is to obtain the shape of the bubble and to satisfy equation 4.6 simultaneously. This is not an easy task as it will become clear soon. However, to solve this issue Dumitrescu formulated the problem as finding a solution to the Laplace equation  $\nabla^2 \varphi = 0$  such that

1. equation 4.6 is satisfied on a yet to be determined streamline or bubble shape, and
2. where the walls of the pipe are streamlines themselves.

This problem turns out to be an eigenvalue problem and the solution procedure applied by Dumitrescu (also by Taylor) will be summarized below.

### 4.1.1 Series expansion for the potential

The flow is irrotational and axisymmetric, hence the Laplace equation  $\nabla^2\varphi=0$  in cylindrical coordinates takes the form

$$\frac{\partial^2\varphi}{\partial z^2} + \frac{\partial^2\varphi}{\partial r^2} + \frac{1}{r} \frac{\partial^2\varphi}{\partial r} = 0 \quad (4.7)$$

and the corresponding Stokes streamfunction is given by (Lamb, 1932)

$$\frac{\partial^2\psi}{\partial z^2} + \frac{\partial^2\psi}{\partial r^2} - \frac{1}{r} \frac{\partial^2\psi}{\partial r} = 0. \quad (4.8)$$

The general solution for equation 4.7 and equation 4.8 for  $r = R$  is given by (Lamb, 1932)

$$\varphi = \sum_{i=1}^n c_i J_0 \left( \beta_i \frac{r}{R} \right) e^{-\beta_i \frac{z}{R}}, \quad (4.9)$$

$$\psi = r \sum_{i=1}^n c_i J_1 \left( \beta_i \frac{r}{R} \right) e^{-\beta_i \frac{z}{R}}, \quad (4.10)$$

where  $J_0$  and  $J_1$  are Bessel functions,  $\beta_i$  is a root of the equation  $J_1(\beta) = 0$  and  $c_i$  is an arbitrary constant. The first two roots of  $J_1(\beta) = 0$  is for  $\beta = 3.832$  and  $\beta = 7.016$ . By applying a downward velocity  $w_\infty$ , to keep the bubble steady, the equations 4.9 and 4.10 become

$$\varphi = -w_\infty z + \sum_{i=1}^n c_i J_0 \left( \beta_i \frac{r}{R} \right) e^{-\beta_i \frac{z}{R}}, \quad (4.11)$$

$$\psi = \frac{1}{2} w_\infty r^2 + r \sum_{i=1}^n c_i J_1 \left( \beta_i \frac{r}{R} \right) e^{-\beta_i \frac{z}{R}}. \quad (4.12)$$

Equation 4.6 should hold at the interface and the following condition should be satisfied:

$$w^2 = u^2 + v^2 = 2g|z|. \quad (4.13)$$

Equation 4.13 is equivalent to

$$\left( \frac{\partial\varphi}{\partial z} \right)^2 + \left( \frac{\partial\varphi}{\partial r} \right)^2 = 2g|z|. \quad (4.14)$$

So far the solution approach of Dumitrescu and Taylor is the same. First the procedure of Taylor will be discussed and after that we will continue with the approach of Dumitrescu.

#### Solution procedure by Taylor

Taylor used only one term in the series of equation 4.11 and equation 4.12. Doing this equation 4.11 takes the form

$$\varphi = -w_\infty z + c_1 J_0 \left( 3.832 \frac{r}{R} \right) e^{-3.832 \frac{z}{R}} \quad (4.15)$$

and equation 4.12 is reduced to

$$\psi = \frac{1}{2} w_\infty r^2 + r c_1 J_1 \left( 3.832 \frac{r}{R} \right) e^{-3.832 \frac{z}{R}}. \quad (4.16)$$

The bubble surface is chosen to coincide with  $\psi = 0$  and Taylor required the vertex of the air bubble to be at  $z = 0$ . To fulfil this requirement the coefficient of  $r^2$  in the expansion of  $\psi$  should be zero. Hence,

$$c_1 = -\frac{w_\infty R}{3.832}. \quad (4.17)$$

The consequence of taking only one term in the series expansion of equation 4.15 is that the condition 4.13 can not be satisfied at more than one point. To proceed, Taylor assumed that the condition 4.14 is satisfied on the bubble surface ( $\psi = 0$ ) when  $r = \frac{R}{2}$ . This is a very crucial assumption, since the solution for the bubble velocity depends strongly on which radius  $r$  is selected (Zukoski, 1966).

However, with this assumption the bubble velocity can readily be obtained by setting the following in equation 4.14

$$c_1 = -\frac{w_\infty R}{3.832}, \quad \frac{r}{R} = \frac{1}{2}, \quad \psi = 0. \quad (4.18)$$

With  $J_1 \left[ \frac{1}{2}(3.832) \right] = 0.580$  equation 4.16 gives

$$e^{-3.832 \frac{z}{R}} = \frac{3.832}{4(0.580)} = 1.65. \quad (4.19)$$

Equation 4.19 gives the  $z$  value at the arbitrary chosen  $r$

$$\frac{z}{R} = -0.131. \quad (4.20)$$

Note that in the chosen coordinate system the value of  $z$  at the interface is always negative (except for  $z = 0$ ), hence equation 4.20 is positive. Since  $J_0 \left[ \frac{1}{2}(3.832) \right] = 0.273$  equation 4.14 gives

$$\frac{2gR}{w_\infty^2}(0.131) = [1 - (1.65)(0.273)]^2 + [(0.580)(1.65)]^2. \quad (4.21)$$

The dimensionless bubble velocity follows from equation 4.21

$$\frac{w_\infty}{\sqrt{gR}} = 0.464. \quad (4.22)$$

Although the method applied by Taylor for obtaining the bubble velocity is very rough, the result 4.22 is in good agreement with experimental data. However, as was pointed earlier the result 4.22 depends on the chosen radius  $r$  at which the boundary condition 4.14 is satisfied. Thus a different choice of  $r$  will give a different bubble velocity. The result of Taylor can be improved by increasing the number of terms in the series of 4.11. Dumitrescu solved the problem by retaining three terms in the series expansion. The related difficulty and solution approach of Dumitrescu will be discussed next.

### Solution procedure by Dumitrescu

In this part the solution approach of Dumitrescu will be discussed. We will continue with his procedure just after equation 4.13. It follows from dimensional analysis (see Appendix A) that the bubble rise velocity should be proportional to the square root of the radius of the pipe and the gravity as

$$w_\infty = \lambda \sqrt{gR}, \quad (4.23)$$

where  $\lambda$  denotes a dimensionless constant,  $g$  the gravitational acceleration and  $R$  the radius of the pipe. Hence, all equations are non-dimensionalized with equation 4.23 and  $R$ . The dimensionless numbers are

$$\begin{aligned} \varphi^* &= \frac{\varphi}{\lambda \sqrt{gR^3}} & \psi^* &= \frac{\psi}{\lambda \sqrt{gR^5}} & u^* &= \frac{u}{\lambda \sqrt{gR}} & v^* &= \frac{v}{\lambda \sqrt{gR}} \\ \frac{z}{R} &= \eta & k_i &= \frac{c_i}{\sqrt{gR^3}} & \frac{r}{R} &= \zeta \end{aligned}$$

Using these dimensionless numbers the velocity potential equation 4.11 and the streamfunction equation 4.12 can be written as

$$\varphi^* = -\eta + \frac{1}{\lambda} \sum_{i=1}^n k_i J_0(\beta_i \zeta) e^{-\beta_i \eta}, \quad (4.24)$$

$$\psi^* = \frac{\zeta^2}{2} + \frac{\zeta}{\lambda} \sum_{i=1}^n k_i J_1(\beta_i \zeta) e^{-\beta_i \eta}. \quad (4.25)$$

The dimensionless velocity components  $u^*$  and  $v^*$  are given by

$$u^* = \frac{\partial \varphi^*}{\partial \zeta} = \frac{1}{\zeta} \frac{\partial \psi^*}{\partial \eta} = -\frac{1}{\lambda} \sum_{i=1}^n k_i \beta_i J_1(\beta_i \zeta) e^{-\beta_i \eta}, \quad (4.26)$$

$$v^* = \frac{\partial \varphi^*}{\partial \eta} = -\frac{1}{\zeta} \frac{\partial \psi^*}{\partial \zeta} = -1 - \frac{1}{\lambda} \sum_{i=1}^n k_i \beta_i J_0(\beta_i \zeta) e^{-\beta_i \eta}. \quad (4.27)$$

Point 0 ( $\zeta = \eta = 0$ ) in figure 4.2 is a stagnation point. Hence, the velocity components are zero ( $u = v = 0$ ) and equation 4.27 with  $J_0(0) = 1$  requires that

$$\lambda = -\sum_{i=1}^n k_i \beta_i. \quad (4.28)$$

From equation 4.28 it is clear that the dimensionless bubble velocity  $\lambda$  or the Froude number will depend on the coefficients  $k_i$ . Inserting equation 4.28 in the stream function equation 4.12 and dividing the result by  $\zeta$  gives the shape of the bubble

$$\frac{\psi^*}{\zeta} = \sum_{i=1}^n k_i J_1(\beta_i \zeta) e^{-\beta_i \eta} - \frac{1}{2} \zeta \sum_{i=1}^n k_i \beta_i = 0. \quad (4.29)$$

Equation 4.16 follows from the fact that the bubble shape is (or should be) a streamline and this streamline is chosen to be coincide with the iso-line  $\psi^*=0$ . The condition that still has to be satisfied is equation 4.13, which in dimensionless form is written as

$$u^{*2} + v^{*2} = \frac{2}{\lambda^2} |\eta|. \quad (4.30)$$

Inserting equation 4.26, equation 4.27 and equation 4.28, respectively for  $u^*$ ,  $v^*$  and  $\lambda$  in equation 4.30 gives

$$\left( \sum_{i=1}^n k_i \beta_i J_1(\beta_i \zeta) e^{-\beta_i \eta} \right)^2 + \left( -\sum_{i=1}^n k_i \beta_i + \sum_{i=1}^n k_i \beta_i J_0(\beta_i \zeta) e^{-\beta_i \eta} \right)^2 = |2\eta|. \quad (4.31)$$

The problem is now to determine the coefficients  $k_i$  such that the corresponding values of  $\zeta$  and  $\eta$  satisfy equation 4.29 and equation 4.31, simultaneously. After determining the coefficients  $k_i$ , the bubble velocity and the bubble shape can be obtained by equation 4.28 and equation 4.29, respectively.

#### 4.1.2 Determination of the coefficients

To determine the coefficients  $k_i$  we need to express  $\eta$  as a function of  $\zeta$ . For this purpose, the Taylor series expansion method is used. The required terms and their corresponding series expansion are given below

$$J_0(\beta_i \zeta) = 1 - \frac{1}{1^2} \left( \frac{\beta_i}{2} \right)^2 \zeta^2 + \frac{1}{(2!)^2} \left( \frac{\beta_i}{2} \right)^4 \zeta^4 - \dots = \sum_{n=0}^{\infty} \frac{(-1)^n}{(n!)^2} \left( \frac{\beta_i \zeta}{2} \right)^{2n}, \quad (4.32)$$

$$J_1(\beta_i \zeta) = \left( \frac{\beta_i}{2} \right) \zeta - \frac{1}{1!2!} \left( \frac{\beta_i}{2} \right)^3 \zeta^3 + \frac{1}{2!3!} \left( \frac{\beta_i}{2} \right)^5 \zeta^5 - \dots = \sum_{n=0}^{\infty} \frac{(-1)^n}{n!(n+1)!} \left( \frac{\beta_i \zeta}{2} \right)^{2n+1}, \quad (4.33)$$

$$e^{-\beta_i \eta} = 1 - 2 \left( \frac{\beta_i}{2} \right) \eta + \frac{2^2}{2!} \left( \frac{\beta_i}{2} \right)^2 \eta^2 - \dots = \sum_{n=0}^{\infty} \frac{2^n}{n!} \left( -\frac{\beta_i \eta}{2} \right)^n. \quad (4.34)$$

Inserting these expressions in equation 4.29 gives

$$\begin{aligned} \sum_{i=1}^n k_i J_1(\beta_i \zeta) e^{-\beta_i \eta} - \frac{1}{2} \zeta \sum_{i=1}^n k_i \beta_i = & \left( -\frac{B_3}{1!2!} \zeta^2 + \frac{B_5}{2!3!} \zeta^4 - \frac{B_7}{3!4!} \zeta^6 + \dots \right) \\ & - \frac{2}{1} \left( B_2 - \frac{B_4}{1!2!} \zeta^2 + \frac{B_6}{2!3!} \zeta^4 - \frac{B_8}{3!4!} \zeta^6 + \dots \right) \eta \\ & + \frac{2^2}{2!} \left( B_3 - \frac{B_5}{1!2!} \zeta^2 + \frac{B_7}{2!3!} \zeta^4 - \frac{B_9}{3!4!} \zeta^6 + \dots \right) \eta^2 \\ & \dots \dots \dots \end{aligned} \quad (4.35)$$

The first term on the left side of equation 4.31, inside the parenthesis, can be written as

$$\begin{aligned}
\sum_{i=1}^n k_i \beta_i J_1(\beta_i \zeta) e^{-\beta_i \eta} &= 2 \sum_{i=1}^n k_i \left( \frac{\beta_i}{2} \right) J_1(\beta_i \zeta) e^{-\beta_i \eta} \\
&= \frac{2}{1} \left( B_2 \zeta - \frac{B_4}{1!2!} \zeta^3 + \frac{B_6}{2!3!} \zeta^5 - \dots \right) \\
&\quad - \frac{2^2}{1} \left( B_3 \zeta - \frac{B_5}{1!2!} \zeta^3 + \frac{B_7}{2!3!} \zeta^5 - \dots \right) \eta \\
&\quad + \frac{2^3}{2} \left( B_4 \zeta - \frac{B_6}{1!2!} \zeta^3 + \frac{B_8}{2!3!} \zeta^5 - \dots \right) \eta^2 \\
&\quad \dots \dots \dots
\end{aligned} \tag{4.36}$$

Similarly, the second term on the left side of equation 4.31 can be written as

$$\begin{aligned}
\sum_{i=1}^n k_i \beta_i J_0(\beta_i \zeta) e^{-\beta_i \eta} - \sum_{i=1}^n k_i \beta_i &= 2 \sum_{i=1}^n k_i \left( \frac{\beta_i}{2} \right) J_0(\beta_i \zeta) e^{-\beta_i \eta} - 2 \sum_{i=1}^n k_i \left( \frac{\beta_i}{2} \right) \\
&= 2 \left( -\frac{B_3}{1^2} \zeta^2 + \frac{B_5}{(2!)^2} \zeta^4 - \frac{B_7}{(3!)^2} \zeta^6 + \dots \right) \\
&\quad - \frac{2^2}{1} \left( \frac{B_2}{1} - \frac{B_4}{1^2} \zeta^2 + \frac{B_6}{(2!)^2} \zeta^4 - \frac{B_8}{(3!)^2} \zeta^6 + \dots \right) \eta \\
&\quad + \frac{2^3}{2!} \left( \frac{B_3}{1} - \frac{B_5}{1^2} \zeta^2 + \frac{B_7}{(2!)^2} \zeta^4 - \frac{B_9}{(3!)^2} \zeta^6 + \dots \right) \eta^2 \\
&\quad \dots \dots \dots
\end{aligned} \tag{4.37}$$

where  $B_m$  is given by

$$B_m = \sum_{i=1}^n k_i \left( \frac{\beta_i}{2} \right)^m. \tag{4.38}$$

The symmetry of the bubble requires that the interface be expressed in terms of even degrees of  $\zeta$  and Dumitrescu used

$$\eta = - \sum_{x=1}^{\infty} a_x \zeta^{2x} \tag{4.39}$$

where  $a_x$  are constants. This expression for  $\eta$  can now be inserted in equation 4.35, 4.36 and 4.37. After this, the equations 4.29 and 4.31 are, respectively given by

$$\frac{1}{2} (4B_2 a_1 - B_3) \zeta^2 + \frac{1}{12} (B_5 - 12B_4 a_1 + 24B_3 a_1^3 + 24B_2 a_2) \zeta^4 + \dots = 0, \tag{4.40}$$

$$B_2^2 \zeta^2 + (-B_2 B_4 + 4B_2^2 a_1^2 + B_3^2) \zeta^4 + \dots = \frac{1}{2} (a_1 \zeta^2 + a_2 \zeta^4 + \dots). \tag{4.41}$$

The values of  $B_i$  in equation 4.40 and 4.41 can be found by comparing the coefficients of the corresponding  $\zeta$  degrees. For a given  $a_1$  equation 4.41 gives  $B_2^2 = a_1/2$  and with this  $B_1$  equation 4.40 can be used to find  $B_3$ . In this way all the  $B_m$  can be determined, provided that the coefficients  $a_x$  are known. Subsequently, equation 4.38 will result in a system of  $n$  linear equations with  $n$  unknowns as

$$\begin{aligned}
k_1 \left( \frac{\beta_1}{2} \right)^2 + k_2 \left( \frac{\beta_2}{2} \right)^2 + \dots + k_n \left( \frac{\beta_n}{2} \right)^2 &= B_2 \\
k_1 \left( \frac{\beta_1}{2} \right)^3 + k_2 \left( \frac{\beta_2}{2} \right)^3 + \dots + k_n \left( \frac{\beta_n}{2} \right)^3 &= B_3 \\
\dots \dots \dots & \\
k_1 \left( \frac{\beta_1}{2} \right)^{n+1} + k_2 \left( \frac{\beta_2}{2} \right)^{n+1} + \dots + k_n \left( \frac{\beta_n}{2} \right)^{n+1} &= B_{n+1}
\end{aligned} \tag{4.42}$$

For  $n \rightarrow \infty$  the system 4.42 will result in infinitely many equations with infinitely many unknowns. The problem now is to determine the coefficients  $k_i$ , which are functions of the arbitrary coefficients  $a_x$ . The coefficients  $k_i$  can be determined from equation 4.42, but this requires the bubble shape to be known (i.e. the  $a_x$ ). However, the shape is unknown in advance and the problem seems to be unsolvable. However, Dumitrescu observed two facts in his experiments:

1. close to the nose the bubble has a spherical shape and
2. the flow has an asymptotic behaviour for  $\eta \rightarrow -\infty$ .

Using these two facts Dumitrescu was able to solve the problem completely. The first fact is used to approximate the shape of the bubble in the vicinity of the nose. Hence, the shape of the bubble close to the nose is given by

$$\eta = \varrho \left( \sqrt{1 - \left(\frac{\zeta}{\varrho}\right)^2} - 1 \right) \quad \text{with } \zeta < \varrho < 1 \quad (4.43)$$

where  $\varrho$  denotes the radius of curvature. Using the Taylor series expansion, equation 4.43 can be approximated as

$$\eta = -\varrho \left( \frac{1}{2} \left(\frac{\zeta}{\varrho}\right)^2 + \frac{1}{8} \left(\frac{\zeta}{\varrho}\right)^4 + \frac{1}{16} \left(\frac{\zeta}{\varrho}\right)^6 + \dots \right). \quad (4.44)$$

Equation 4.43 has a similar form as equation 4.39 and by comparing these two the unknown coefficients  $a_x$  can be determined as a function of the radius of curvature  $\varrho$  as

$$a_x = \frac{1}{(2\varrho)^{2x-1}}. \quad (4.45)$$

Subsequently, the values for  $B_m$  can be determined from equation 4.40 and 4.41 as explained earlier. Then, the coefficients  $k_i$  can be obtained from equation 4.42. Finally, the bubble velocity can be found by using equation 4.28. However, this procedure requires the radius of curvature close to the bubble nose to be known. Consequently, Dumitrescu had to impose an additional boundary condition for  $\eta \rightarrow -\infty$ . Thus Dumitrescu assumed that close to the bubble nose the shape can be approximated by a sphere and the shape far away from the nose by an asymptotic function. For the latter asymptotic reconstruction he assumed the volumetric flow rate ( $Q = \pi D^2 w_\infty / 4$ ) between the bubble and the wall to be the same for every cross-section. Furthermore, he assumed a fully developed steady flow in the film far away from the bubble nose. Hence, continuity requires that

$$\frac{\pi}{4} ((2R)^2 - (2r)^2) \sqrt{2g|z|} = \frac{\pi}{4} (2R)^2 \lambda \sqrt{gR}, \quad (4.46)$$

where  $\sqrt{2g|z|}$  is the relative velocity at the bubble surface as given by equation 4.6 and  $w_\infty = \lambda \sqrt{gR}$  is the bubble rise velocity with  $R$  being the radius of the pipe. The dimensionless form of equation 4.46 is given by

$$\eta = \frac{\lambda^2}{2(1 - \zeta^2)^2}. \quad (4.47)$$

Note that  $\lambda$  depends on the radius of curvature. Finally, Dumitrescu connected the two solutions, the spherical nose equation 4.44 and the asymptotic equation 4.47, together with the requirement that the derivative at the point of intersection of the two curves should be continuous. Note that only for one radius of curvature the requirement of the continuous derivative is met, which implies that the solution is unique. In this way Dumitrescu uniquely determined the radius of curvature to be equal to 0.75 and the corresponding dimensionless bubble velocity to be given by  $\lambda = 0.496$ . This result of Dumitrescu is in agreement with experimental data reported by himself and by several other authors.

It is clear that the problem is much more complex than one might think at a first glance. Although the solution approach of Dumitrescu is more solid than the result of Taylor, the latter should at least be credited for the simplicity in obtaining the solution. Later Bendiksen (1985) extended the work of Dumitrescu by retaining six terms in the series expansion and by taking surface tension into account. Further, Bendiksen showed that, when surface tension is taken into account, it is not necessary to make an a priori assumption on the bubble shape in order to solve the problem.

## 4.2 Summary

An analytical approximation of the solution for the rise of a single large bubble in stagnant liquid in a vertical pipe (i.e. for the Dumitrescu or Taylor bubble) is possible under the assumption that the flow is axisymmetric, irrotational and inviscid. Dumitrescu (1943) was the first to solve the problem by neglecting the effect of surface tension and by assuming that the shape of the bubble is spherical near the nose. In this way Dumitrescu obtained the bubble shape and the dimensionless bubble velocity of  $w_\infty/\sqrt{gR} = 0.496$ . Davies and Taylor (1950) used a similar approach as Dumitrescu, the only difference being that they used one instead of three terms in the series expansion. In this way they found a dimensionless bubble velocity of 0.464. Later Bendiksen (1985) extended the work of Dumitrescu by taking surface tension into account, but the complexity was increased and the result for the bubble velocity was similar to what was found by Dumitrescu. The analytical approximation of both Dumitrescu and Davies & Taylor is in close agreement with experimental data.

---

## Chapter 5

# Numerical methods

Analytical solutions for the governing equations of fluid dynamics are restricted to some simple cases only. For more complex problems the solutions, if there exist any, should be obtained numerically. There are several numerical (i.e. finite difference, finite element and spectral) methods to discretize the governing equations. The commercial CFD code FLUENT, used for the modeling throughout this work, utilises the Finite Volume Method (FVM) to discretize the governing equations. In this study the focus is on the modeling of multiphase flow systems. Hence, a numerical multiphase model was required and the Volume Of Fluid (VOF) model as implemented in FLUENT was used for this. This chapter will give an overview of the FVM and of the VOF method as implemented in FLUENT. Further, a detailed explanation of the simulation setup is given.

### 5.1 Finite Volume Method

In the Finite Volume Method (FVM) the domain is sub-divided into a number of smaller sub-domains or control volumes. Subsequently the governing equations of fluid flow are integrated over each of the control volumes of the domain. Then the resulting integral equations are discretized to obtain a system of algebraic equations. Finally the algebraic equations are solved by an iterative method. Most of the commercial CFD codes use the FVM, because it is also applicable to unstructured meshes, which are frequently used for complex geometries. Below a summary of the discretization schemes is given, see Versteeg and Malalasekera (2007) for a detailed overview of the Finite Volume Method (FVM).

#### 5.1.1 Discretization of the transport equations

In the FVM approach a transport quantity  $\phi$  entering or leaving the control volume is described as a flux of that quantity entering or leaving the domain. The FVM is conservative, which means that the flux of  $\phi$  entering the control volume has to be equal to the flux of  $\phi$  leaving control volume, if no source or sink is present in the control volume. The general transport equation for a quantity  $\phi$  can be described by, see FLUENT (2006)

$$\frac{\partial}{\partial t}(\rho\phi) + \nabla \cdot (\rho\phi\vec{v}) = \nabla \cdot (\Gamma_\phi \nabla \phi) + S_\phi, \quad (5.1)$$

where  $\Gamma_\phi$  denotes the diffusion coefficient and  $S_\phi$  the source term. Integration of equation 5.1 over a control volume  $V$  gives

$$\int_V \frac{\partial \rho\phi}{\partial t} dV + \oint \rho\phi\vec{v} \cdot d\vec{A} = \oint \Gamma_\phi \nabla \phi \cdot d\vec{A} + \int_V S_\phi dV, \quad (5.2)$$

where  $\vec{A}$  is the surface area vector. The first term on the left hand side of equation 5.2 represents the change of  $\phi$  in time in the control volume. The second term on the left hand side represents the convective flux of  $\phi$  across faces of the control volume  $V$ . The first term on the right hand side represents the diffusive flux of  $\phi$  across the faces of control volume  $V$  and the last term on the right

hand side accounts for the contribution of source terms. Discretization of equation 5.2 gives, see FLUENT (2006)

$$V \frac{\partial \rho \phi}{\partial t} + \sum_f^{N_{faces}} \rho_f \vec{v}_f \phi_f \cdot \vec{A}_f = \sum_f^{N_{faces}} \Gamma_\phi \nabla \phi_f \cdot \vec{A}_f + S_\phi V, \quad (5.3)$$

where  $N_{faces}$  is the number of faces enclosing the control volume,  $\phi_f$  the value of  $\phi$  convected through face  $f$ ,  $\rho_f \vec{v}_f \cdot \vec{A}_f$  the mass flux through face  $f$ ,  $A_f$  the area of face  $f$ ,  $\nabla \phi_f$  the gradient of  $\phi$  at face  $f$  and  $V$  the volume of the control volume.

For transient simulations the term  $\frac{\partial \rho \phi}{\partial t}$  in equation 5.3 has to be discretized in time, which is referred to as the temporal discretization. Thus in transient simulations the governing equations have to be discretized in both space and time. Temporal and spatial discretization of the governing equations are discussed in section 5.1.2 and section 5.1.3, respectively. After the discretization of the governing equations in time and space, the linearized form of equation 5.3 will be

$$a_p \phi_p = \sum_{nb} a_{nb} \phi_{nb} + b, \quad (5.4)$$

where  $a_p$  and  $a_{nb}$  are the linearized coefficients for  $\phi_p$  and  $\phi_{nb}$  respectively and  $b$  the constant part of the source term. The subscripts  $p$  and  $nb$  refer to the central point and the neighbouring cells, respectively. In general the number of neighbouring cells will be equal to the number of faces of the control volume, with the exception of the control volumes that coincide with the boundaries. One can easily write a linear set of equations for each grid cell. These equations are solved simultaneously for all the grid cells within the domain, using an algebraic multi-grid (AMG) solver, see FLUENT (2006).

### 5.1.2 Temporal discretization

As mentioned earlier, the transport equations have to be discretized also in time for a transient simulation. This discretization is referred to as temporal discretization. In the temporal discretization the transient term in the transport equations is integrated over a time step. A general expression for the time evolution of a variable  $\phi$  is given by

$$\frac{\partial \phi}{\partial t} = F(\phi), \quad (5.5)$$

where  $F(\phi)$  is the function that incorporates the spatial discretization of equation 5.3. Using backward differences, the first-order temporal discretization is given by, see FLUENT (2006)

$$\frac{\phi^{n+1} - \phi^n}{\Delta t} = F(\phi). \quad (5.6)$$

The second-order accurate discretization is given by FLUENT (2006)

$$\frac{3\phi^{n+1} - 4\phi^n + \phi^{n-1}}{2\Delta t} = F(\phi). \quad (5.7)$$

Here  $\phi$  is a scalar quantity,  $n + 1$  is the value at the next time level,  $n$  the value at the current time level and  $n - 1$  the value at the previous time level.  $F(\phi)$  can be evaluated at the new time level (implicit time integration) or at the current time level (explicit time integration). The explicit time integration method is not available in FLUENT when the pressure-based solver is used. Hence in all the simulations the first order implicit time integration was used. The main advantage of the implicit discretization is that it is unconditionally stable with respect to the time step size, unlike the explicit discretization, where  $F(\phi)$  is evaluated at the current time level (FLUENT, 2006).

The first order implicit time discretization of  $F(\phi)$  is thus given by

$$\frac{\phi^{n+1} - \phi^n}{\Delta t} = F(\phi^{n+1}). \quad (5.8)$$

This can be solved iteratively at each time level by

$$\phi^{n+1} = \phi^n + \Delta t F(\phi^{n+1}). \quad (5.9)$$

### 5.1.3 Spatial discretization

FLUENT stores by default discrete values of the scalar quantity  $\phi$  at the cell centres (FLUENT, 2006). In order to obtain face values, as required for the convection terms in equation 5.3, the quantity  $\phi$  has to be interpolated from the centre values. This interpolation is accomplished by using an upwind scheme. Upwinding means that the face value  $\phi_f$  is derived from quantities in the cell upstream (upwind), relative to the direction of the fluid flow. FLUENT has the following upwind schemes: first-order upwind, second-order upwind, power law and QUICK. In this study the first-order upwind, the second-order upwind and the QUICK scheme was used. These schemes will be discussed below.

#### First-order upwind scheme

In this scheme quantities at cell faces are obtained by assuming that the cell-centre values of any field variable hold throughout the entire cell. In other words the face quantities are identical to the cell quantities. Thus the face value  $\phi_f$  is set equal to the cell-centre value of  $\phi$  in the upstream cell. This scheme has first-order accuracy only.

#### Second-order upwind scheme

For second-order accuracy, quantities at the cell face are computed using a multidimensional linear reconstruction approach. This approach achieves higher-order accuracy at cell faces through a Taylor series expansion of the cell-centered solution. The face value is computed by, see FLUENT (2006)

$$\phi_{f,sou} = \phi + \nabla\phi \cdot \vec{r}, \quad (5.10)$$

where  $\phi$  and  $\nabla\phi$  are the cell-centered value and its gradient in the upstream cell, respectively, and  $\vec{r}$  is the displacement vector from the upstream cell centroid to the face centroid.

#### QUICK upwind scheme

For a higher accuracy in the spatial discretization the third order scheme QUICK can be used. The QUICK scheme uses a three-point upstream weighted quadratic interpolation for the cell face values. The face value is obtained from passing a quadratic function through two downstream nodes and one upstream node, see Versteeg and Malalasekera (2007). The interface value of  $\phi$  at face  $e$  can be evaluated as, see (Versteeg and Malalasekera, 2007)

$$\Phi_e = -\frac{1}{8}\Phi_W + \frac{6}{8}\Phi_P + \frac{3}{8}\Phi_E \quad \text{for} \quad u_e > 0 \quad (5.11)$$

$$\Phi_e = -\frac{1}{8}\Phi_{EE} + \frac{6}{8}\Phi_E + \frac{3}{8}\Phi_P \quad \text{for} \quad u_e < 0 \quad (5.12)$$

The QUICK scheme in FLUENT is available only for quadrilateral and hexahedral meshes, due to the requirement of specific upstream and downstream interface cells. Therefore the QUICK scheme cannot be used in unstructured and hybrid grids (FLUENT, 2006).

## 5.2 Volume Of Fluid Method

The Volume Of Fluid (VOF) model is an Euler-Euler type of multiphase model (also known as a two-fluid model) and is based on the work of Hirt and Nichols (1981). Actually, the VOF model is a surface tracking technique applied at a fixed Eulerian mesh and it is used to model two or more immiscible fluids where the interface between the fluids is of interest. In the VOF model a single momentum equation is solved and the volume fraction for each of the phases is tracked throughout the domain. Moreover, the fields for all variables and properties are shared by the phases and are connected through the local volume fraction of the phases. Let now  $\alpha_q$  be the volume fraction of the  $q$ th phase in a computational cell then

- $\alpha = 0$  represents a cell that is empty of the  $q$ th fluid and
- $\alpha = 1$  represents a cell that is full of the  $q$ th fluid and
- $0 < \alpha < 1$  represents the interface between the  $q$ th phase and one of the other phases.

Based on these three possibilities of  $\alpha_q$ , appropriate properties and variables will be assigned to each computational cell.

### 5.2.1 Volume fraction equation

The interface between two or more phases is tracked by solving a continuity equation for the volume fraction of one or more of the phases. The equation for the volume fraction for the  $q$ th phase is given by (FLUENT, 2006)

$$\frac{\partial}{\partial t}(\alpha_q \rho_q) + \nabla \cdot (\alpha_q \rho_q \mathbf{v}_q) = S_{\alpha_q}, \quad (5.13)$$

where  $\alpha$  is the volume fraction of the  $q$ th phase,  $\rho_q$  the density of the  $q$ th phase and  $S_{\alpha_q}$  a source term, which is usually zero. If there are two phases equation 5.13 for the volume fraction is solved only for the secondary phase and the volume fraction for the primary phase is obtained by the following constraint:

$$\sum_{q=1}^n \alpha_q = 1. \quad (5.14)$$

Equation 5.14 simply states that sum of the volume fractions of all the phases in a control volume must be equal to unity. The volume fraction equation 5.13 may be solved through implicit or explicit time discretization:

$$\frac{\alpha_q^{n+1} \rho_q^{n+1} - \alpha_q^n \rho_q^n}{\Delta t} V + \sum_f (\rho_q^m U_f^m \alpha_{q,f}^m) = S_{\alpha_q} V, \quad (5.15)$$

where  $m = n + 1$  when the implicit scheme is used and  $m = n$  when the explicit scheme is used,  $n + 1$  is the index for the current time step,  $n$  is the index for the previous time step,  $\alpha_{q,f}$  is the face value of the  $q$ th volume fraction,  $V$  is the volume of the cell and  $U_f$  is the volume flux through the face based on the normal velocity. In the implicit approach FLUENT's standard finite difference interpolation schemes are used to obtain the face fluxes  $\alpha_{q,f}$  for all cells, including those near the interface. In the explicit approach the face fluxes can be interpolated either using the interface reconstruction scheme or using a finite volume discretization scheme. The geometric reconstruction scheme, which is an interface reconstruction scheme, was used in all the simulations. This scheme will be discussed in more detail below.

### 5.2.2 Geometric reconstruction scheme

The geometric reconstruction scheme is used when the cell is near the interface between two phases. In the geometric reconstruction scheme the interface is represented by a piecewise-linear approach. In this approach the interface between the two fluids has a linear slope within each cell, see figure 5.1. This linear shape is then used for the calculation of the advection of the fluid through the cell faces. This scheme is the most accurate one available in FLUENT and it is generalized for unstructured meshes from the work of Youngs (1982).

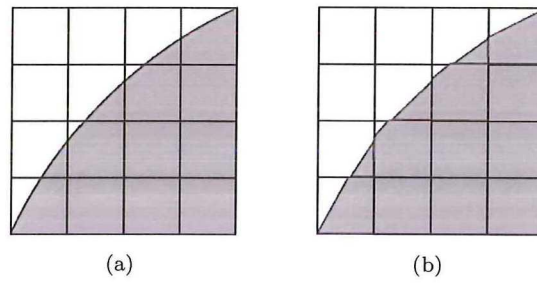


**Figure 5.1:** (a) Actual interface shape, (b) Interface shape represented by the geometric reconstruction scheme (FLUENT, 2006).

The reconstruction scheme is a three step process, see FLUENT (2006):

1. Calculation of the position of the linear interface, based on information for the volume fraction and its derivatives.
2. Calculation of the amount of advected fluid through each face computed from the linear interface representation and from information on the normal and tangential velocity distribution at the face.
3. Calculation of the volume fraction in each cell by balancing the fluxes calculated during the previous time step.

### 5.2.3 Momentum equation

As mentioned earlier a single momentum equation is solved in the VOF model and the obtained velocity field is shared by the phases. A consequence of this is that the standard output of FLUENT contains only results for the mixture phase (i.e. pressure, velocity and density). The momentum equation, which is equivalent to equation 2.4, is given by

$$\frac{\partial}{\partial t} \rho \mathbf{v} + [\nabla \cdot \rho \mathbf{v} \mathbf{v}] = -\nabla p + \nabla \cdot [\mu (\nabla \mathbf{v} + \nabla \mathbf{v}^T)] + \rho \mathbf{g} + \mathbf{F}, \quad (5.16)$$

where  $\rho$  and  $\mu$  are defined through equation 5.17 and equation 5.18, respectively.

### 5.2.4 Properties of the phases

The properties that appear in the transport equations are volume-fraction-averaged properties. For instance the density for an  $n$ -phase system is given by

$$\rho = \sum_{q=1}^n \alpha_q \rho_q. \quad (5.17)$$

Similarly, the viscosity is calculated as

$$\mu = \sum_{q=1}^n \alpha_q \mu_q. \quad (5.18)$$

### 5.2.5 Surface tension

The fact that small air bubbles in water or small liquid droplets in air take up a spherical form is due to the surface tension. Surface tension is a result of the movement of molecules that are located at an interface. Consider an air bubble in water. Inside the bubble, the net force on a molecule due to its neighbours is zero. However, the molecules at the interface experience, due to lack of neighbours, an unbalanced cohesive force and tend to move inwards. This tendency is equivalent to the contraction

of the interface, thereby increasing the pressure on the concave side of the interface. Surface tension is a force that only acts on a surface to balance the radially inward intermolecular cohesive force with the radially outward pressure gradient force across the interface. The reason that small air bubbles in water have a spherical shape is that surface tension acts to minimize the free energy by decreasing the area of the interface.

### Continuum Surface Force model

The surface tension model used in FLUENT is the Continuum Surface Force (CSF) model proposed by Brackbill et al. (1992). With this model the surface tension is modeled as a source term in the momentum equation. The origin of the source term can be understood by considering the special case where the surface tension is constant along the surface. Then it can be shown that the pressure drop across the interface depends upon the surface tension coefficient  $\sigma$  and the surface curvature as

$$p_2 - p_1 = \sigma \left( \frac{1}{R_1} + \frac{1}{R_2} \right), \quad (5.19)$$

where  $p_1 - p_2$  is the pressure difference across the interface,  $R_1$  and  $R_2$  are the surface radii in two perpendicular directions. In the CSF model the surface curvature is obtained from local gradients in the surface normal at the interface. The surface normal  $n$  is defined as the gradient of the volume fraction of the  $q$ th phase:

$$n = \nabla \alpha_q. \quad (5.20)$$

The curvature  $\kappa$  is defined as the divergence of the unit normal  $\hat{n}$ , see Brackbill et al. (1992):

$$\kappa = \nabla \cdot \hat{n}, \quad (5.21)$$

where

$$\hat{n} = \frac{n}{|n|}. \quad (5.22)$$

The surface tension can be expressed in terms of the pressure jump across the interface. The force at the interface can be expressed as a volume force using the divergence theorem, see Brackbill et al. (1992). This volume force is added to the momentum equation as a source term. For two phases the volume force has the following form

$$F_{vol} = \sigma_{ij} \frac{\rho \kappa_i \nabla \alpha_i}{\frac{1}{2}(\rho_i + \rho_j)}, \quad (5.23)$$

where  $\rho$  is the volume-averaged density.

## 5.3 Simulation setup

The simulation setup was based on the 'Best practices for the VOF model' document, see ANSYS FLUENT (2006) and ANSYS FLUENT (2007). Furthermore, chapter 23 of FLUENT (2006) for modeling multiphase flows was studied carefully before the simulations were started. The simulation setup for the Benjamin bubble and the Taylor bubble will be discussed separately.

### 5.3.1 Simulation setup for the Benjamin bubble

Prior to the simulation the numerical mesh was generated by the CAD tool GAMBIT. All the 2D simulations were done with a uniform grid, which means that the grid spacing was  $\Delta x = \Delta y$ . Subsequently the mesh was loaded in FLUENT and the problem was defined. The double-precision version of FLUENT was used in all the simulations. Since the VOF model is not available for the density-based solver the pressure-based solver was used for the simulations. Furthermore the simulations were transient and with the inclusion of the gravity. Moreover the VOF model was selected for the modeling of the two phases. In all the simulations the primary phase was air and the secondary phase was water or oil. Obviously, the inviscid model was selected in FLUENT for the modeling of the inviscid (and zero surface tension) flow.

### Boundary/initial conditions

The boundary and initial conditions are shown in figure 5.2: blue is liquid and red is gas. The diameter and length of the pipe or channel were 0.05 m and 3.0 m, respectively. One end of the channel or pipe was closed, while the other end was open to the atmosphere. The boundary conditions used for the 2D channel flow and the 3D pipe flow were the same. At the outlet an atmospheric pressure was specified. Inflow through the outlet, if any, is always gas. Initially the left part of the channel or pipe was filled with liquid (blue) and the right part was filled with gas (red). Thus the two phases were initially separated by a virtual dam. Starting the simulation (i.e. removing the dam) allowed the liquid to fall to the gas side and at the same time the gas in the form of a bubble replaces the volume of the discharged liquid. There will be no inflow of gas at the outlet until the liquid has reached the outlet.

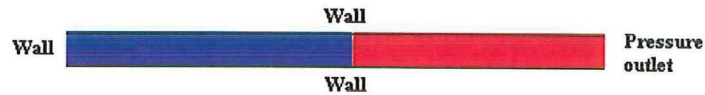


**Figure 5.2:** *Boundary and initial conditions for the Benjamin bubble (blue is liquid and red is gas).*

Two structured mesh configurations were used for the 3D simulations of the Benjamin bubble, see figure 5.3. The first mesh type has a cubic core and the second mesh type has a hexagonal core. A definition for the grid refinement is shown in figure 5.3(b) and in figure 5.3(d).  $X$ ,  $Y$  and  $Z$  denotes the number of grid cells on the edges as defined in figure 5.3(b) and in figure 5.3(d). Grid refinement, which is equivalent to increasing the number of  $X$ ,  $Y$  and  $Z$ , was done in all the directions.

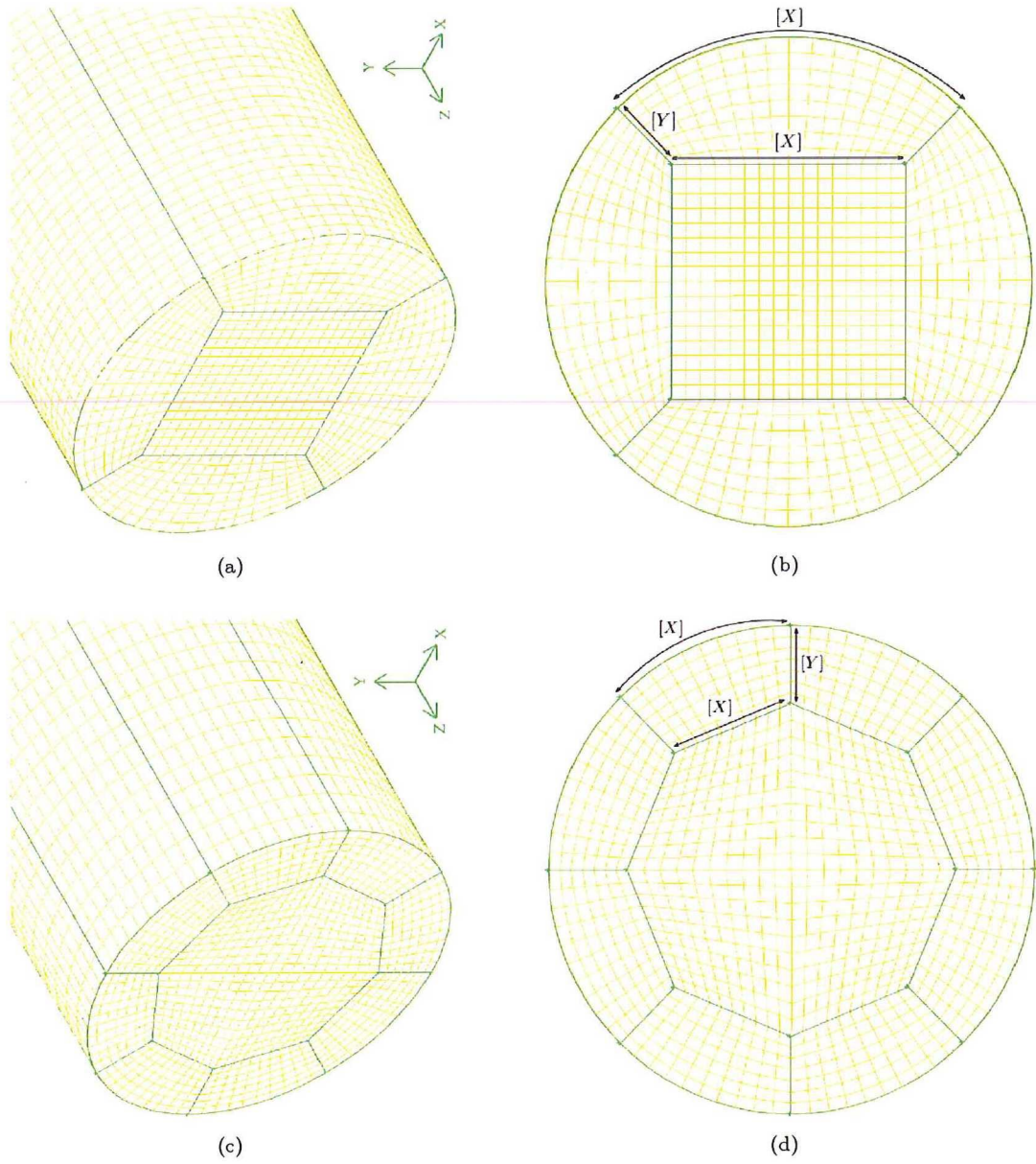


Figure 5.3: (a) and (b) Mesh type 1, (c) and (d) Mesh type 2.

### Convergence criterion

The scaled residual was used as the convergence criterion. The scaled residual in FLUENT is defined as

$$R^\phi = \frac{\sum_{cells P} |\sum_{nb} a_{nb} \phi_{nb} + b - a_P \phi_P|}{\sum_{cells P} |a_P \phi_P|}. \quad (5.24)$$

Here  $a_P$  is the centre coefficient,  $a_{nb}$  are the influence coefficients for the neighbouring cells, and  $b$  is the contribution of the constant part of the source term  $S_c$ . For the momentum equations the denominator term  $a_P \phi_P$  is replaced by  $a_P v_P$ , where  $v_P$  is the magnitude of the velocity at cell  $P$ , see FLUENT (2006). The unscaled residual for the continuity equations is defined as

$$R^c = \sum_{cells P} |\text{rate of mass creation in cell } P|. \quad (5.25)$$

The scaled continuity residual is defined as

$$R_s^c = \frac{R_{iteration N}^c}{R_{iteration 5}^c}, \quad (5.26)$$

where the denominator is the largest absolute value of the continuity residual in the first five iterations.

The value of the scaled residual was set to be  $10^{-6}$  as a convergence criterion in the 2D simulations. In the 3D simulations the value of the scaled residual was set to  $10^{-5}$ . The time step used in the simulations was 0.001 s, which always gave a Courant number (Co) number with a value much lower than unity. Furthermore, the PISO scheme was used for the pressure-velocity coupling. For the pressure interpolation the PRESTO scheme was used and the momentum equation was discretized either with the first order upwind scheme or with the QUICK scheme.

### 5.3.2 Simulation setup for the Dumitrescu or Taylor bubble

The boundary and initial conditions for the simulation of the 2D axisymmetric Dumitrescu bubble are shown in figure 5.4(a). The upper end of the pipe was closed, while the lower end was open to the atmosphere. A constant atmospheric pressure was specified at the pressure outlet. Since the flow is axisymmetric only the domain between the wall and the centre line was modelled. The diameter and the length of the pipe in the 2D axisymmetric simulations was 0.1 m and 1.5 m, respectively. It was necessary to disturb the interface in the 2D axisymmetric simulations in order to have a flow. The interface was disturbed by setting the gravity in the opposite direction for a small time of period. After the interface was disturbed the gravity was set in the normal downward orientation again. Immediately thereafter a bubble was seen to move upward as the liquid was falling downward.

In contrast to the 2D simulations the 3D simulations were started with a pre-defined bubble shape. The bubble shape was initialized by a cosine function, see figure 5.4(b) and Appendix B. In this case it was not necessary to disturb the interface. Note that the bubble shape was initialized with an arbitrarily chosen cosine function. However it turns out that the initial bubble shape is not important, since the bubble adopts very quickly to its equilibrium shape after the simulation is started. Furthermore the diameter and length of the pipe in the 3D simulations was 0.05 m and 3.0 m, respectively.

The simulation settings were similar as for the Benjamin bubble case, except for the time step and the discretization scheme used for the momentum. The time step was 0.0001 s and for the momentum either the first order upwind scheme or the second order upwind scheme was used.

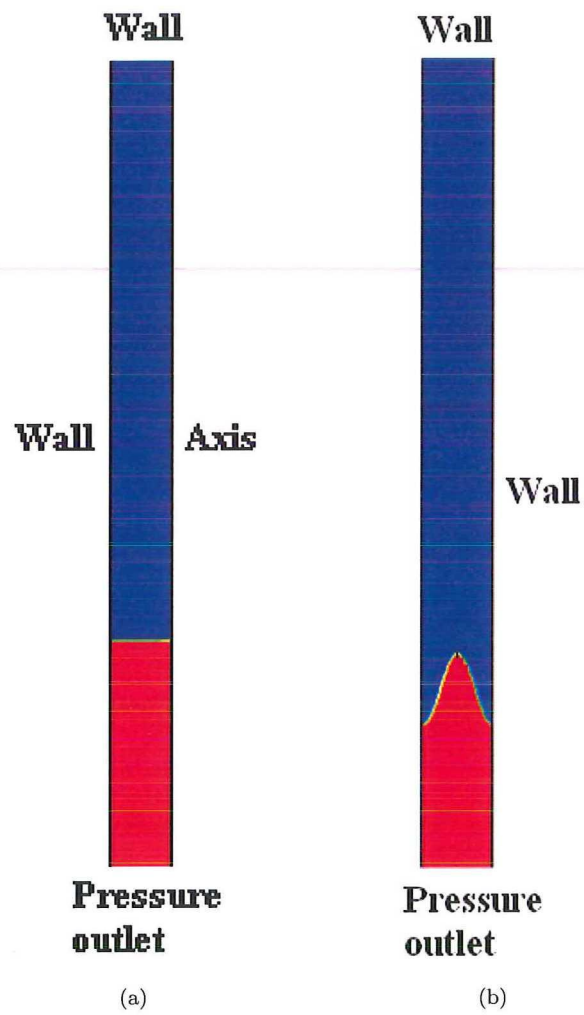


**Figure 5.4:** Boundary and initial conditions for the; (a) 2D axisymmetric Dumitrescu bubble, (b) 3D Dumitrescu bubble (blue is liquid and red is gas).

---

## Chapter 6

# Simulation results for the Benjamin bubble

In this chapter, the simulation results for the Benjamin bubble will be given. First, the results of the inviscid two-dimensional flow are given. Then, the results for the effect of viscosity and surface tension are presented. Finally, the results of the inviscid three-dimensional flow will be given followed by the results of the effect of viscosity and surface tension.

### 6.1 Results for the 2D Benjamin bubble

In order to calculate the bubble velocity, the liquid height and the intersection angle, an iso-surface of  $\alpha = 0.5$  was created. Here  $\alpha$  is the volume fraction of the gas phase. Since in the VOF method the interface is represented by all values between  $\alpha = 0$  and  $\alpha = 1$ , the iso-surface of  $\alpha = 0.5$  represents an average interface. The results below are presented in dimensionless form and the dimensionless parameters are defined hereafter. The bubble velocity is calculated as

$$v_b = \frac{x_2 - x_1}{t_2 - t_1}, \quad (6.1)$$

where  $x_1$  and  $x_2$  are the coordinates of the stagnation point at an old ( $t_1$ ) and new ( $t_2$ ) time level, respectively. The dimensionless bubble velocity is given by

$$v_b^* = \frac{v_b}{\sqrt{gH}}, \quad (6.2)$$

where  $g$  is the gravitational acceleration and  $H$  the channel height. The dimensionless liquid height is described by

$$y^* = \frac{y}{H}, \quad (6.3)$$

where  $y$  is the coordinate at the interface. The asymptotic liquid height, with reference to figure 3.1, is found by replacing the  $y$  coordinate in equation 6.3 by  $h$ . The length of the interface is non-dimensionalized by

$$l^* = \frac{x - x_s}{H}, \quad (6.4)$$

where  $x$  is the coordinate on the interface and  $x_s$  is the coordinate of the stagnation point, i.e. point 0 in figure 3.1. The dimensionless time is given by

$$t^* = t \sqrt{\frac{g}{H}}, \quad (6.5)$$

where  $t$  is the physical time. The grid size is non-dimensionalized as

$$\Delta_i^* = \frac{\Delta_i}{H}, \quad (6.6)$$

where  $\Delta_i$  is the grid size and  $i = x, y$  or  $z$ . The intersection angle,  $\theta$ , near the stagnation point is calculated by

$$\theta = \tan^{-1} \left( \frac{\delta_y}{\delta_x} \right), \quad (6.7)$$

where  $\delta_x$  and  $\delta_y$  are defined in figure 6.1. The interface is represented as a dashed line and the points 0 and 1 correspond with the stagnation point and the numerical point closest to the stagnation point on the interface, respectively.

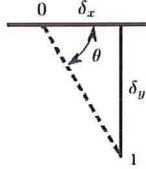


**Figure 6.1:** Intersection angle near the stagnation point.

The results for the dimensionless bubble velocity as a function of the dimensionless time for the two numerical schemes are given in figure 6.2. The results for the dimensionless liquid height as a function

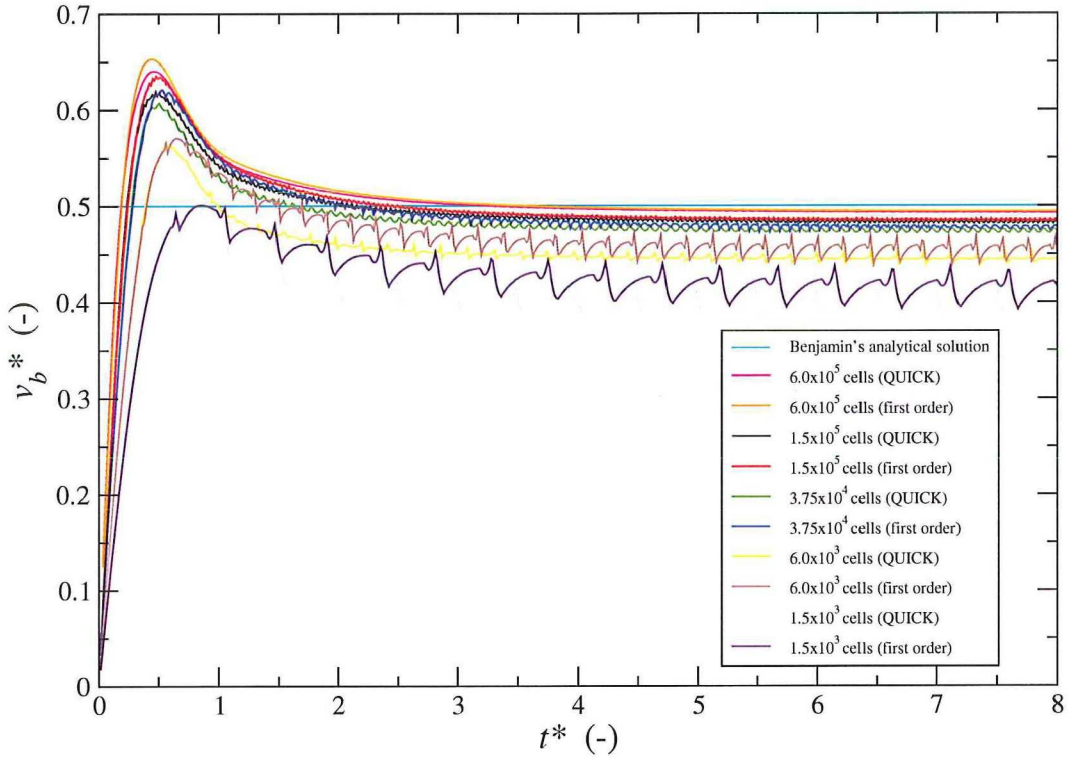


**Figure 6.2:** Comparison of the bubble velocity for the 2D Benjamin bubble.

of the dimensionless length for  $t^* = 56$ , is given in figure 6.3. The results for the different grid sizes for the first order upwind scheme and for the QUICK scheme are summarized in table 6.1 and 6.2, respectively. The values for  $v_b^*$  given in table 6.1 and table 6.2 are averaged values. The averaging is done between  $t^* = 5$  and  $t^* = 10$ . The reported values in table 6.1 and table 6.2 for  $h^*$  are averaged values along the horizontal part of the interface. The results are also shown in figure 6.4 and in figure 6.5. In figure 6.4 the dimensionless bubble velocity is plotted versus the dimensionless grid size, whereas in figure 6.5 the dimensionless liquid height is plotted versus the dimensionless grid size. The

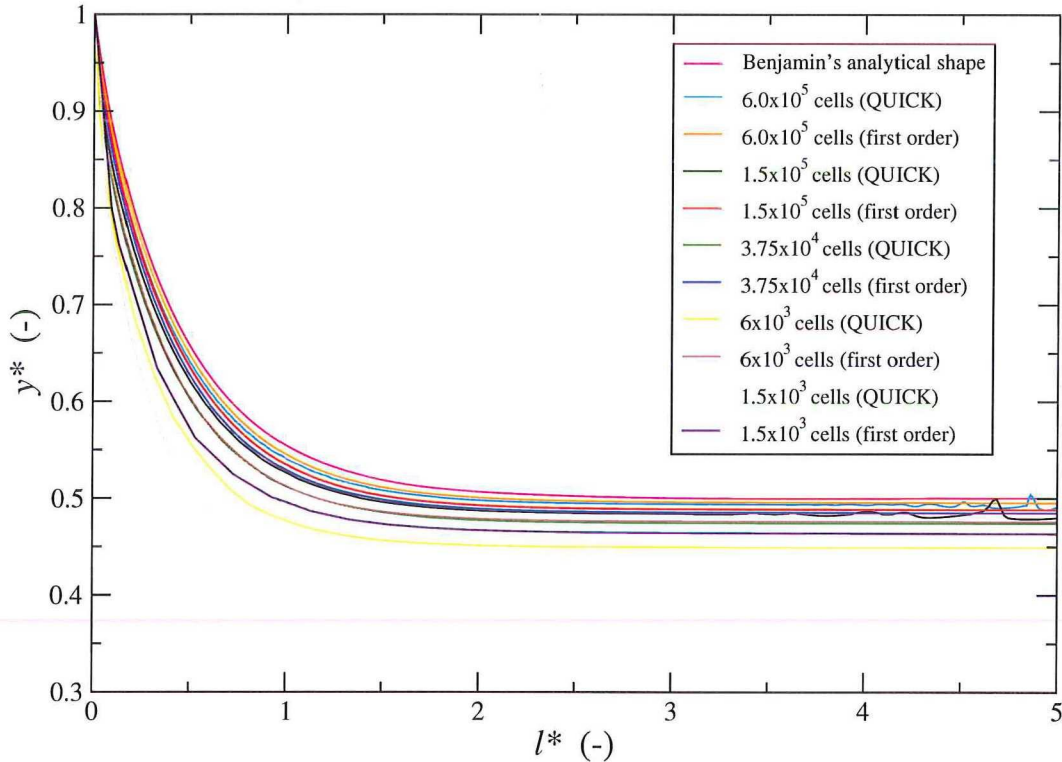


**Figure 6.3:** Comparison of the liquid height for the 2D Benjamin bubble at  $t^* = 56$ .

tables 6.1 and 6.2 also contain extrapolated values for a zero grid size. A linear extrapolation, using the last two solutions on the finer mesh, is performed. The results on the finest mesh and the values of the extrapolation to zero grid size are in excellent agreement with the theoretical result of Benjamin. The experimental data in table 6.1 are also in good agreement with the simulation and theoretical results. Note that there are no inviscid liquids in real life and that surface tension cannot be neglected completely. However the experiments were done under conditions to minimize viscosity and surface tension effects.

Furthermore a striking result is observed in figure 6.4 and in figure 6.5. The first order upwind scheme gives always a better result than the QUICK (third order) scheme. No reason could be found for this.

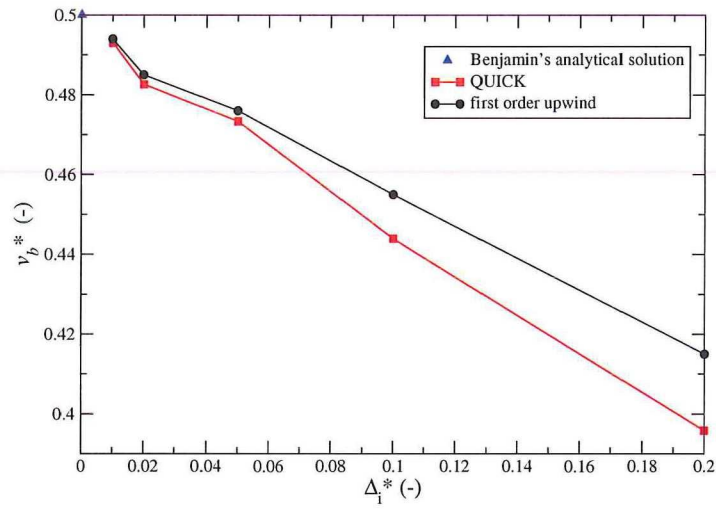
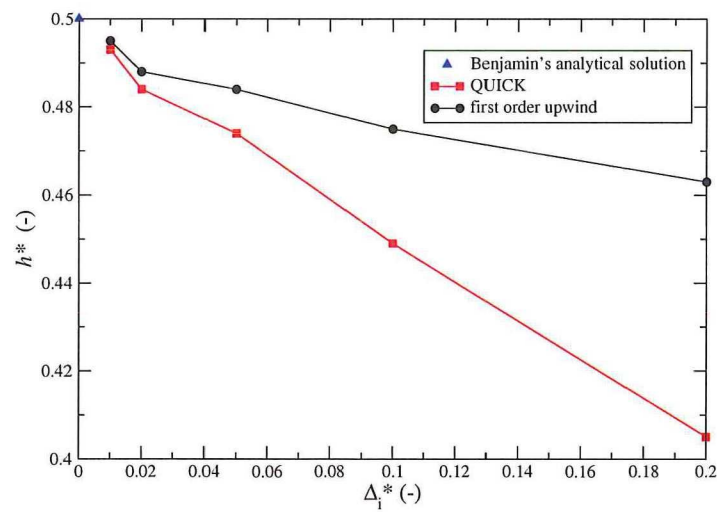
**Table 6.1:** Dimensionless bubble velocity, liquid height and intersection angle for the 2D Benjamin bubble with the first order upwind scheme.

$[\Delta_x^*] \times [\Delta_y^*]$	Total number of grid cells	$v_b^*$	$h^*$	$\theta$ (degree)
[0.2] x [0.2]	1500	0.415	0.463	64.8
[0.1] x [0.1]	6000	0.455	0.475	71.2
[0.05] x [0.05]	37500	0.476	0.484	74.5
[0.02] x [0.02]	150000	0.485	0.488	76.9
[0.01] x [0.01]	600000	0.494	0.495	77.6
Extrapolation		0.503	0.502	-
Analytical solution Benjamin		0.5	0.5	60
Experiment Wilkinson (1982)		0.48	0.48	-
Experiment Baines (1985)		0.47	0.47	-
Experiment Gardner and Crow (1970)		0.49	0.48	-

The bubble profile in the neighbourhood of the nose, for the finest grid and for the different numerical

**Table 6.2:** Dimensionless bubble velocity, liquid height and intersection angle for the 2D Benjamin bubble with the QUICK scheme.

$[\Delta_x^*] \times [\Delta_y^*]$	Total number of grid cells	$v_b^*$	$h^*$	$\theta$ (degree)
[0.2] x [0.2]	1500	0.395	0.405	72.6
[0.1] x [0.1]	6000	0.444	0.449	78.1
[0.05] x [0.05]	37500	0.472	0.474	82.5
[0.02] x [0.02]	150000	0.483	0.484	83.8
[0.01] x [0.01]	600000	0.493	0.493	84.3
Extrapolation		0.503	0.502	-

**Figure 6.4:** Convergence of the numerical solution for the 2D Benjamin bubble: bubble velocity versus grid size.**Figure 6.5:** Convergence of the numerical solution for the 2D Benjamin bubble: liquid height versus grid size.

schemes, is given for  $t^* = 56$  in figure 6.6 together with experimental data and the analytical solution of Benjamin. A good agreement between the predicted, experimental and theoretical shape is found. Although the numerically obtained overall bubble shape is in good agreement with the theoretical profile of Benjamin, the intersection angle  $\theta$  is not consistent with the theoretical value of  $60^\circ$ : the numerical solution gives a significantly larger angle of about  $80^\circ$ .

The evolution of the interface in time, for the two schemes and the finest grid, is given in figure 6.7. Clearly, the interface becomes more and more uniform (horizontal) for increasing time.

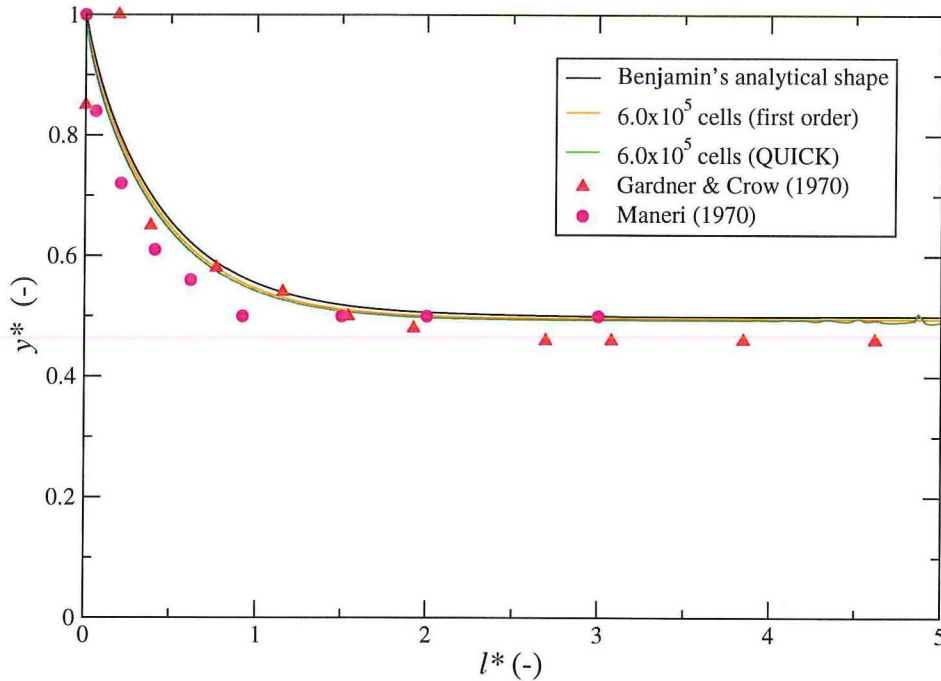


Figure 6.6: Comparison of the bubble profile at  $t^* = 56$  for the 2D Benjamin bubble.

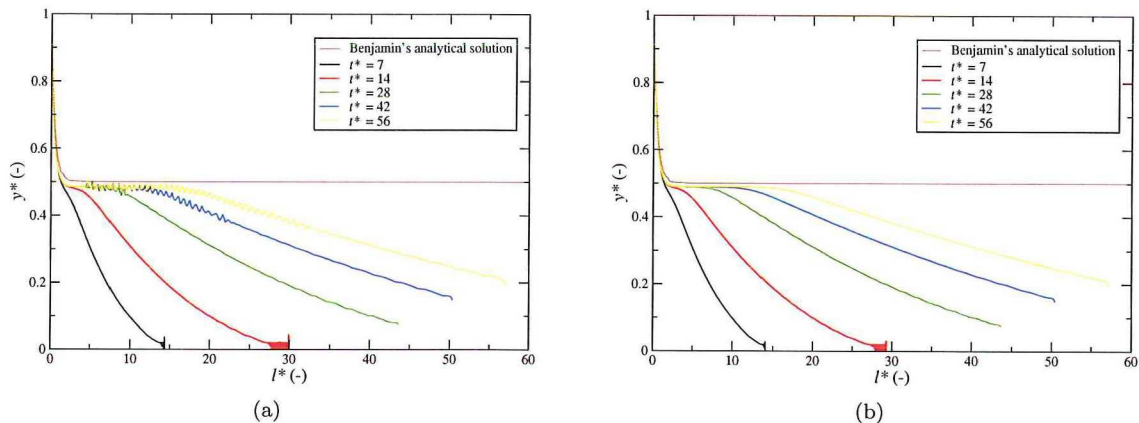


Figure 6.7: Evolution of the interface for the 2D Benjamin bubble: (a) QUICK scheme, (b) first order upwind scheme.

### 6.1.1 Effect of viscosity and surface tension

In this section the effect of viscosity and surface tension on the bubble rise velocity, liquid height and the shape of the bubble will be investigated for the 2D Benjamin bubble. Where possible the results

of these simulations will be compared with experimental data. The dimensionless groups that can be used for correlating experimental data (White and Beardmore, 1962), when the viscosity of the light phase is negligible, are the Froude (Fr) number, the Eötvös (Eo) number and the Morton (Mo) number. These dimensionless numbers are defined as

$$\text{Fr} = \sqrt{\frac{v^2}{gD} \frac{\rho}{\Delta\rho}}, \quad (6.8)$$

$$\text{Eo} = \frac{\Delta\rho g D^2}{\sigma}, \quad (6.9)$$

$$\text{Mo} = \frac{g\mu^4 \Delta\rho}{\rho^2 \sigma^3}, \quad (6.10)$$

where  $v$  is the bubble velocity,  $g$  the gravitational acceleration,  $D$  the tube diameter (replaced by  $H$  for channel flow),  $\rho$  the heavy phase density,  $\Delta\rho$  the density difference,  $\sigma$  the surface tension and  $\mu$  the heavy phase viscosity. However, it is also possible to use the Reynolds number (Re), instead of the Morton number, as a measure for viscous effects (see Appendix A). In the experiments, to be discussed below, some authors used a dimensionless surface tension parameter  $\Sigma$ , instead of the Eötvös number to account for surface tension effects. This dimensionless surface tension parameter is in fact the reciprocal of the Eötvös number and was defined by Gardner and Crow (1970) as

$$\Sigma = \frac{4\sigma}{\Delta\rho g H^2}. \quad (6.11)$$

The experiments were carried out in a channel, and therefore the channel height  $H$  was used as the characteristic length. Several cases were modeled with varying viscosity and surface tension. Table 6.3 gives an overview of the simulated cases. For convenience also a characteristic Reynolds number was defined as

$$\text{Re} = \left(\frac{\text{Eo}^3}{\text{Mo}}\right)^{\frac{1}{4}} = \frac{\rho H \sqrt{gH}}{\mu}, \quad (6.12)$$

where  $\sqrt{gH}$  is a characteristic velocity. Equation 6.12 is also referred to as Galileo (Ga) number. The

**Table 6.3:** Overview of the modeled cases

Case	Density (kg/m <sup>3</sup> )	$\mu$ (Pa·s)	$\sigma$ (N/m)	$\Sigma$ ( $\times 10^{-3}$ )	Mo	Re (eqn. 6.12)	Eo
1	998.2	0.00036	0.0184	3.0	$2.53 \times 10^{-11}$	99045	1333
2	998.2	0.00063	0.04	6.5	$2.53 \times 10^{-11}$	55136	615
3	998.2	0.00154	0.13	21.2	$2.53 \times 10^{-11}$	22718	189
4	998.2	0.00968	1.51	246	$2.53 \times 10^{-11}$	3613	16
5	873	0.121	0.02	3.74	$3.01 \times 10^{-1}$	253	1071
6	889	0.692	0.02	3.67	$3.16 \times 10^2$	45	1090
7	889	1.200	0.02	3.67	$2.86 \times 10^3$	26	1090

first case in table 6.3 is similar to the experiment of Wilkinson (1982) in a channel with  $H = 100$  mm. The cases 2 to 4 in table 6.3 correspond with the experimental study of Gardner and Crow (1970), where they investigated the effect of the surface tension on the bubble velocity and on the bubble profile in a channel. Wilkinson and Gardner & Crow used air and water in the experiments and therefore the Morton number (or the Reynolds number) was fixed. Gardner & Crow varied the dimensionless surface tension parameter  $\Sigma$  (or the Eötvös number) by varying the height of the channel. As all the simulations were done in a channel with  $H = 5$  cm, the viscosity was set accordingly to keep the Morton number (or the Reynolds number) similar as in the experiments. The last three cases in table 6.3 are randomly chosen, but the aim was to investigate the effect of viscosity on the bubble velocity and on the bubble profile. It should be noted that the chosen viscosities of 0.121, 0.692 and 1.2 Pa·s are quite high (i.e. viscosity of water is 0.001 Pa·s), but not unusual for heavy oil production. A surface tension of 0.02 N/m was used, which is typical for an air-oil system.

### Results for the effect of surface tension

The results for the effect of surface tension on the bubble velocity for the 2D Benjamin bubble are given in figure 6.8. Average values are reported in table 6.4. Clearly the surface tension reduces the bubble velocity. For low and moderate surface tension the bubble quickly reaches its final velocity which remains constant thereafter. However for a high surface tension a fluctuation in the bubble velocity is seen. The authors of the study with the experiments in case 1 to 4 also reported a minimum dimensionless liquid height  $h_m^*$ , which is the minimum liquid height just after the bubble nose, as defined in figure 6.10.

A comparison between the experimental data of Wilkinson (1982) and of Gardner and Crow (1970) and the simulation results for the bubble velocity and for the minimum liquid height is given in figure 6.9 and figure 6.10, respectively. Good agreement between the simulation results and the experimental data is observed for the cases 1 to 3. The simulation results for case 4 are not in agreement with the experimental data. The reason for this disagreement is the so-called spurious or parasite currents, which occur in regimes dominated by the surface tension. The nature of these parasite currents will be discussed in more detail below.

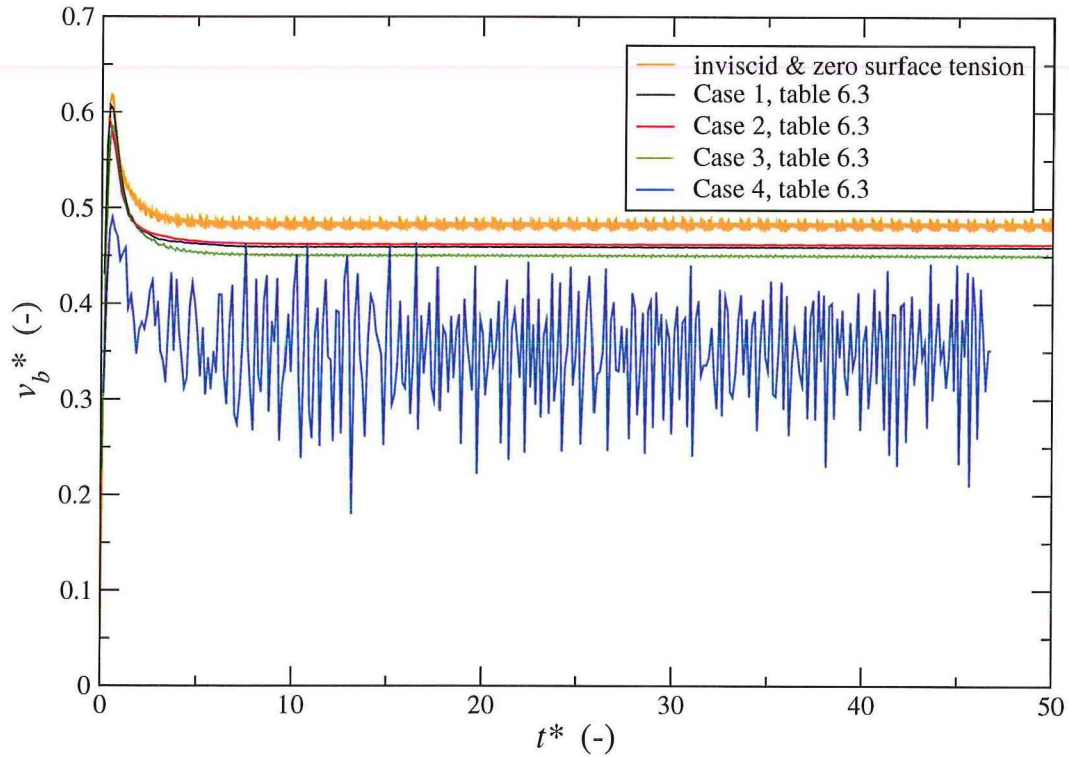


Figure 6.8: Comparison of the bubble velocity for the 2D Benjamin bubble.

Table 6.4: Results for the effect of the surface tension on the 2D Benjamin bubble.

Case	$v_b^*$		$h_m^*$	
	Experiment	Simulation	Experiment	Simulation
1	0.468	0.459	0.48	0.47
2	0.44	0.462	0.48	0.475
3	0.42	0.449	0.45	0.464
4	0.2	0.349	0.47	0.435

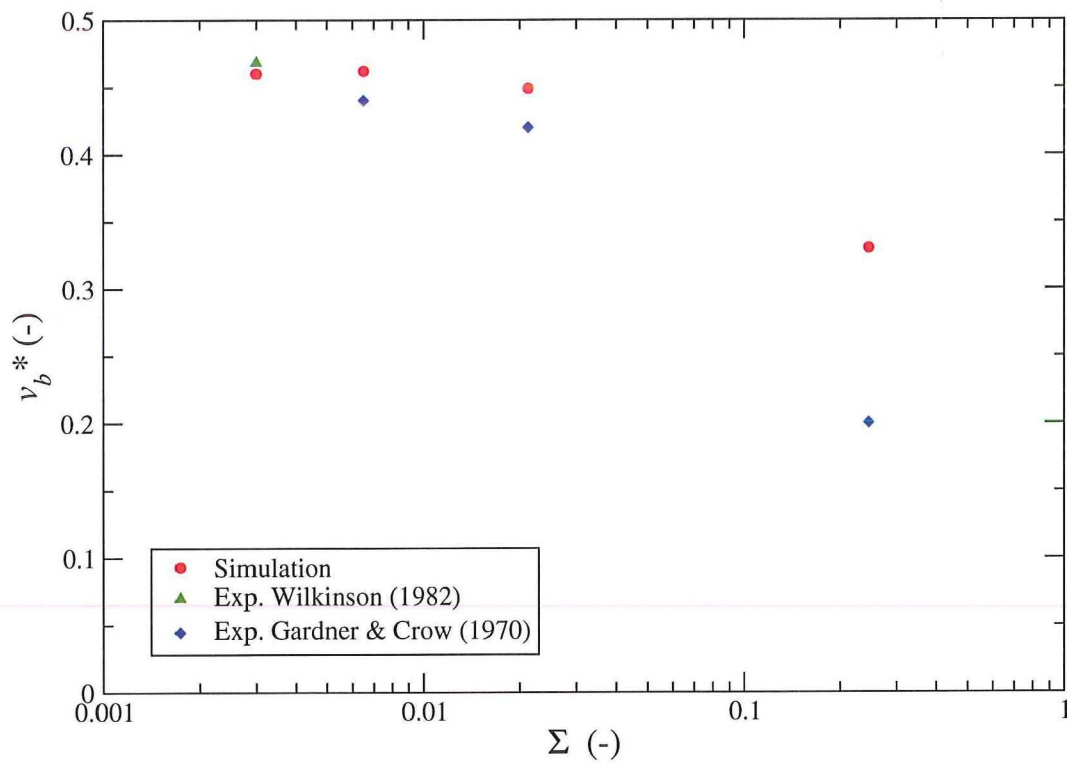


Figure 6.9: Comparison of the velocity for the 2D Benjamin bubble.

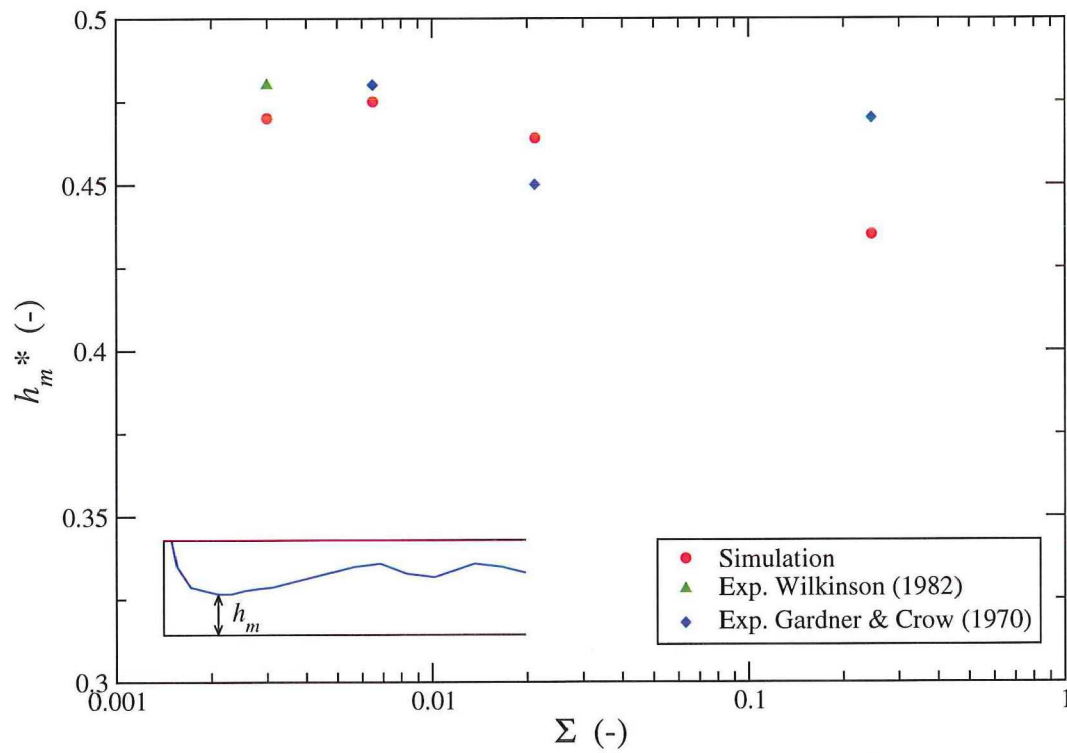


Figure 6.10: Comparison of the minimum liquid height for the 2D Benjamin bubble.

### Parasite currents

The spurious or parasite currents in the simulations are vortices which appear in the neighbourhood of the interface region despite the absence of any external forcing (Scardovelli and Zaleski, 1999). These parasite currents are clearly seen in figure 6.11(a) for the simulations for case 4. The bubble shape, figure 6.11(b), is also influenced by these parasite currents, which tend to destroy the interface. The parasite currents scale with the surface tension and with the viscosity, see Lafaurie et al. (1994). A dimensional analysis (Lafaurie et al., 1994) reveals that

$$K = \frac{u_{max}\mu}{\sigma}. \quad (6.13)$$

Here  $u_{max}$  is the maximum velocity due to the parasite currents,  $\mu$  the viscosity,  $\sigma$  the surface tension and  $K$  is a dimensionless constant without any physical meaning, but characteristic for these parasite currents. The magnitude of the parasite currents increases with decreasing viscosity and increasing surface tension, see Ubbink (1997) and Lafaurie et al. (1994). Thus parasite currents may be observed in flows dominated by the surface tension, as in case 4 of table 6.3. The origin of these spurious currents

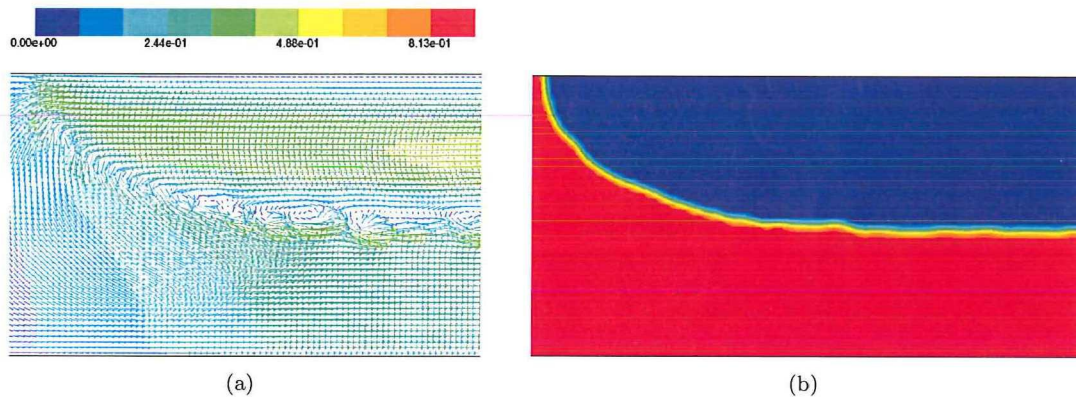


**Figure 6.11:** (a) Plot of velocity vectors, (b) bubble shape close to nose (Case 4 table 6.3).

lies in the Continuum Surface Force (CSF) model of Brackbill et al. (1992), which is implemented in FLUENT to account for the surface tension. The spurious currents are a well-known drawback of the VOF method. They originate from the calculation of the interfacial curvature in the CSF model. Since the interface is smeared out over several cells the curvature becomes oscillatory and as a consequence these spurious currents arise.

### Effect of surface tension on bubble profile

An increasing surface tension results in a decreasing bubble velocity, as observed in the experiments and in the simulations. However, Gardner and Crow (1970) observed that also the bubble profile was influenced for  $0.02 < \Sigma < 0.105$  and large waves were formed downstream of the bubble nose. Case 2 of table 6.3 lies in this range and a photograph of the experiments for this case was provided by Gardner and Crow. A comparison between the experimentally obtained bubble profile and the simulation is given in figure 6.12. Although the bubble velocity and the minimum liquid height (see table 6.4 case 2) are in fair agreement with the experimental data, the bubble profile is not consistent with the experiments. A possible reason for this deviation is how the experiments were performed. Gardner and Crow (1970) used a sill at the end of the channel to have a better drainage. Furthermore, one end of the channel was closed by a fixed wall while the other end was sealed with a flap. Releasing this flap allowed the liquid to flow out, but at the same time this allowed air to enter the channel. However by releasing the flap a disturbance might be created. Gardner and Crow report that a surface elevation was created by releasing the flap, but that it decayed rapidly. Since the flow, under the conditions of case 2, is subcritical according to Gardner and Crow (1970) small disturbances in the form of a wave may travel upstream. The sill used for a better drainage may also create some disturbances. In order to check the influence of downstream disturbances one additional simulation, corresponding with the experimental conditions in the study of Wilkinson (1982), was performed. The results of this simulation are discussed below.

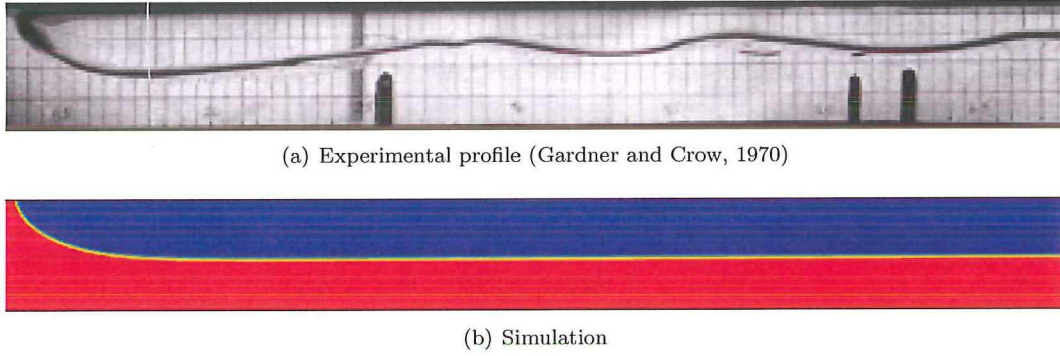


Figure 6.12: Comparison of the 2D bubble profile for  $\Sigma = 0.0212$ .

### Effect of downstream disturbances

The experimental setup of Wilkinson is shown in figure 6.13. Wilkinson used a control weir at the outlet of the channel to control the outflow. Except for the weir the experimental setup was the same as for case 1 of table 6.3. The height of the weir was  $H/3$ , where  $H$  denotes the height of the channel. The weir was modeled as a wall in the simulation. Figure 6.14 compares the bubble profile of the simulation with the experimental profile at different time instants.

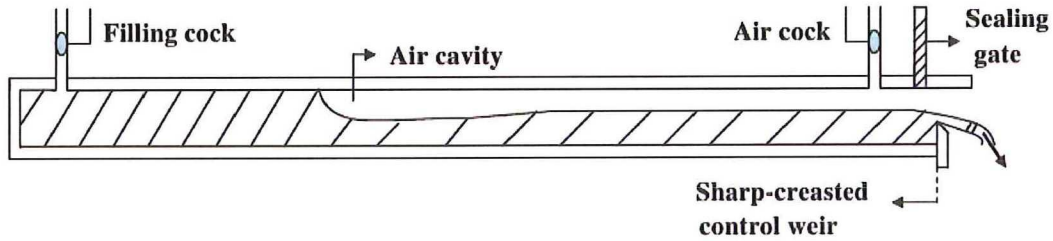


Figure 6.13: Experimental setup for the 2D Benjamin bubble (Wilkinson, 1982).

Clearly, disturbances are created at the outlet that travel upstream in the form of a wave. The qualitative flow behaviour in the simulations is in good agreement with the experiments. The bubble velocity in the cases with or without weir is plotted in figure 6.15. The bubble velocity is not influenced by the travelling waves, which is in agreement with the observation of Wilkinson. Furthermore, Wilkinson observed that the length of the frontal region of the bubble was increasing with time. This fact is also seen in the simulation in figure 6.16. A more quantitative comparison is given in table 6.5. The simulation results are not only qualitatively, but also quantitatively in good agreement with the experiments. These results suggest that the change of the bubble profile for case 2, mentioned in the previous section, is likely due to disturbances created at the outlet during the experiments and not due to surface tension as presumed by Gardner and Crow (1970). However, it is clear that high quality measurements and well defined boundary conditions in the experiments are required to be able to validate a CFD code.

Table 6.5: Comparison of simulation results with experimental data for the 2D Benjamin bubble.

Case	$v_b^*$		$h_m^*$	
	Experiment	Simulation	Experiment	Simulation
without weir	0.468	0.459	0.48	0.47
with weir	0.46	0.462	0.48	0.472

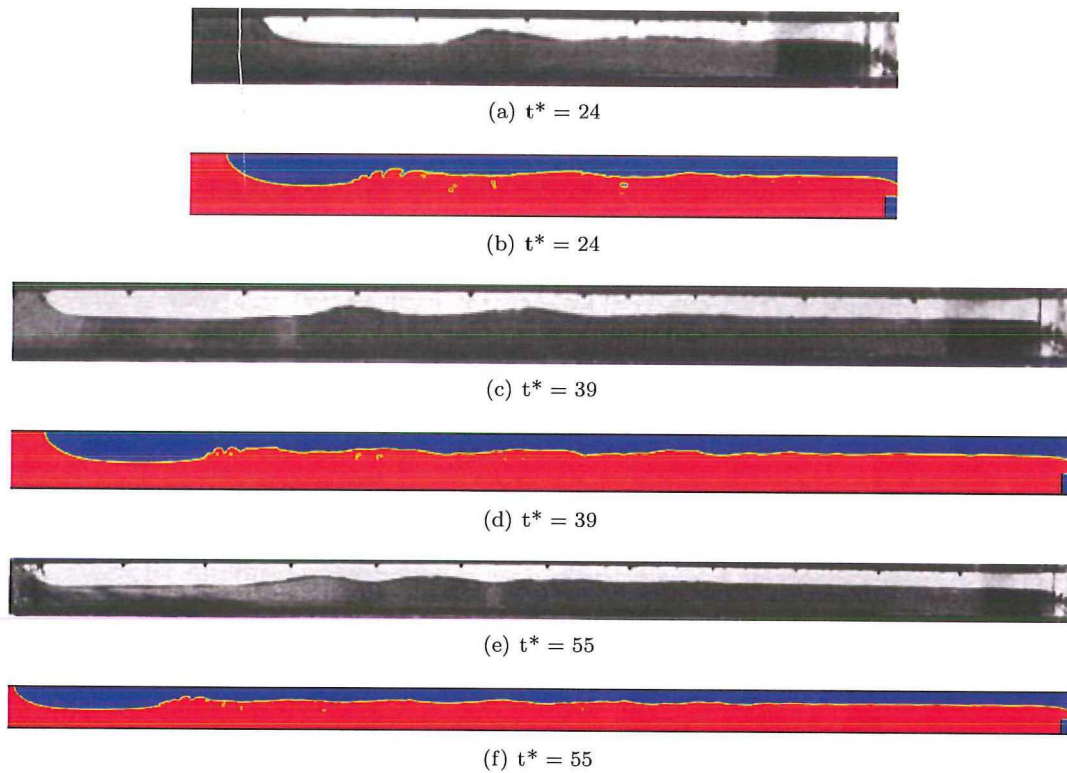


Figure 6.14: (a), (c) and (e) experiment (Wilkinson, 1982) and (b), (d) and (f) simulation Fluent.

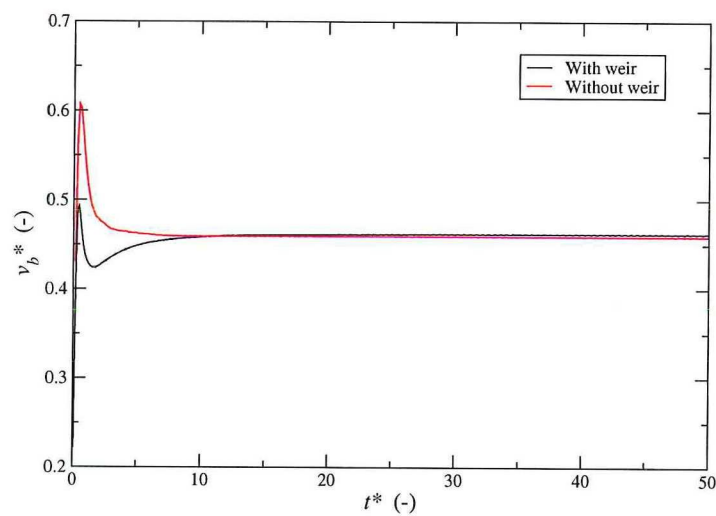


Figure 6.15: Bubble velocity for a simulation with a weir and without a weir.

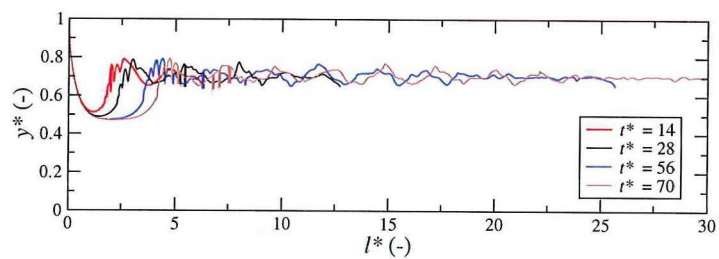


Figure 6.16: Bubble shape for different time instants.

### Results for the effect of viscosity

The effect of viscosity on the bubble velocity of the 2D Benjamin bubble is shown in figure 6.17. The cases correspond with the cases given in table 6.3. It can be seen in figure 6.17 that the bubble velocity decreases with increasing viscosity. Furthermore, the bubble velocity decreases in time for all the three cases and will probably never reach a constant value. Instead the bubble will come to standstill after a long time. Case 7 of table 6.3 will be analyzed here, but the characteristics for the other two cases with viscosity are similar. The decrease in bubble velocity can readily be understood, since the energy losses, due to boundary friction, increases as the liquid layer beneath the bubble increases in time. This is in agreement with a viscous experimental observation of Wilkinson (1982). The bubble profile at different time instants for case 7 is shown in figure 6.18. Clearly the liquid layer beneath the bubble cannot be regarded as uniform and as a consequence of this the bubble velocity changes. Furthermore, as we can see in figure 6.18 the bubble becomes thinner and thinner in time. We can also observe in this figure that the liquid drainage close to the bubble nose is incomplete, hence a thin liquid layer is observed above the bubble in the neighbourhood of the nose. Note that this is not strange since Wilkinson (1982) and other authors also observed this fact in experiments. What seems to be strange is the falling droplets, as can be observed in figure 6.18(b). This might be a numerical artifact.

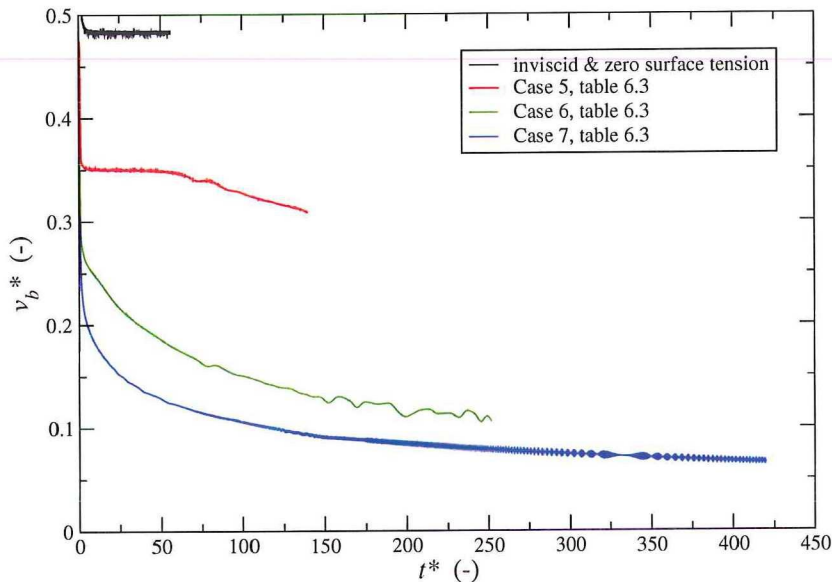


Figure 6.17: Effect of viscosity for the 2D Benjamin bubble.

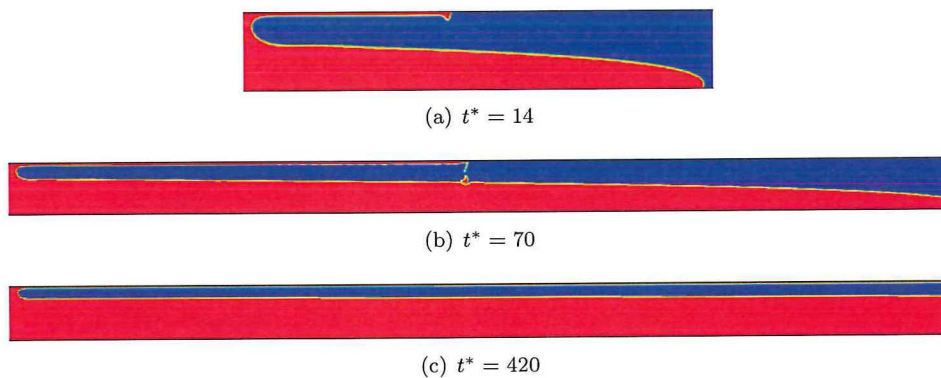
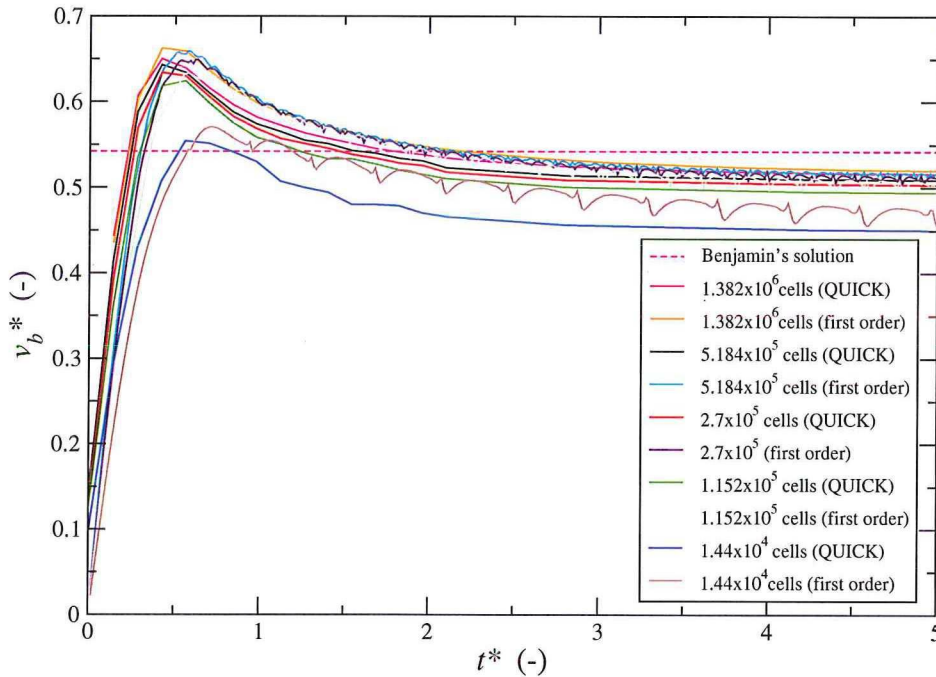


Figure 6.18: Bubble profiles at different time instants for the 2D Benjamin bubble (case 7, table 6.3).

## 6.2 Results for the 3D Benjamin bubble in a pipe

The results will be presented in dimensionless form. The dimensionless numbers are the same as defined for the two dimensional channel flow, except for the height  $H$  which is replaced by the diameter  $D$  of the pipe. Two mesh types, see figure 5.3, and discretization schemes were investigated. The reason for using two mesh types may become clear while discussing the results.

The results for the bubble velocity for the first mesh type with different grid sizes are given in figure 6.19. The bubble velocity tends to approach the theoretical value of Benjamin (1968) as the grid is refined. Furthermore, the bubble reaches very quickly, after  $t^* > 2.5$ , its final velocity. The results for the liquid height are given in figure 6.20. Clearly the interface consist of small waves, but the amplitude of these waves becomes smaller when the grid is refined. This suggests that the observed waves are of numerical nature, instead of being physical. However a second mesh type, see figure 5.3, was used to check the influence on these waves. The waves were also seen on this mesh configuration. The results of the first mesh type are summarized in table 6.6 and table 6.7 for the first order and second order scheme, respectively. Although the results on the second mesh type were comparable with the results on the first mesh type, it was decided to report also those results, see table 6.8. Note that the mentioned wavy interface was seen on both mesh types and the mentioned liquid height in tables 6.6, 6.7 and 6.8 are average values. In the case of the second mesh type only the QUICK scheme was explored. Although the interface is wavy, due to numerical artifact, the average liquid height is very close to the analytical value of Benjamin. Further, the tables 6.6, 6.7 and 6.8 contain extrapolated values for zero grid size. The difference between these extrapolated values and the analytical values are less then 3%. The experimental data given in table 6.6 is also in good agreement with the simulation results. However it should be realized that viscosity and surface tension cannot be ignored completely in real life experiments.



**Figure 6.19:** Comparison of the bubble velocity for the 3D Benjamin bubble in a pipe.

For convenience the results are also shown in figure 6.21(a) and figure 6.21(b), in which the results are plotted versus the dimensionless grid size. The grid size was non-dimensionalized as

$$\Delta_i^* = \frac{\sqrt{\frac{\pi D^2}{4n}}}{D}, \quad (6.14)$$

where  $D$  is the diameter of the pipe and  $n$  the number of grid cells in the cross-section of the pipe.

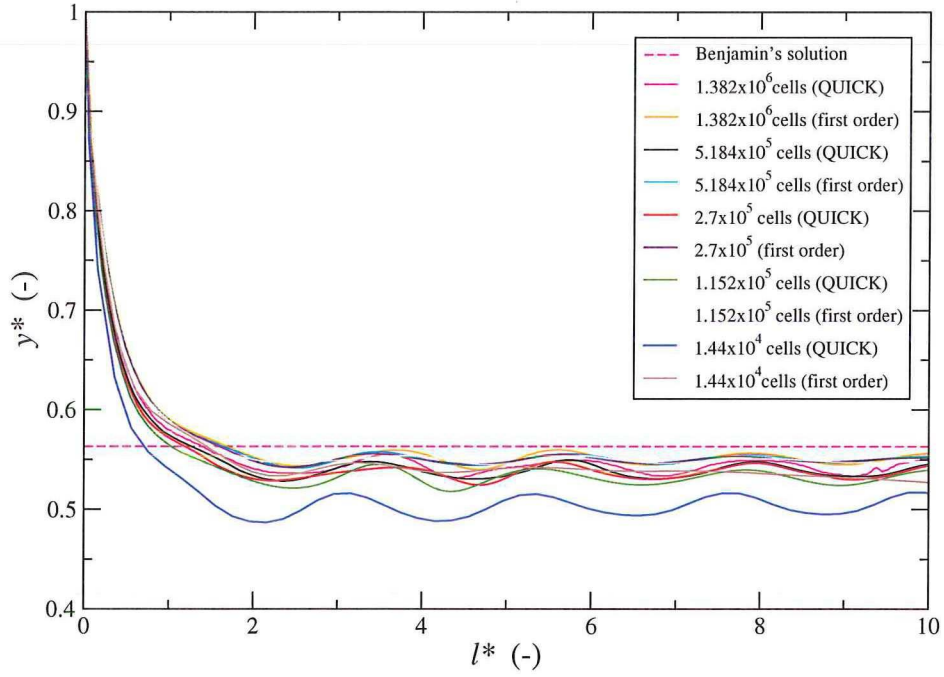


Figure 6.20: Comparison of the liquid height for the 3D Benjamin bubble in a pipe.

Table 6.6: Dimensionless bubble velocity and liquid height for the 3D Benjamin bubble in a pipe (cubic mesh and first order scheme).

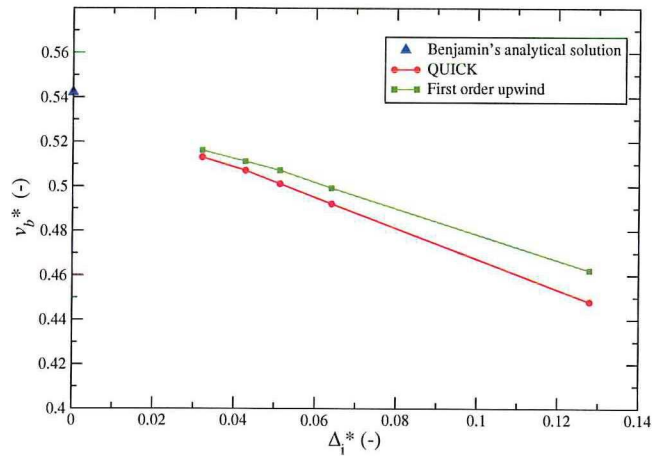
Interval [X] x [Y] x [Z]	Total number of grid cells	$v_b^*$	$h^*$
[4] x [2] x [300]	14400	0.462	0.539
[8] x [4] x [600]	115200	0.499	0.549
[10] x [5] x [900]	270000	0.507	0.55
[12] x [6] x [1200]	518400	0.511	0.5504
[16] x [8] x [1800]	1382400	0.516	0.5513
Extrapolation		0.531	0.554
Analytical solution Benjamin		0.542	0.563
Experiment Gokcal (2008)		0.5	0.62
Experiment Hager (1999)		0.6	0.63
Experiment Zukoski (1966)		0.53	-
Experiment Bendiksen (1984)		0.53	-

Table 6.7: Dimensionless bubble velocity and liquid height for the 3D Benjamin bubble in a pipe (cubic mesh and QUICK scheme).

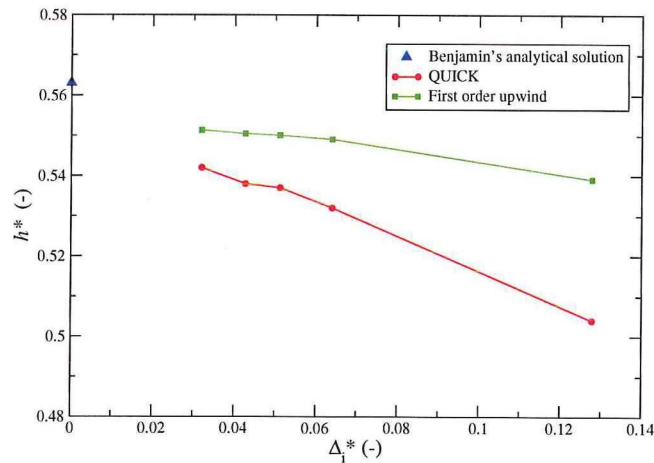
Interval [X] x [Y] x [Z]	Total number of grid cells	$v_b^*$	$h^*$
[4] x [2] x [300]	14400	0.448	0.504
[8] x [4] x [600]	115200	0.492	0.532
[10] x [5] x [900]	270000	0.501	0.537
[12] x [6] x [1200]	518400	0.507	0.538
[16] x [8] x [1800]	1382400	0.513	0.542
Extrapolation		0.531	0.554

**Table 6.8:** Dimensionless bubble velocity and liquid height for the 3D Benjamin bubble in a pipe (hexagonal mesh and QUICK scheme).

Interval $[X] \times [Y] \times [Z]$	Total number of grid cells	$v_b^*$	$h^*$
$[2] \times [1] \times [300]$	9600	0.428	0.485
$[5] \times [3] \times [500]$	110000	0.495	0.532
$[8] \times [5] \times [750]$	432000	0.51	0.543
$[10] \times [7] \times [900]$	864000	0.517	0.546
Extrapolation		0.541	0.556



(a)



(b)

**Figure 6.21:** Convergence of the numerical solution for the 3D Benjamin bubble:(a) bubble velocity versus grid size , (b) liquid height versus grid size.

### 6.2.1 Effect of viscosity and surface tension for the 3D Benjamin bubble in a pipe

In this section the influence of viscosity and surface tension on the bubble velocity will be investigated. The results of the simulation will be compared with the experimental work of Zukoski (1966) and Gokcal (2008). Zukoski investigated the effect of viscosity and surface tension in a vertical, horizontal and inclined pipe. Gokcal investigated the effect of high viscosity oil on the bubble velocity in a horizontal pipe. In presenting the experimental results Zukoski used the Reynolds number (Re), based on the bubble velocity, as a measure for viscous effects and he defined this by

$$\text{Re} = \frac{\rho v_b a}{\mu}, \quad (6.15)$$

where  $\rho$  and  $\mu$  are the density and viscosity, respectively, of the liquid in which the bubble is propagating,  $v_b$  is the bubble velocity and  $a$  the tube radius. The parameter that accounts for the surface tension was defined by Zukoski as

$$\Sigma = \frac{\sigma}{\Delta \rho g a^2}, \quad (6.16)$$

which is the reciprocal of the more commonly used Bond (Bd) or Eötvös (Eo) number. Although the definition of the Reynolds number is correct for correlating experimental data, it is not convenient for simulation purposes. The reason for this is that the bubble velocity is a result of the simulation and is unknown prior to the simulation. Five cases, listed in table 6.9, are simulated to check the influence of viscosity and surface tension on the bubble velocity. The first three cases in table 6.9 are

**Table 6.9:** Overview of the modeled cases for the 3D Benjamin bubble in a pipe

Case	Density (kg/m <sup>3</sup> )	$\mu$ (Pa·s)	$\sigma$ (N/m)	$\Sigma$ ( $\times 10^{-3}$ )	Re (eqn. 6.15) Experiment	Re = $\frac{\rho D \sqrt{g D}}{\mu}$
1	998.2	0.00087	0.061	10	9290	40217
2	998.2	0.00352	0.392	64	1787	9925
3	998.2	0.0102	1.64	268	205	3412
4	873	0.121	0.0325	6.07	-	253
5	889	0.692	0.0325	5.96	-	45

meant to investigate the effect of the surface tension and correspond with the experimental work of Zukoski (1966) in the sense that  $\Sigma$  is kept the same as in the experiment. Zukoski used different tube diameters to influence the dimensionless surface tension parameter  $\Sigma$ . However, in all the simulations a 5 cm diameter pipe was used and the surface tension,  $\sigma$ , was changed to match the experimental  $\Sigma$ . The experimental Reynolds numbers, based on equation 6.15, are mentioned in table 6.9. It is not possible to keep the Reynolds numbers exactly identical as in the experiments. The reason for this, as explained earlier, is that the definition of the Reynolds number (eqn. 6.15) contains the bubble velocity, which is a result of the simulation itself and unknown in advance. To overcome this problem, it was assumed that the simulation will reproduce the experimentally obtained dimensionless bubble velocity, hence also the Reynolds number. Then, the viscosity was changed accordingly as given in table 6.9. In the case that the simulation fails to predict the experimental dimensionless bubble velocity, the experimental Reynolds number will differ from the simulated Reynolds number. The last two cases in table 6.9 are identical to the experimental investigation of Gokcal (2008) and numerical simulation of Andreussi and Bonizzi (2009). It is evident that in the last two cases the effect of surface tension is minimal and that the flow is dominated by viscous forces.

#### Results for the effect of surface tension

The results of the simulations to account for the surface tension effects on the bubble velocity are shown in figure 6.22. In the first two cases the bubble reaches, within five dimensionless time units, a constant velocity. In contrast to this, in the third case the dimensionless bubble velocity is fluctuating from almost zero to 0.5. Note that Zukoski also observed an unsteady propagation rate of the bubble for  $\Sigma > 0.1$ , similar as we found in the third case. Zukoski observed in his experiments that the bubbles did not propagate steadily if, owing to surface tension,  $v_b^*$  was lower than about 0.35. The reason for this is

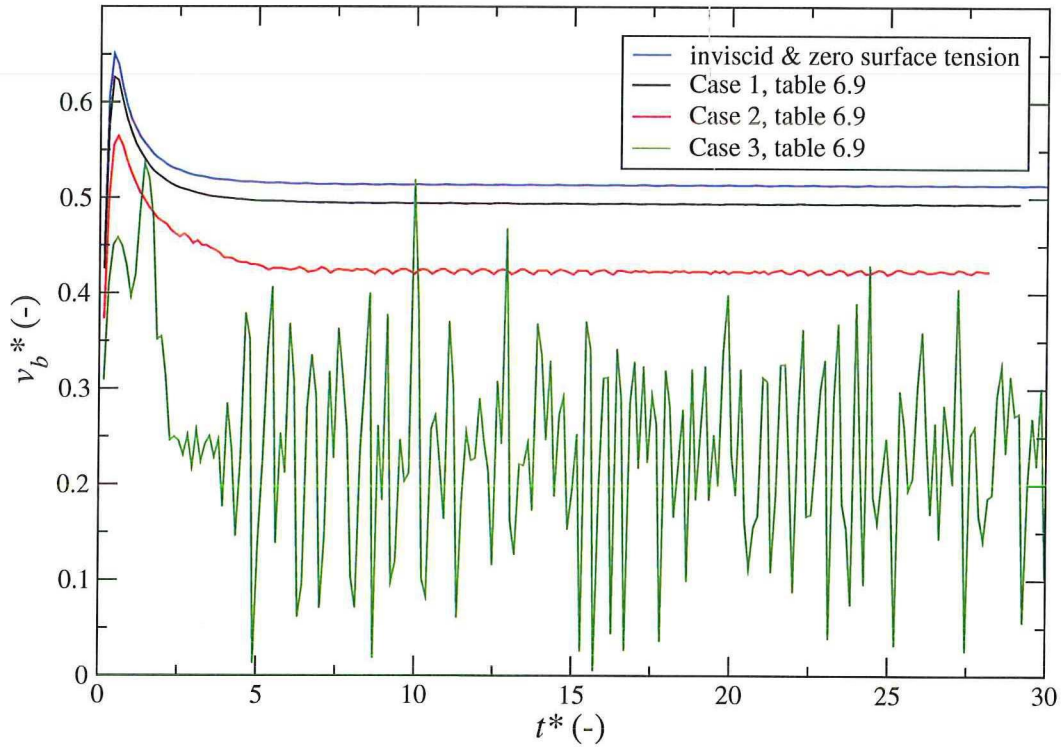


**Figure 6.22:** Simulations for the bubble velocity for the 3D Benjamin bubble in a pipe.

that the flow beneath the bubble becomes subcritical (i.e.  $Fr \leq 1$ ) for  $v_b^* \leq 0.35$ . This implies that small disturbances at the outlet or downstream of the bubble can travel upstream and overtake the bubble and therefore no steady flow can be established. For  $v_b^* \geq 0.35$  the flow is supercritical (i.e.  $Fr > 1$ ) the disturbances cannot travel upstream and a steady flow must evolve. Note that for the inviscid case, without surface tension, the Froude number was given by equation 3.40 and the associated flow is supercritical. A comparison between the experimental data of Zukoski and the simulations is given in table 6.10. In the third case an average value for the bubble velocity is reported. It is clear from table

**Table 6.10:** Comparison of the bubble velocity for the 3D Benjamin bubble in a pipe.

Case	$\Sigma$ ( $\times 10^{-3}$ )	$v_b^*$		Re	
		Experiment	Simulation	Experiment	Simulation
1	10	0.462	0.494	9290	9934
2	64	0.36	0.423	1787	2099
3	268	0.12	0.234	205	399

6.10, that the dimensionless bubble velocity predicted by FLUENT is somewhat higher in the first two cases and almost two times higher in the third case. Thus, the initial assumption that the simulation will reproduce the experimental dimensionless bubble velocity is not satisfied and hence the simulation Reynolds number is somewhat higher. However, the differences between the simulated dimensionless bubble velocities and the experiments is not due to the differences in the Reynolds numbers. This conclusion is based on the observation of Zukoski, who found that for  $Re > 200$  the viscous effects were negligible. Since, in all the cases  $Re > 200$  it is unlikely that viscous effects play a role. Instead differences in the bubble velocity in the three cases are solely due to the effect of surface tension. The reason for the large difference in the third case is the presence of the parasite currents. As explained earlier this parasite currents appear in flows dominated by the surface tension, as in case 3 of table 6.9. The velocity vectors are plotted in figure 6.23(a) and again vortices are seen at the interface. The explanation for the difference between the simulation and the experiment for the first two cases in table 6.10 is less obvious, but the results may be improved by using a finer mesh.

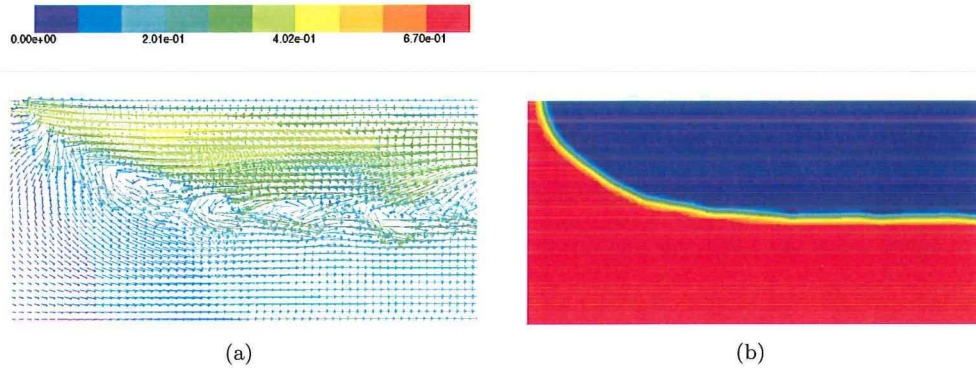


Figure 6.23: (a) Plot of velocity vectors, (b) bubble shape close to nose (Case 3 table 6.9).

### Results for the effect of viscosity

The results for the bubble velocity as a function of the length for the cases 4 and 5 are given in figure 6.24, together with the simulation results of Andreussi and Bonizzi (2009). The bubble velocity versus the dimensionless time together with the experimental data is given in figure 6.25. Clearly, the bubble velocity decreases in time for the two viscous cases, while the velocity in the inviscid case reaches a constant value. This means that the velocity measured by Gokcal (2008) should be considered as the bubble velocity at a given distance and time after starting the experiment. The reported values in figure 6.25 was measured by Gokcal (2008) after three seconds, which corresponds with  $t^* = 42$ . The bubble velocity reported by Gokcal for case 5 is in good agreement with the simulation, while the agreement for case 4 is less satisfactory. The reason for this disagreement is not known. However it should be noted that the bubble velocity decreases in time, and hence the actual time of measurements and the initial (boundary) conditions to initiate the bubble motion should be the same to be able to make a meaningful comparison.

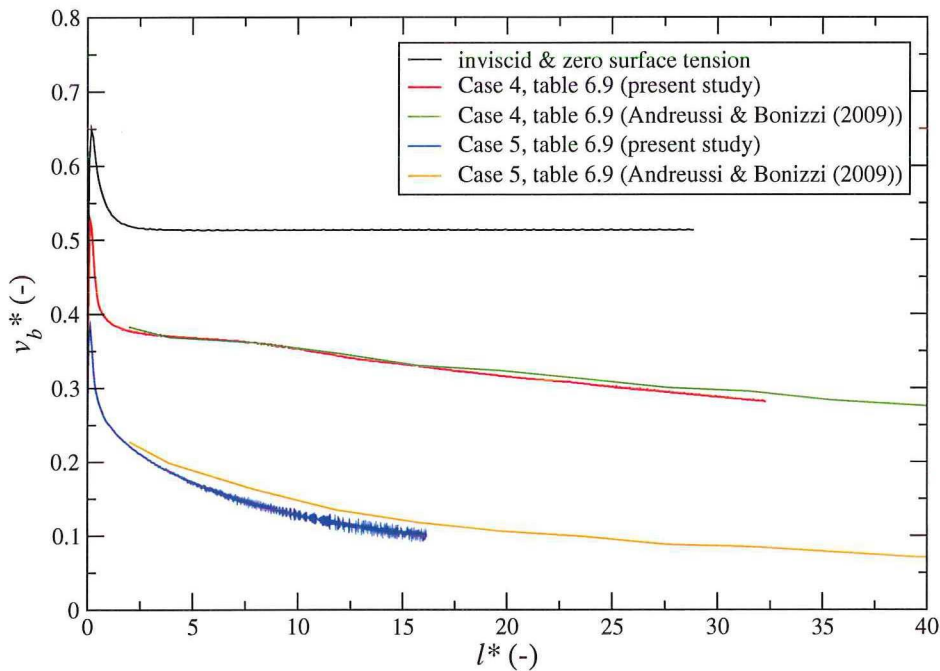


Figure 6.24: Bubble velocity along the length of the pipe for the 3D Benjamin bubble.

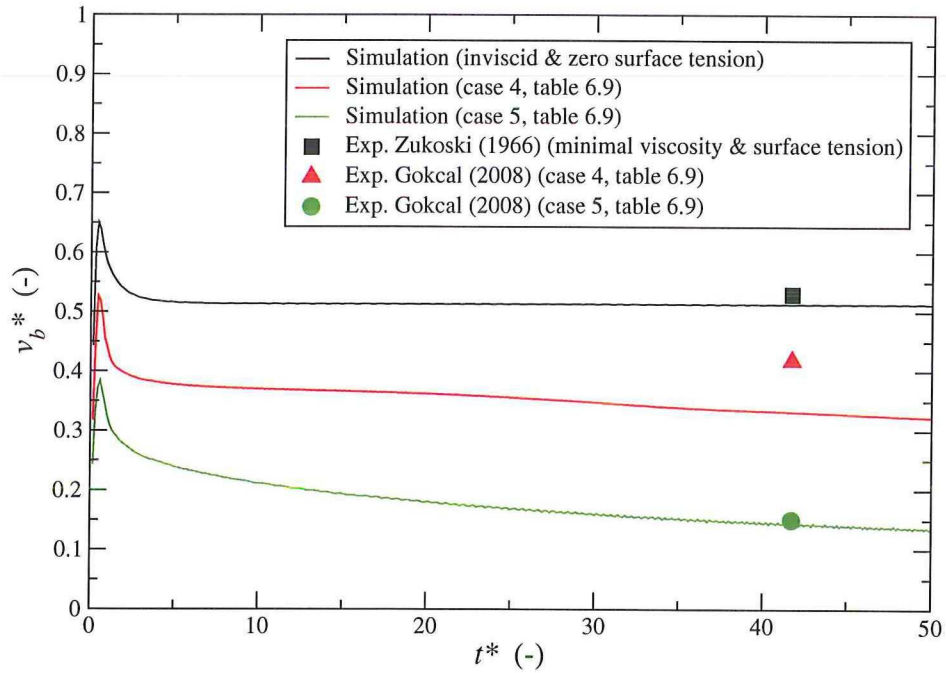


Figure 6.25: Bubble velocity versus dimensionless time for the 3D Benjamin bubble in a pipe.

For the 3D pipe, a similar behaviour of the bubble as in the viscous 2D Benjamin bubble flow is observed. The bubble profile at different time instants for case 5 is shown in figure 6.26. The liquid layer beneath the bubble is again not uniform. As explained earlier the energy losses due to pipe wall friction increases as the liquid layer beneath the bubble (or equivalently the bubble length) increases. Consequently, the bubble velocity drops along the length of the pipe. Again a thin liquid layer remains at the roof of the pipe close to the bubble nose. This was also observed in the simulations of Andreussi and Bonizzi (2009) and of Ben-Mansour et al. (2010).

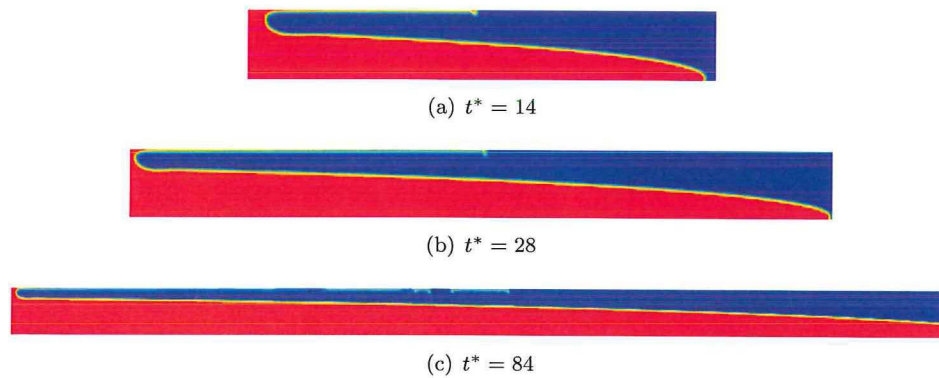


Figure 6.26: Bubble profiles at different time instants for the 3D Benjamin bubble (case 5, table 6.9).

### 6.3 Conclusions

The so-called Benjamin bubble, which is a single infinitely long bubble that moves into a stagnant liquid in a horizontal pipe, was modeled with the VOF model in FLUENT. The two-dimensional flow, which is in fact a channel flow, has an analytical solution for the case of negligible viscosity and negligible surface tension. The dimensionless bubble velocity and liquid height should be 0.5, as derived by Benjamin (1968). The simulation with the finest mesh produced a dimensionless velocity of 0.494, while the corresponding scaled liquid height was 0.495 in agreement with theory and experiments. Three-dimensional simulations, which is in fact pipe flow, were also performed. This 3D problem has an analytical solution for the bubble velocity and liquid height when the effects of viscosity and surface tension can be neglected. The dimensionless bubble velocity and liquid height, which is uniform beneath the bubble, should be 0.542 and 0.563, respectively. The simulation for the finest grid gives a value of 0.516 and 0.55 for the dimensionless bubble velocity and liquid height, respectively. Extrapolation of the results to a zero grid size gives 0.531 and 0.554 for the bubble velocity and liquid height, respectively. These values are within 3% of the theoretical results by Benjamin.

Furthermore, the effects of surface tension and viscosity on both 2D and 3D Benjamin bubble were investigated. For low and moderate surface tension the simulation results are in good agreement with experimental data from the literature. However, for large surface tension the so-called parasite currents are observed. These parasite currents are vortices in the neighbourhood of the interface despite the absence of any external forces. These parasite currents arise as a consequence of local change in curvature, which is inevitable within the CSF model as implemented in FLUENT. Due to these parasite currents the bubble velocity deviates from the experiments and the interface becomes ripply.

Simulations with high viscosities reveal that the bubble velocity decreases with increasing viscosity. Moreover, the bubble velocity decreases along the length of the pipe. The physical explanation for this is that the frictional losses increases as the liquid layer beneath the bubble increases. Furthermore, the liquid layer beneath the bubble is not uniform as it is in the inviscid case. Comparison of the simulation results with experimental data is not straightforward, since most of the authors measured only one velocity at a certain distance and time after the experiment was started. Hence it is difficult to compare the simulation results, in which the bubble velocity decreases continuously along the length of the pipe, with a single velocity measurement at a certain distance and time in the experiments. However, the reduction of bubble velocity along the length of the pipe was also observed in a single experiment by Wilkinson (1982), but no details were given in that study.

---

## Chapter 7

# Simulation results for the Dumitrescu or Taylor bubble

In this chapter the simulation results of the Dumitrescu bubble will be given. First, the results for the 2D axisymmetric Dumitrescu bubble will be given followed by the results for the 3D Dumitrescu bubble. The Dumitrescu bubble in a vertical pipe, with circular cross-section, can be regarded as axisymmetric. Thus it might seem meaningless to do timeconsuming 3D simulations. However, the results to be discussed below show some interesting phenomena that are not captured in the 2D axisymmetric simulations. The results will be compared with the (semi)analytical solution as discussed in chapter 4 and with experimental data. All results will be presented in dimensionless form and the definitions, if not given here, can be found in chapter 4.

### 7.1 2D Axisymmetric Dumitrescu bubble

In this section the simulation results for the 2D axisymmetric Dumitrescu bubble will be given. First the simulation results for the inviscid case with zero surface tension will be presented. After this the results of one simulation with small viscosity and surface tension will be given as well.

#### 7.1.1 Bubble velocity

The bubble velocity is calculated by tracking the position of the nose in time. This is done, as for the Benjamin bubble case, by creating an iso-surface with  $\alpha = 0.5$ , where  $\alpha$  denotes the volume fraction of the gas phase. Then the coordinates of the nose of the bubble were tracked in time to calculate the (average) bubble velocity. The dimensionless bubble velocity is given by

$$v_b^* = \frac{v_b}{\sqrt{gD}}. \quad (7.1)$$

The radius of the curvature at the bubble nose is calculated by the following formula

$$\varrho = \frac{\left(1 + \left(\frac{\partial\eta}{\partial\zeta}\right)^2\right)^{\frac{3}{2}}}{\frac{\partial^2\eta}{\partial\zeta^2}}, \quad (7.2)$$

where  $\eta$  and  $\zeta$  are dimensionless coordinates as defined in chapter 4. The rise velocity of the Dumitrescu bubble for the different grid sizes and schemes is given in figure 7.1. The shape of the bubble is compared with the theoretical shape of Dumitrescu in figure 7.2. The average values for the bubble velocity and the radius of curvature, together with experimental data and analytical solutions, are given in table 7.1 and table 7.2. A graphical representation of the results can be seen in figure 7.3, where the final bubble velocity is plotted versus the dimensionless grid size.

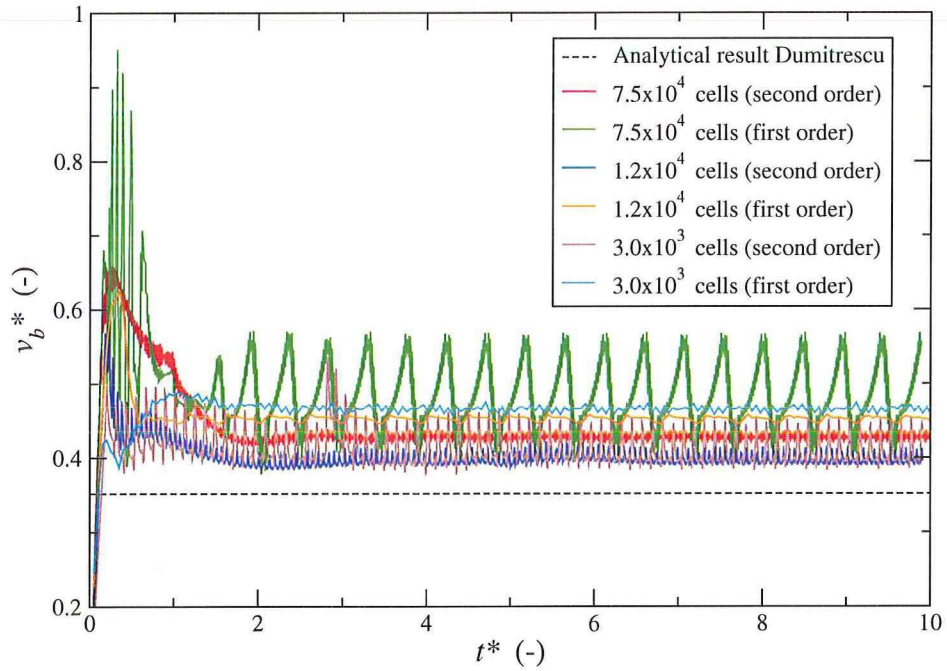


Figure 7.1: Comparison of bubble velocity for the 2D axisymmetric Dumitrescu bubble (inviscid and zero surface tension).

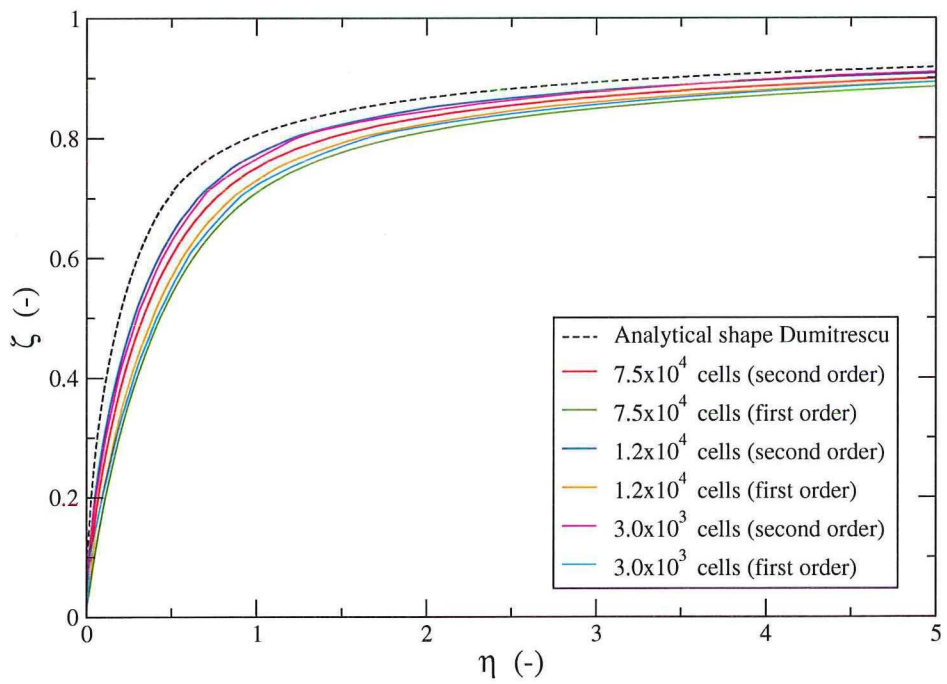
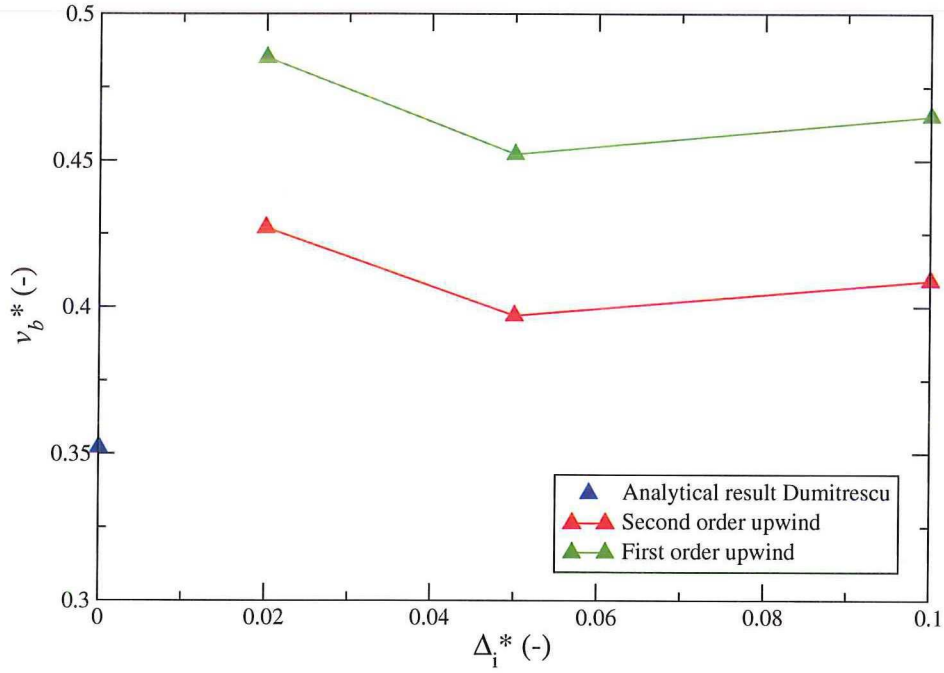


Figure 7.2: Comparison of 2D axisymmetric bubble shape (inviscid and zero surface tension).



**Figure 7.3:** Bubble velocity versus dimensionless grid size for the 2D axisymmetric Dumitrescu bubble (inviscid and zero surface tension).

**Table 7.1:** Bubble velocity and radius of curvature for the 2D axisymmetric Dumitrescu bubble (first order upwind scheme).

$[\Delta_x^*] \times [\Delta_y^*]$	Total number of grid cells	$v_b^*$	$\varrho/D$
[0.1] x [0.1]	3000	0.465	0.17
[0.05] x [0.05]	12000	0.452	0.22
[0.02] x [0.02]	75000	0.485	0.1
Analytical solution Dumitrescu (1943)		0.352	0.75
Approximate solution Davies and Taylor (1950)		0.328	-
Experiment Dumitrescu (1943)		0.346	0.75
Experiment White and Beardmore (1962)		0.345	-
Experiment Zukoski (1966)		0.34	-

**Table 7.2:** Bubble velocity and radius of curvature for the 2D axisymmetric Dumitrescu bubble (second order upwind scheme).

$[\Delta_x^*] \times [\Delta_y^*]$	Total number of grid cells	$v_b^*$	$\varrho/D$
[0.1] x [0.1]	3000	0.409	0.56
[0.05] x [0.05]	12000	0.397	0.63
[0.02] x [0.02]	75000	0.427	0.25

Clearly, the simulation results do not agree with the theoretical result of Dumitrescu (1943) and Davies and Taylor (1950). The difference in bubble velocity at the finest grid for both schemes is more than 20 percent. It is remarkable that the results on the coarser grids relative to the finest grid are in better agreement (10 percent difference) with the theoretical solution, as can be seen in figure 7.3. Note that the agreement between the theoretical result of Dumitrescu and the experimental data is not just coincidence, since Dumitrescu used, as explained in chapter 4, experimental facts to solve the problem. However, in real experiments there will always be a small effect of viscosity and surface tension. A possible reason for the discrepancies between the simulation results and the theoretical solution of Dumitrescu is the existence of multiple solutions to the inviscid problem. To the best of our knowledge, only one paper by Mao and Dukler (1990) reports the existence of multiple solutions to the problem. However multiplicity is also described in papers on vertical channel flows, see Birkhoff and Carter (1957), Garabedian (1957), Collins (1965), Vanden-Broeck (1984a), Vanden-Broeck (1984b), Couët et al. (1986) and Daripa (2000). In the same paper Mao and Dukler gives a criterion for selecting the physically observable (experimental) velocity from the infinite many solutions. The criterion is based on the fact that for any nonzero surface tension, no matter how small, the bubble must have a spherical shape in the immediate vicinity of the nose vertex. Consequently, the gradient of the curvature should be zero at the nose and this was used by Mao and Dukler (1990) as a criterion for obtaining the physically realistic velocity. The additional requirement of zero gradient of the curvature near the nose is only satisfied at one rise velocity. This selected rise velocity turns out to be in excellent agreement with the experiments. This suggests that the surface tension is responsible for obtaining the physical solution. Therefore one simulation was done with a small viscosity and surface tension. The results for this simulation can be found in the next section.

### 7.1.2 Effect of surface tension

To check the effect of a small (but finite) surface tension a simulation with an Eötvös number ( $Eo$ ) of 200 and a Morton number ( $Mo$ ) of  $1.6 \times 10^{-11}$ , corresponding with an experiment of White and Beardmore (1962), was performed. Under these conditions both viscous and surface forces are small. The dimensionless numbers  $Eo$  and  $Mo$  are defined by equation 6.9 and by equation 6.10, respectively. The simulations for these parameters were done on all the three grids with a second order scheme. Results for the bubble velocity are given in figure 7.4 and the resulting bubble shape is given in figure 7.5. The average values of the final bubble velocity and the experimental result of White and Beardmore (1962) are given in table 7.3.

**Table 7.3:** Comparison of the bubble velocity for the 2D axisymmetric Dumitrescu bubble (second order upwind scheme).

$[\Delta_x^*] \times [\Delta_y^*]$	Total number of grid cells	$Eo$	$Mo$	$v_b^*$
$[0.1] \times [0.1]$	3000	200	$1.6 \times 10^{-11}$	0.345
$[0.05] \times [0.05]$	12000	200	$1.6 \times 10^{-11}$	0.359
$[0.02] \times [0.02]$	75000	200	$1.6 \times 10^{-11}$	0.344
Experiment White and Beardmore (1962)		200	$1.6 \times 10^{-11}$	0.345

Although a peculiar behaviour is seen in figure 7.4 for  $3 < t^* < 6$ , the final bubble velocity for all the three grids is in good agreement with the theoretical result of Dumitrescu and the experiment of White and Beardmore (1962). As we would expect, since the bubble velocity and shape are related, the bubble shape for all the grids are also in good agreement with the theoretical shape. The problem now is to decide upon which of the three solutions is most accurate, since all the three are in good agreement with theory and experiment. Since no peculiarity is seen on the finest mesh one can say, with a reasonable confidence, that the solution on the finest mesh is most accurate. The conclusion that can be drawn from this simulation is that the statement by Mao and Dukler (1990), that a small surface tension is required for obtaining the physically observed bubble velocity, seems to be correct.

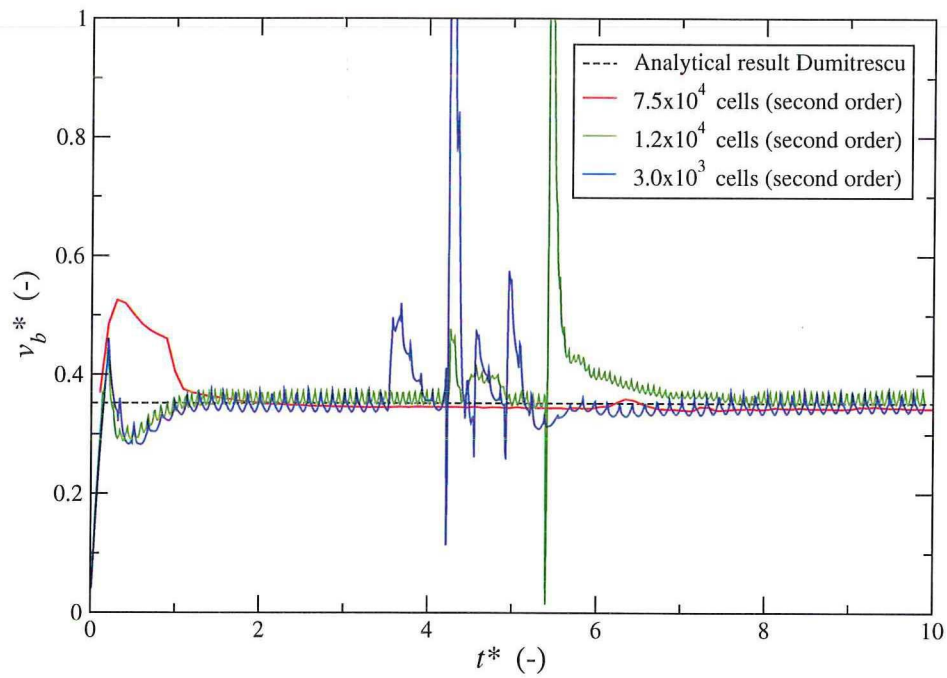


**Figure 7.4:** Comparison of the bubble velocity for the 2D axisymmetric Dumitrescu bubble ( $Eo = 200$ ,  $Mo = 1.6 \times 10^{-11}$ ).

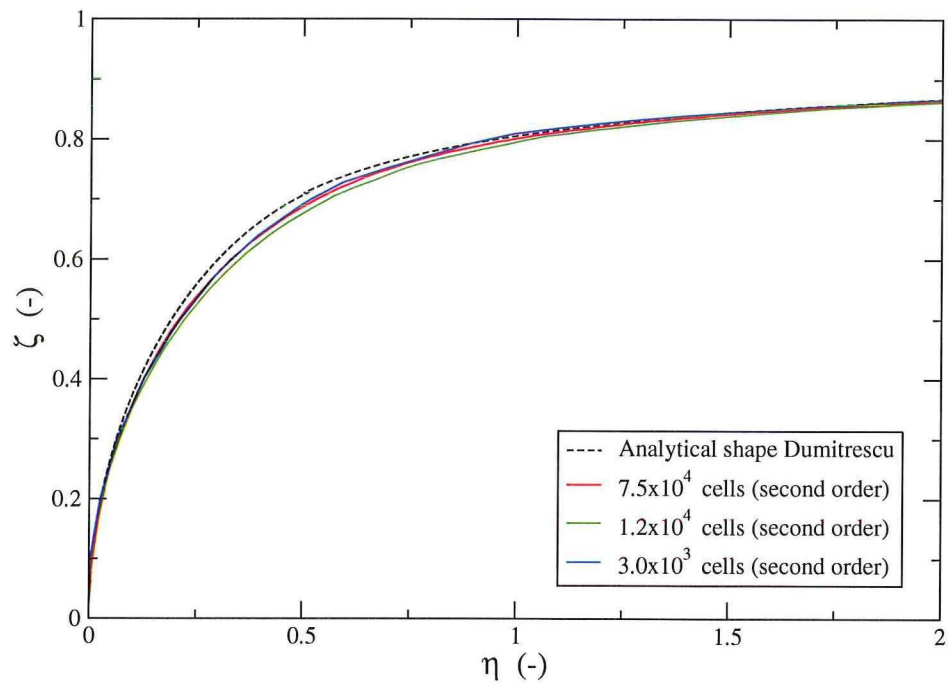


**Figure 7.5:** Comparison of the bubble shape for the 2D axisymmetric Dumitrescu bubble ( $Eo = 200$ ,  $Mo = 1.6 \times 10^{-11}$ ).

## 7.2 3D Dumitrescu bubble

In addition to the 2D axisymmetric simulations a few 3D simulations were done. In this section the simulation results for these 3D simulations will be given. First the results of the inviscid and zero surface tension case will be presented. After this results of one simulation, in which surface tension and viscosity were included, will be given. Simulation results will be compared with theoretical and experimental data.

### 7.2.1 Bubble velocity

In contrast to the 2D axisymmetric simulations, the 3D simulations were started with a pre-defined bubble shape. A User Defined Function (UDF), see Appendix B for an example, was used to initialize the bubble shape. The initial shape was defined by an arbitrarily chosen cosine function with a period of  $2D$ , where  $D$  denotes the pipe diameter. The length of the bubble (amplitude of the cosine function) was randomly chosen, but since the mesh consists of hexahedral cells a certain length was required to obtain a curved bubble nose. However, the initial shape of the bubble is not important: after the simulation is started, the bubble quickly adopts an equilibrium shape of a Dumitrescu bubble. The initial shape of the bubble is shown in figure 7.6(a). The bubble velocity is calculated by first creating a plane at the centre of the pipe, as shown in figure 7.6(b). Subsequently an iso-surface of 0.5 for the volume fraction was created on this plane and the position of the bubble nose was tracked in time to calculate the velocity.

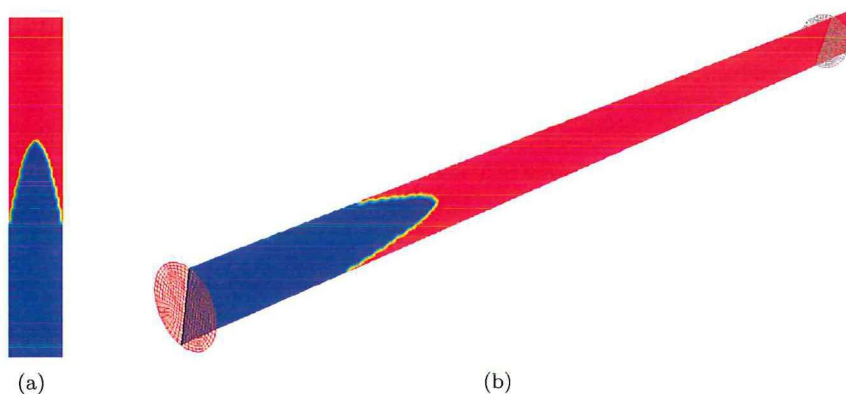


Figure 7.6: (a) Initial bubble shape, (b) Symmetry plane

The grids used for the simulations are similar to the grids for the 3D simulations of the Benjamin bubble, see table 6.6. The diameter and the length of the pipe were, 0.05 m and 3.0 m, respectively. The finest mesh contained 518400 grid cells and the simulation was run until  $t^* = 17.5$ . The computational time for this simulation, with four processors (Dual Core AMD Opteron<sup>TM</sup> Processor 275), was in the order of two weeks.

The dimensionless bubble velocity versus the dimensionless time is plotted in figure 7.7. Clearly, the results of the 3D simulations are different from the 2D axisymmetric simulations. The bubble velocity in the 2D axisymmetric case reaches a constant value after a short time and is independent of the bubble length. However, in the 3D simulations the bubble becomes unstable when the length of the bubble is more than  $6D$ , where  $D$  denotes the diameter of the pipe. Only the results for the finest grid will be analyzed here, but the instability is seen for all the grid sizes when the bubble exceeds a certain length. This length is  $6D$  for the finest mesh. The bubble velocity is initially more or less constant and close to the theoretical velocity of Dumitrescu, but after some time ( $t^* > 6$ ) the bubble becomes unstable and the velocity starts to increase. The instability appears at the tail of the bubble and causes the bubble to become asymmetric. This instability and asymmetry is clearly seen in figure 7.8 for  $t^* > 6$ . The increase in the bubble velocity can readily be understood, since an asymmetric bubble rises faster than a symmetric bubble, see Zukoski (1966) and Mao and Dukler (1990). Of course this instability and asymmetry is not captured in the 2D axisymmetric simulations,

and hence the bubble velocity is not altered for any bubble lengths. The question remains whether the instability is due to a numerical artifact or due to the physics. This instability is also observed in experiments, see Gibson (1913) and Nigmatulin (2001), for very large, but finite bubbles. However, an infinitely large bubble, which is experimentally obtained by emptying a vertical tube, is simulated. In this case the liquid film around the Dumitrescu bubble becomes thinner and thinner as the bubble becomes larger. It is evident that at a certain bubble length, the film becomes such thin that the numerical mesh may become inappropriate and further grid refinement would be required. However, the instabilities are seen on all the three grid sizes approximately after  $t^* = 6$  and for a bubble length of  $6D$ . This suggests that grid refinement has no or minor influence, showing that the phenomena may have a physical nature. This problem should be investigated further to draw a more definite conclusion on the nature of the instabilities. One way of doing this is by refining the grid further, but the computational time will then increase considerably.

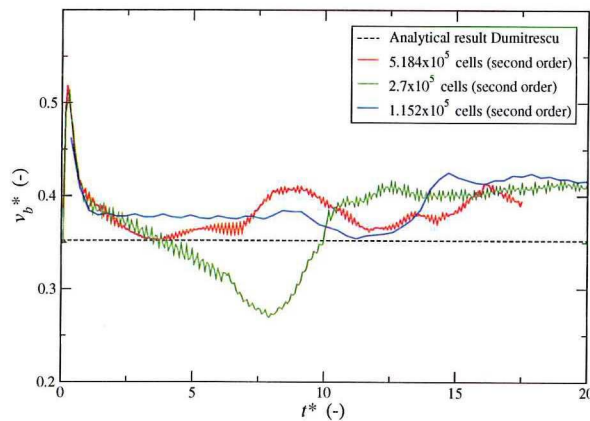


Figure 7.7: Comparison of bubble velocity for the 3D Dumitrescu bubble (inviscid and zero surface tension).

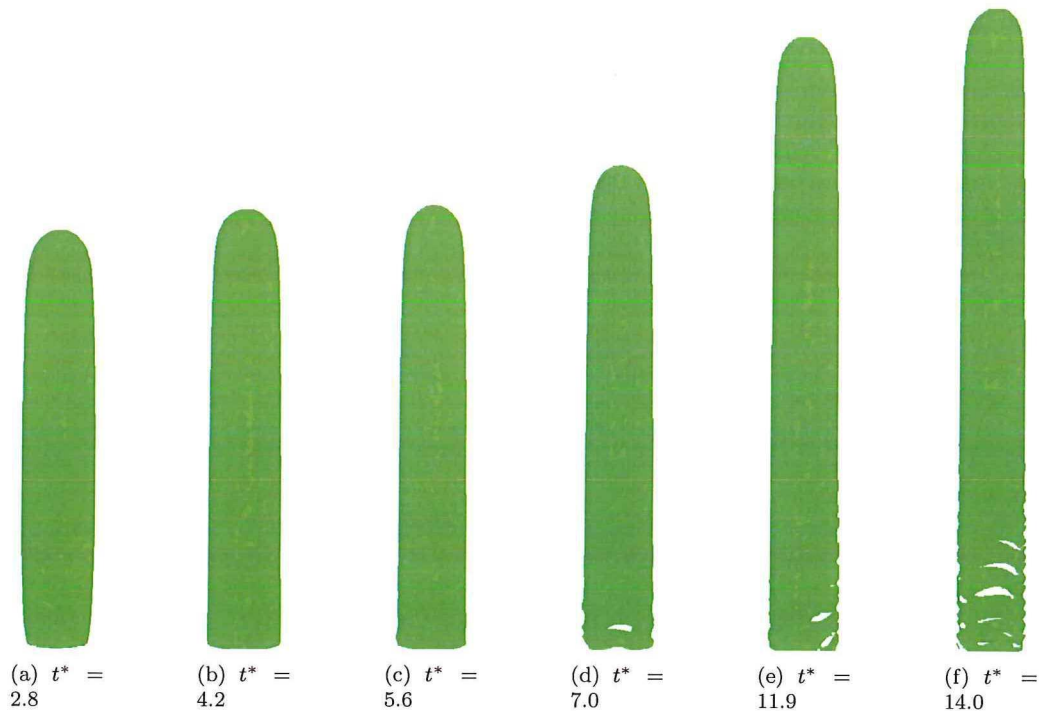


Figure 7.8: 3D bubble surface (iso-surface of 0.5) at different time instants for the finest grid (inviscid and zero surface tension).

### 7.2.2 Effect of viscosity and surface tension

In order to investigate the effect viscosity and surface tension on the bubble velocity a simulation, corresponding with the PIV measurements of Bugg and Saad (2002), was performed. Bugg and Saad (2002) provide detailed information on the velocity field around a Dumitrescu or Taylor bubble. This kind of experimental work is of major importance, due to the high quality and accuracy, for the validation of CFD codes. Similar experiments were done by Polonsky et al. (1999), van Hout et al. (2002), Nogueira et al. (2006a) and Nogueira et al. (2006b). All these authors used PIV to measure the velocity field around a Dumitrescu bubble. Some measurement results by Bugg and Saad (2002) are given in figure 7.9.

The dimensionless bubble velocity  $v_b^*$  versus the dimensionless time  $t^*$  is plotted in figure 7.10. The average final dimensionless bubble velocity is compared with the experiment in table 7.4. Note that Bugg and Saad (2002) used a 0.019 m diameter tube, while the simulation was done with a 0.05 m diameter tube. Hence, the material properties were changed accordingly to keep  $Eo$  and  $Mo$  constant. The Reynolds number based on the bubble velocity is also given in table 7.4. The simulation bubble rise velocity is in good agreement with the experiment. The velocity field around the Dumitrescu bub-

**Table 7.4:** Comparison of the dimensionless bubble velocity for the Dumitrescu bubble.

Experiment/simulation	D (m)	$\rho$ (kg/m <sup>3</sup> )	$\mu$ (Pa·s)	$\sigma$ (N/m)	$Eo$	$Mo$	$v_b^*$	Re
Exp. Bugg and Saad (2002)	0.019	911	0.084	0.0328	100	0.015	0.303	27
Simulation	0.05	911	0.359	0.227	100	0.015	0.292	26

ble will be compared in the upcoming figures. The results of the simulation and the PIV measurements for the axial velocity along the tube axis above the bubble are given in figure 7.11. The axial velocity  $v_z$  is nondimensionalized by the bubble rise velocity  $v_b$ . The simulation results are in good agreement with the PIV measurements. Figure 7.12 compares the axial and radial velocity, at a position  $z/D = -0.111$ . This position corresponds with location *A* in figure 7.9, just above the bubble nose. Again, the simulation results are in good agreement with the PIV measurements. Figure 7.13 compares the axial and radial velocity, at a position  $z/D = 0.504$ . This position corresponds with location *B* in figure 7.9, just below the bubble nose. At this point the film is still developing and has a small radial velocity component. Good agreement between the experimental data and the simulation is seen. Beyond the section *B* in figure 7.9 a fully developed film is formed. The radial component of the velocity in this fully developed film is zero and the axial velocity profile does not change anymore. Figure 7.14 compares the axial velocity profile in the fully developed falling film. No PIV measurements are available close to the interface, due to excessive laser light reflection from the bubble surface. In figure 7.14 also the theoretical result of Brown (1965) is given. Brown modified the potential flow theory of Dumitrescu in the film region assuming laminar flow in the film. By applying a material balance (see Appendix C) Brown obtained the following expression for the velocity distribution in the film

$$v_z = \frac{\rho g}{\mu} \left( \frac{R^2 - r^2}{4} - \frac{(R - \delta)^2}{2} \ln \frac{R}{r} \right). \quad (7.3)$$

Here  $v_z$  is the axial velocity component,  $\rho$  the liquid density,  $g$  the gravity parameter,  $\mu$  the liquid viscosity,  $R$  the tube radius and  $\delta$  the film thickness. Brown also provided a general correlation for the film thickness

$$\delta = \frac{-1 + \sqrt{1 + 2NR}}{N} \quad (7.4)$$

and the bubble velocity

$$v_b = 0.496 \sqrt{gR} \sqrt{1 - \frac{-1 + \sqrt{1 + 2NR}}{NR}} \quad (7.5)$$

where

$$N = \sqrt[3]{14.5 \frac{\rho^2 g}{\mu^2}}. \quad (7.6)$$

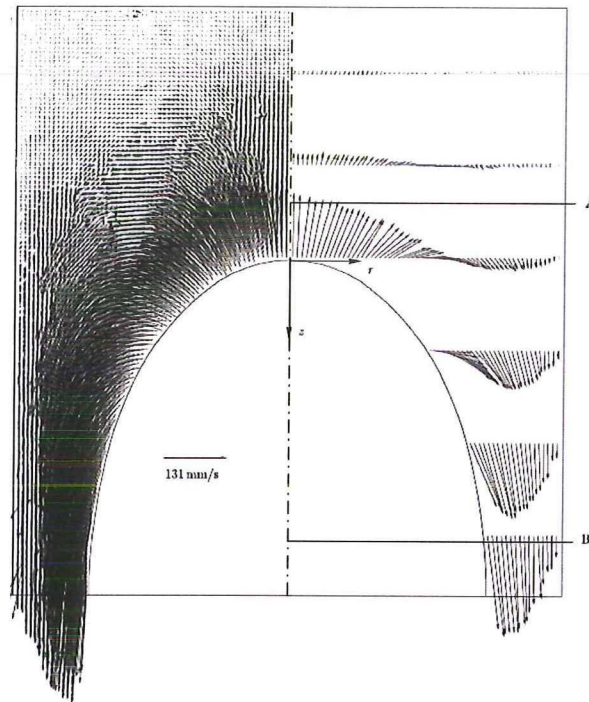


**Figure 7.9:** PIV measurements of the velocity field close to the bubble nose in a 19 mm diameter tube,  $Eo = 100$  and  $Mo = 0.015$  (Bugg and Saad, 2002).

The shape of the bubble at different time instants is given in figure 7.15. It can be seen that the bubble shape does not change in time after it has adopted an equilibrium shape. The initial bubble shape and the shape given by Dumitrescu for the potential flow is also depicted in figure 7.15. The shape of the bubble, close to the nose, is similar to the shape for the potential flow. This is in agreement with the observation of Brown (1965). The analysis of Brown (eqn. 7.4) predicts a dimensionless film thickness ( $\delta/R$ ) of 0.249, while the simulation predicts a dimensionless film thickness of 0.25. Equation 7.5 predicts a dimensionless bubble velocity ( $v_b/\sqrt{gD}$ ) of 0.304, while the simulation predicts 0.292. In conclusion the simulation results are in good agreement with the PIV measurements of Bugg and Saad (2002) and with the theoretical result of Brown (1965).

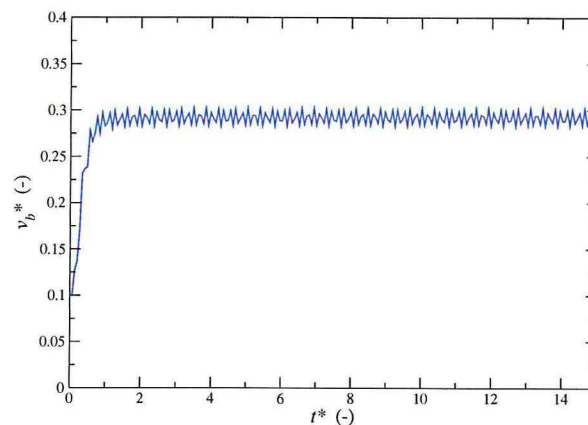


**Figure 7.10:** Dimensionless bubble rise velocity ( $Eo = 100$  and  $Mo = 0.015$ ).

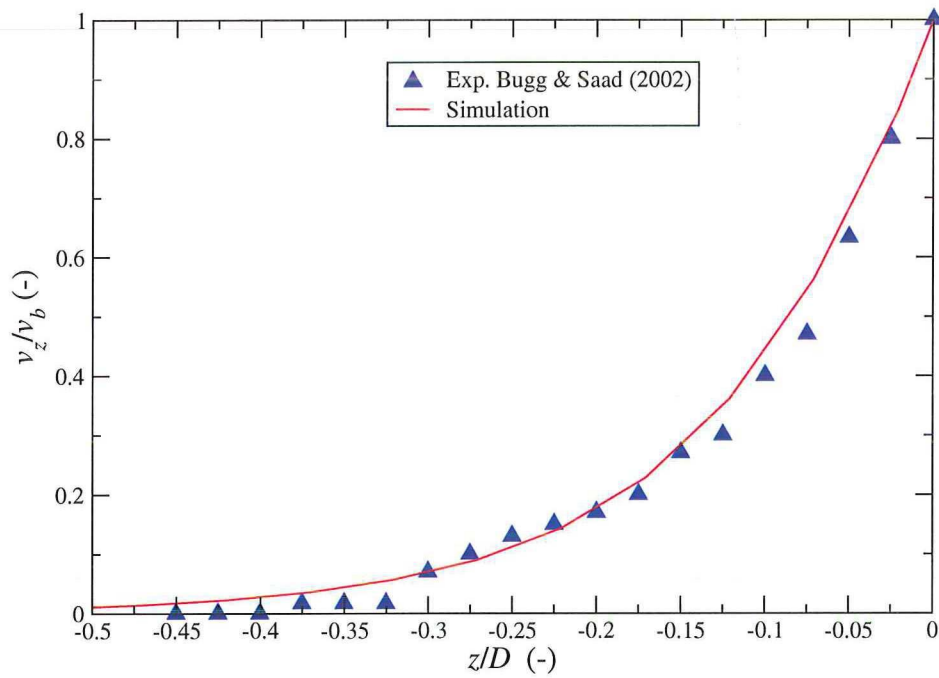


**Figure 7.11:** Comparison of simulation results with PIV measurements for the axial velocity along the tube axis above the Dumitrescu bubble.

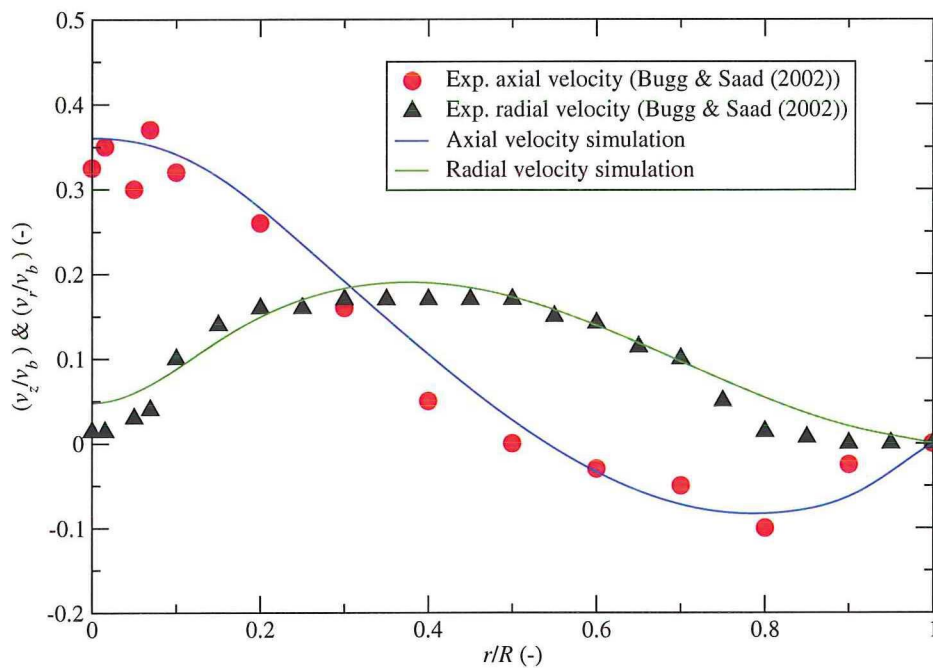


**Figure 7.12:** Comparison of simulation results with PIV measurements for the axial and radial components of velocity at  $z/D = -0.111$  for the Dumitrescu bubble. This location corresponds to section A in figure 7.9.

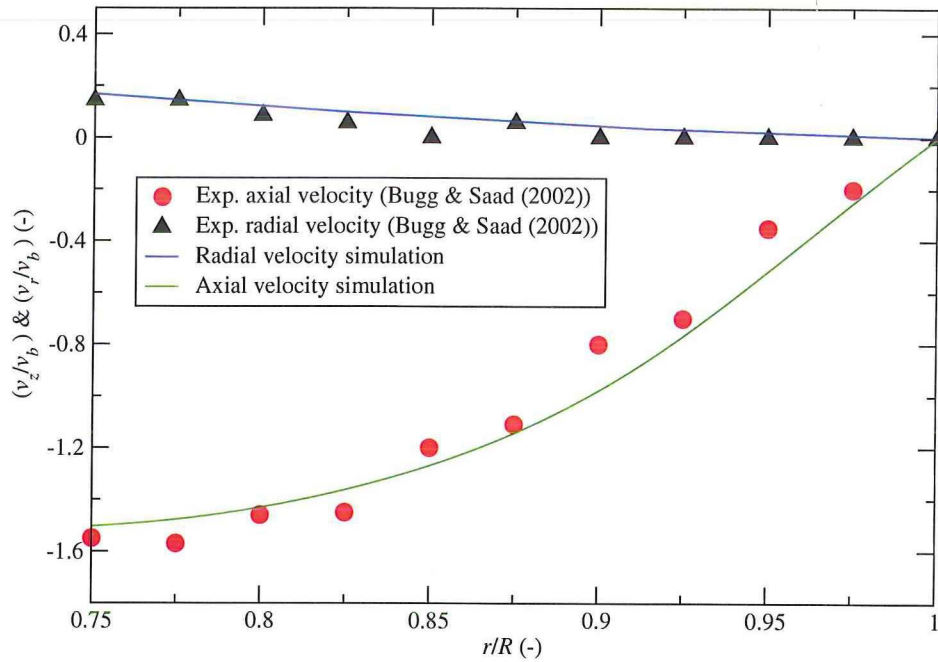


**Figure 7.13:** Comparison of simulation results with PIV measurements for the axial and radial components of velocity at  $z/D = 0.504$  for the Dumitrescu bubble. This location corresponds to section B in figure 7.9.

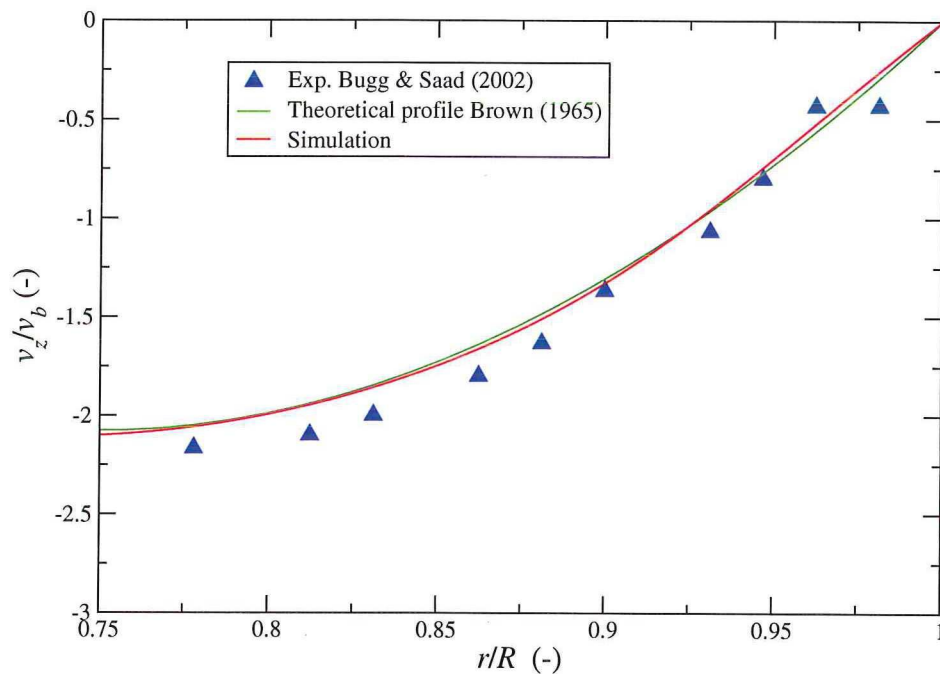


**Figure 7.14:** Comparison of simulation results with PIV measurements and analytical solution of Brown (1965) for the axial component of velocity in the fully developed falling film for the Dumitrescu bubble.

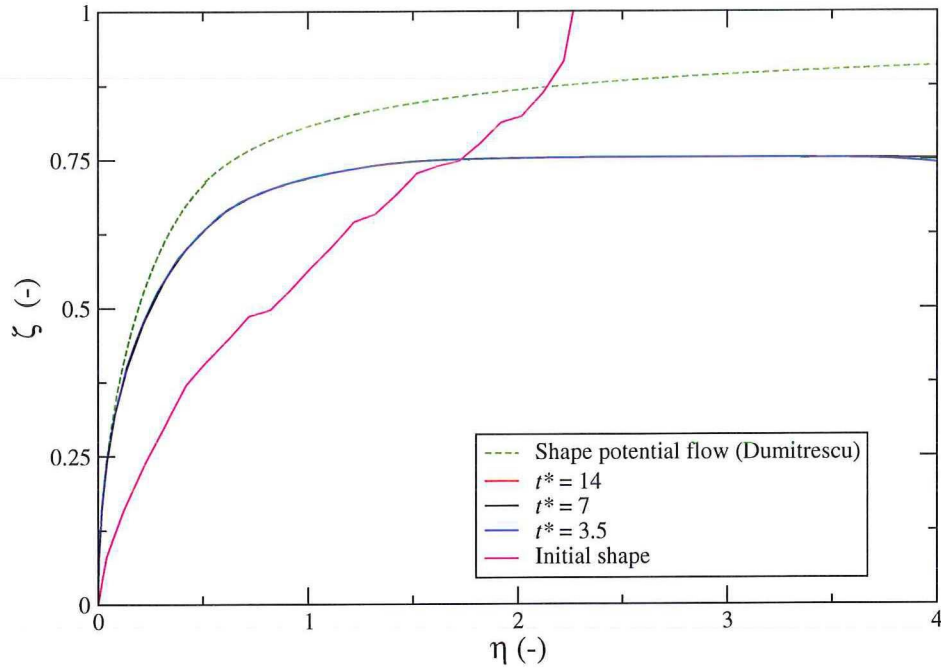


Figure 7.15: Shape of the bubble at different time instants.

### 7.3 Conclusions

A single large bubble, i.e. Dumitrescu or Taylor bubble, which rises in a stagnant liquid in a vertical pipe was modeled in FLUENT with the VOF model. This problem has an analytical solution for the bubble velocity when the viscosity and surface tension are neglected. The theoretical dimensionless bubble velocity ( $v_b/\sqrt{gD}$ ) should be 0.352. The problem can be regarded as axisymmetric, but both 2D axisymmetric and 3D simulations were performed. The bubble velocity of the 2D axisymmetric simulations on three different grid sizes, with zero viscosity and surface tension, does not agree with the theoretical result. The deviation in the bubble velocity is more than 20 percent. The reason for this is most likely due to the existence of multiple solutions to the inviscid problem. Mao and Dukler (1990) showed that multiple solutions exist and claimed that the surface tension is responsible for obtaining the physical relevant solution. Hence, a simulation with a small viscosity and surface tension was performed. The dimensionless bubble velocity for this simulation was 0.344, which is in good agreement with the experimental value of 0.345 and also in very close agreement with the theoretical value of 0.352. Thus the proposition by Mao and Dukler (1990) that the surface tension is possibly responsible for the physically observable solution, seems to be correct.

In addition to the 2D axisymmetric simulations also 3D simulations, with zero viscosity and surface tension, were performed. The 3D simulations show that the bubble becomes unstable when the bubble exceeds a certain length. Instabilities at the tail of the bubble were observed for a bubble length of approximately  $6D$  or larger. Due to this instability the bubble becomes asymmetric and the bubble velocity starts to increase. This shows the importance of 3D simulations, since the instability and asymmetry of the bubble are not captured in the 2D axisymmetric simulations. One extra 3D simulation, with viscosity and surface tension, corresponding with the experimental work of Bugg and Saad (2002) was done. The results of this simulation, axial and radial velocities at several locations, are in good agreement with the PIV measurements of Bugg and Saad (2002).

---

## Chapter 8

# Conclusions and Recommendations

In this chapter the study is concluded and recommendations are given for future research. Furthermore, the intention of this chapter is to clarify the questions (or goals) stated in the introductory chapter.

### 8.1 Conclusions

Two benchmark simulations, namely the Benjamin bubble and the Dumitrescu or Taylor bubble, were performed in order to investigate the reliability of a selected commercial CFD code FLUENT for modeling multiphase flows in pipelines. The Benjamin bubble is a single large bubble that moves into a stagnant liquid in a horizontal pipe. The Taylor bubble is a single large bubble, which rises in a stagnant liquid in a vertical pipe. Both bubbles are important in the modeling of slug flow, which is a common flow regime in pipelines found in the oil and gas industry. The Volume Of Fluid (VOF) multiphase model was used to model the two phases. Both 2D and 3D simulations were performed for several grid sizes in order to assure grid independence. The two benchmark cases have an analytical solution when the effect of viscosity and the effect of surface tension are neglected. In addition to these special conditions, simulations were performed to investigate the effects of viscosity and surface tension on the bubble motion both in horizontal and vertical pipes.

The following conclusions can be drawn for the Benjamin bubble:

- The dimensionless bubble velocity obtained in the simulations for the finest grid size for the 2D Benjamin bubble (inviscid) was  $v_b/\sqrt{gH} = 0.494$ , which is in good agreement with the analytical value of 0.5. The corresponding dimensionless height was  $y/H = 0.495$ , which compares favourably with the analytical value of 0.5.
- The dimensionless bubble velocity obtained in the simulations for the finest grid size for the 3D Benjamin bubble (inviscid) was  $v_b/\sqrt{gD} = 0.516$ , which is in good agreement with the analytical value 0.542. The corresponding dimensionless height was  $y/D = 0.551$ , which is also in good agreement with the analytical value of 0.563. Extrapolation of the FLUENT results to a zero grid size gives a value of 0.531 and 0.554 for the dimensionless bubble velocity and the dimensionless liquid height, respectively.
- Simulations were performed to investigate the effect of the surface tension on the Benjamin bubble. The results were compared with available experimental data. The simulations show that the VOF model accurately models flow with low or moderate surface tension, but parasite currents appear in flows dominated by the surface tension. These parasite currents are vortices in the neighbourhood of the interface, which tend to destroy the interface. These parasite currents originate from the calculation of the interface curvature in the Continuum Surface Force (CSF) model, which is implemented in FLUENT to model the surface tension.
- Simulations to account for the effect of viscosity on the Benjamin bubble reveal that the bubble velocity decreases as the viscosity increases, as one would expect. However, the simulations show that the bubble velocity also decreases with increasing time when the bubble moves along the length of the pipe. The reason for this is that the frictional losses increase when the length of

the liquid layer beneath the bubble (or equivalently the bubble length) increases. Extrapolation of the results show that the bubble comes to a stand-still after long time (shorter with increasing viscosity).

- In contrast to the expectation, the first-order upwind scheme in FLUENT gives more accurate solutions than the QUICK scheme.

The Taylor bubble has an axisymmetric nature, but both 2D axisymmetric and 3D simulations were performed. The following conclusions can be drawn for the Dumitrescu or Taylor bubble:

- The simulation results for the bubble velocity for the inviscid, zero surface tension and 2D axisymmetric flow are not in agreement with the analytical solution. The analytical dimensionless bubble velocity is  $v_b/\sqrt{gD} = 0.352$ , but the simulations give a value of approximately 0.4 for the coarse mesh and 0.43 for the finest mesh. The difference is more than 20 percent and the reason for this is most likely the existence of multiple solutions for the inviscid equations. Existence of multiple solutions is also reported in the literature by Mao and Dukler (1990), in which the authors claim surface tension to be responsible for obtaining the physically relevant solution.
- Simulations including a small surface tension in the 2D axisymmetric flow gave a dimensionless bubble velocity of  $v_b/\sqrt{gD} = 0.344$ , which is in good agreement with the analytical value of 0.352. This result supports the claim that the surface tension is most likely responsible for obtaining the physically relevant solution.
- In addition to the 2D axisymmetric simulations 3D simulations were performed. These 3D simulations show that the bubble becomes unstable at a certain bubble length. In the present simulations this critical length was about  $6D$ , where  $D$  is the diameter of the pipe. Furthermore the instability cause the bubble to become asymmetric and as a consequence the bubble velocity increases. Obviously, the instability and the asymmetry are not seen in the 2D axisymmetric simulations.
- The simulation results for a case with viscosity and surface tension are in good agreement with the highly detailed experimental data of Bugg and Saad (2002).

We can conclude that the selected CFD code FLUENT can accurately model the Benjamin bubble and the Taylor bubble with the VOF model. Problems may arise when the flow is dominated by the surface tension. It is not the inability of the VOF model to model such flows, but the existence of parasite currents when the flow is dominated by surface forces. The origin of these parasite currents lies in the determination of the interfacial curvature in the Continuum Surface Force (CSF) model implemented in FLUENT to include the surface tension.

More simulations are required to be able to verify the work of De Schepper et al. (2008) who carried out CFD simulations for various fully developed flow regimes in a horizontal pipe. They claimed that the current commercial CFD codes are able to predict the transition between the different multiphase flow regimes in a horizontal pipe. No transitions between flow regimes were modeled in our study, but FLUENT can at least accurately model the simplified form of slug flow, namely the Benjamin bubble or the Taylor bubble.

## 8.2 Recommendations

The following recommendations for future research emanate from the present study:

- Investigate the effect of high viscosity on the Benjamin bubble experimentally with well defined conditions. Since the bubble velocity decreases along the length of the pipe it is important to measure the velocity profile along the pipe, rather than measuring the velocity at a single position. This would make the comparison with CFD simulations easier.
- Investigate the nature of the instability observed in the 3D simulations for the Taylor bubble. It is good to know whether the instabilities are due to a numerical artifact or due to the physics.
- Investigate the effect of high viscosity on the Taylor bubble. The bubble velocity decreases along the pipe for the Benjamin bubble. It should be investigated whether this is also the case for the Taylor bubble.
- Investigate the so-called plane Taylor bubble. This is a Taylor bubble that rises between two vertical planes, rather than in a pipe. It is shown in the literature that this problem has multiple theoretical solutions if the inviscid equations are considered. This would shine more light on the multiplicity of solutions in the "normal" Taylor bubble problem.
- Carry out CFD simulations for the transition between the different flow regimes and compare the results with the one-dimensional models or with experimental data. This will allow to give a more definite judgment on the claim of De Schepper et al. (2008). In addition carry out CFD simulations for the various fully developed flow regimes in horizontal and vertical pipe flow, which should include: stratified flow, slug flow, annular flow, and bubbly flow.
- Carry out benchmarking simulations for the Benjamin bubble and for the Dumitrescu/Taylor bubble with other commonly used commercial CFD codes, such as CFX, STAR-CD and Open-FOAM.



---

# Bibliography

- I. N. Alves, O. Shoham, and Y. Taitel. Drift velocity of elongated bubbles in inclined pipes. *Chem. Eng. Sci.*, 48(17):3063–3070, 1993.
- P. Andreussi and M. Bonizzi. Motion of elongated gas bubbles over a horizontal liquid layer. In *14th International Conference on Multiphase Production Technology*, pages 309–318. BHR Group, 2009.
- ANSYS FLUENT. Best practices for the vof model. On-line training, 2006. URL [www.fluentusers.com](http://www.fluentusers.com).
- ANSYS FLUENT. Volume of fluid model: Advanced multiphase modeling course. On-line training, 2007. URL [www.fluentusers.com](http://www.fluentusers.com).
- W.D. Baines. The motion of constant volume air cavities in long horizontal tubes. *J. Fluid Mech.*, 161:313–327, 1985.
- O. Baker. Design of pipelines for the simultaneous flow of oil and gas. *Oil and Gas Journal*, 53: 185–195, 1954.
- D. Barnea. A unified model for predicting flow-pattern transitions for the whole range of pipe inclinations. *Int. J. Multiphase Flow*, 13:1–12, 1987.
- G. Barr. The air bubble viscometer. *Phil. Mag. Ser. 7*, 2:395–405, 1926.
- G.K. Batchelor. *An introduction to fluid dynamics*. Cambridge University Press, 1967.
- R. Ben-Mansour, A. K. Sharma, B. C. Jeyachandra, B. Gokcal, A. Al-Sarkhi, and C. Sarica. Effect of pipe diameter and high oil viscosity on drift velocity for horizontal pipes. In *7th North American Conference on Multiphase Technology*, pages 237–248. BHR Group, June 2010.
- K. H. Bendiksen. An experimental investigation of the motion of long bubbles in inclined tubes. *Int. J. Multiphase flow*, 10:467–283, 1984.
- K. H. Bendiksen. On the motion of long bubbles in vertical tubes. *Int. J. Multiphase flow*, 11:797–812, 1985.
- T.B. Benjamin. Gravity currents and related phenomena. *J. Fluid Mech.*, 31:209–248, 1968.
- R.B. Bird, W.E. Stewart, and E.N. Lightfoot. *Transport Phenomena*. John Wiley and Sons, Inc., 2nd edition, 1960.
- G. Birkhoff and D. Carter. Rising plane bubbles. *J. Math. Mech.*, 6:769–779, 1957.
- J. U. Brackbill, D. B. Kothe, and C. Zemach. A continuum method for modeling surface tension. *J. Comp. Phys.*, 100:335–354, 1992.
- F. P. Bretherton. The motion of long bubbles in tubes. *J. Fluid. Mech.*, 10:166–188, 1961.
- R. A. S. Brown. The mechanics of large gas bubbles in tubes 1. Bubble velocities in stagnant liquids. *Canadian J. Chem. Eng.*, 43:217–223, 1965.
- R. A. S. Brown and G. W. Govier. The mechanics of large gas bubbles in tubes 2. The prediction of voidage in vertical gas-liquid flow. *Canadian J. Chem. Eng.*, 43:224–230, 1965.

- E. Buckingham. On physically similar systems: illustrations of the use of dimensional equations. *Phys. Rev.*, 4:345–376, 1914.
- J. D. Bugg. A numerical model of Taylor bubbles rising through stagnant liquids in vertical tubes. *Int. J. Multiphase Flow*, (2), 1998.
- J. D. Bugg and G. A. Saad. The velocity field around a Taylor bubble rising in a stagnant viscous fluid: numerical and experimental results. *Int. J. Multiphase Flow*, 28:791–803, 2002.
- C. Clanet, P. Héraud, and G. Searby. On the motion of bubbles in vertical tubes of arbitrary cross-sections: some complements to the Dumitrescu-Taylor problem. *J. Fluid. Mech.*, 519:359–376, 2004.
- R. Collins. A simple model of the plane gas bubble in a finite liquid. *J. Fluid. Mech.*, 22:763–771, 1965.
- R. Collins, F.F. De Moraes, J.F. Davidson, and D. Harrison. The motion of a large bubble rising through liquid flowing in a tube. *J. Fluid. Mech.*, 89:497–514, 1978.
- B. Couët, G.S. Strumolo, and A.E. Dukler. Modeling two-dimensional large bubbles in a rectangular channel of finite width. *Phys. Fluids*, 29:2367–2372, 1986.
- P. Daripa. A computational study of rising plane Taylor bubbles. *J. Comp. Phys.*, 157:120–142, 2000.
- R.M. Davies and Sir G. Taylor. The mechanics of large bubbles rising through extended liquids and through liquids in tubes. *Proc. Roy. Soc.*, 200:375–390, 1950.
- S.C.K. De Schepper, G.J. Heynderickx, and G.B. Marin. CFD modeling of all gas-liquid and vapor-liquid flow regimes predicted by the Baker chart. *Chem. Eng. J.*, 138:349–357, 2008.
- J.M.M DeJesus. *An experimental and numerical investigation of two-phase slug flow in a vertical tube*. PhD thesis, Graduate Department of Chemical Engineering and Applied Chemistry, University of Toronto, 1997.
- D.T. Dumitrescu. Strömung an einer luftblase im senkrechten rohr. *Z. angew. Math. Mech.*, 23:139–149, 1943.
- FLUENT. *FLUENT 6.3 User's Guide*. FLUENT Inc., Lebanon, 2006.
- P.R. Garabedian. On steady-state bubbles generated by Taylor instability. *Proceedings of the Royal Society of London. Series A, Math. Phys. Sci.*, 241:423–431, 1957.
- G.C. Gardner and I.G. Crow. The motion of large bubbles in horizontal channels. *J. Fluid Mech.*, 43:247–255, 1970.
- A.H. Gibson. On the motion of long air bubbles in a vertical tube. *Phil. Mag. Ser. 6*, 26:952–965, 1913.
- B. Gokcal. *An experimental and theoretical investigation of slug flow for high oil viscosity in horizontal pipes*. PhD thesis, The Graduate School, The University of Tulsa, 2008.
- H. L. Goldsmith and S. G. Mason. The movement of single large bubbles in closed vertical tubes. *J. Fluid. Mech.*, 14:42–58, 1962.
- W.H. Hager. Cavity outflow from a nearly horizontal pipe. *Int. J. Multiphase Flow*, 25:349–364, 1999.
- T. Z. Harmathy. Velocity of large drops and bubbles in media of infinite or restricted extent. *A.I.Ch.E*, 6(2):281–288, 1960.
- S. Hattori. On the motion of a cylindrical bubble in a tube and its application to the measurement of the surface tension of a liquid. *Rept. Aeronaut. Res. Inst. Tokyo Imp. Univ.*, No. 115, 1935.
- C.W. Hirt and B.D. Nichols. Volume of Fluid (VOF) method for the dynamics of free boundaries. *J. Comput. Phys.*, 39:201–225, 1981.

- W.P. Jepson and R.E. Taylor. Slug flow and its transitions in large-diameter horizontal pipes. *Int. J. Multiphase flow*, 19:411–420, 1993.
- O. Kvernfold, V. Vindoy, T. Sontvedt, A. Saasen, and S. Selmer-Olsen. Velocity distribution in horizontal slug flow. *Int. J. Multiphase Flow*, 10:441–457, 1984.
- B. Lafaurie, C. Nardone, R. Scardovelli, S. Zaleski, and G. Zanetti. Modelling merging and fragmentation in multiphase flows with SURFER. *J. Comp. Phys.*, 113:134–147, 1994.
- A. D. K. Laird and D. Chisholm. Pressure and forces along cylindrical bubbles in a vertical tube. *Ind. Eng. Chem.*, 48(2):1361–1364, 1956.
- H. Lamb. *Hydrodynamics*. Cambridge University Press, 6th edition, 1932.
- L. D. Landau and E. M. Lifshitz. *Fluid mechanics*. Butterworth Heinemann, 2nd edition, 1987.
- X. Lu and A. Prosperetti. A numerical study of Taylor bubbles. *Ind. Eng. Chem. Res.*, 48:242–252, 2009.
- T.K. Mandal, G. Das, and P.K. Das. Motion of Taylor bubbles and Taylor Drops in liquid-liquid systems. *Ind. Eng. Chem. Res.*, 47:7048–7057, 2008.
- Z. Mao and A. E. Dukler. The motion of Taylor bubbles in vertical tubes. 1. A numerical simulation for the shape and rise velocity of Taylor bubbles in stagnant and flowing liquid. *J. Comp. Phys.*, 91:132–160, 1990.
- Z. Mao and A. E. Dukler. The motion of Taylor bubbles in vertical tubes. 2. Experimental data and simulations for laminar and turbulent flow. *Chem. Eng. Sci.*, 46(8):2055–2064, 1991.
- E. E. Markovich. Effect of surface tension on the free outflow of a wetting fluid from a horizontal tube. *Fluid Dynamics*, 23(2):230–237, 1988.
- D. I. Meiron. On the stability of gas bubbles rising in an inviscid fluid. *J. Fluid Mech.*, 198:101–114, 1989.
- J. S. Montes. Transition to a free-surface flow at end of a horizontal conduit. *J. Hyd. Research*, 35: 225–241, 1996.
- H. V. Nickens and D. W. Yannitell. The effects of surface tension and viscosity on the rise velocity of a large gas bubble in a closed, vertical liquid filled tube. *Int. J. Multiphase flow*, (1), 1987.
- D.J. Nicklin, J.O. Wilkes, and J.F. Davidson. Two-phase flow in vertical tubes. *Trans. Inst. Chem. Eng.*, 40:61–68, 1962.
- T. R. Nigmatulin. Surface of a Taylor bubble in vertical cylindrical flows. *Doklady Physics*, 46:803–805, 2001.
- S. Nogueira, M. L. Riethmuler, J. B. L. M. Campos, and A. M. F. R. Pinto. Flow in the nose region and annular film around a Taylor bubble rising through vertical columns of stagnant and flowing Newtonian liquids. *Chem. Eng. Sci.*, 61:845–857, 2006a.
- S. Nogueira, M. L. Riethmuler, J. B. L. M. Campos, and A. M. F. R. Pinto. Flow patterns in the wake of a Taylor bubble rising through vertical columns of stagnant and flowing Newtonian liquids: An experimental study. *Chem. Eng. Sci.*, 61:7199–7212, 2006b.
- S. Polonsky, L. Shemer, and D. Barnea. The reation between the Taylor bubble motion and the velocity filed ahead of it. *Int. J. Multiphase flow*, 25:957–975, 1999.
- R. Scardovelli and S. Zaleski. Direct numerical simulation of free-surface and interfacial flow. *Ann. Rev. Fluid. Mech.*, 31:567–603, 1999.
- C. E. Shosho and M. E. Ryan. An experimental study of the motion of long bubbles in inclined tubes. *Chem. Eng. Sci.*, 56:2191–2204, 2001.

- G. G. Stokes. On the theory of oscillatory waves. *Transactions of the Cambridge Philosophical Society*, 1:197–229, 1847.
- T. Taha. CFD modeling of slug flow in vertical tubes. *Chem. Eng. Sci.*, 61:676–687, 2006.
- Y. Taitel and D. Barnea. Modelling flow pattern transitions for steady upward gas-liquid flow in vertical tubes. *AIChE Journal*, 26:345–354, 1980.
- Y. Taitel and A. E. Dukler. A model for predicting flow regime transitions in horizontal and near horizontal gas-liquid flow. *AIChE Journal*, 22:47–55, 1976.
- A. Tomiyama, A. Sou, and T. Sakaguchi. Numerical analysis of bubble motion with the VOF method. *Nuclear Engineering and Design*, 141:69–82, 1993.
- A. Tomiyama, A. Sou, and T. Sakaguchi. Numerical simulation of a Taylor bubble in a stagnant liquid inside a vertical pipe. *Trans. Jap. Soc. Mech. Eng.*, 39(3):517–524, 1996.
- O. Ubbink. *Numerical prediction of two fluid systems with sharp interfaces*. PhD thesis, Imperial college of Science, Technology and Medicine, 1997.
- R. van Hout, A. Gulitski, D. Barnea, and L. Shemer. Experimental investigation of the velocity field induced by a Taylor bubble rising in stagnant water. *Int. J. Multiphase flow*, 28:579–596, 2002.
- J.M. Vanden-Broeck. Bubbles rising in a tube and jets falling from a nozzle. *Phys. Fluids*, 27:1090–1093, 1984a.
- J.M. Vanden-Broeck. Rising bubbles in a two-dimensional tube with surface tension. *Phys. Fluids*, 27:2604–2607, 1984b.
- H.K. Versteeg and W. Malalasekera. *An introduction to computational fluid dynamics: The Finite Volume Method*. Pearson Education, 2nd edition, 2007.
- F. Viana, R. Pardo, R. Yanez, J. L. Trallero, and D. D. Joseph. Universal correlation for the rise velocity of long gas bubbles in round pipes. *J. Fluid. Mech.*, 494:379–398, 2003.
- T. von Kármán. The engineer grapples with nonlinear problems. *Am. Math. Soc.*, 46:615–683, 1940.
- M. E. Weber, A. Alarie, and M. E. Ryan. Velocities of extended bubbles in inclined tubes. *Chem. Eng. Sci.*, 41(9):2235–2240, 1986.
- E.T. White and R.H. Beardmore. The velocity of single cylindrical air bubbles through liquids contained in vertical tubes. *Chem. Eng. Sci.*, 17:351–361, 1962.
- D.L. Wilkinson. Motion of air cavities in long horizontal ducts. *J. Fluid Mech.*, 118:109–122, 1982.
- D.L. Youngs. Time-dependent multi-material flow with large fluid distortion. In K.W. Morton and M.J. Baines, editors, *Numerical methods for fluid dynamics*, The Institute of Mathematics and its Applications conference series, pages 273–285. London Academic Press, march 1982.
- E.E. Zukoski. Influence of viscosity, surface tension, and inclination angle on motion of long bubbles in closed tubes. *J. Fluid Mech.*, 25:821–837, 1966.

## Appendix A

# Dimensional analysis for rise of a Dumitrescu or Taylor bubble

Dimensional analysis is a very powerful tool in physics that can be used to reduce the number of variables required to describe a problem. Moreover, dimensional analysis is used to simplify and understand a complex problem without solving the problem in advance. In general the bubble rise velocity  $w$  may depend on the following quantities (White and Beardmore, 1962)

$$w(\Delta\rho, \rho, \mu, \mu_g, \sigma, g, R, L_b). \quad (\text{A.1})$$

Here  $\rho$  is the density of the fluid in which the bubble rises,  $\Delta\rho$  the density difference between the phases,  $\mu$  the viscosity of the liquid phase,  $\mu_g$  the viscosity of the gas bubble,  $\sigma$  the surface tension,  $g$  the gravity parameter,  $R$  the pipe radius and  $L$  the length of the bubble. The problem has nine variables and three fundamental dimensions. By applying the  $\pi$ -theorem of Buckingham (Buckingham, 1914) six (9-3) nondimensional parameters are obtained. Equation A.1 can also be written as

$$w = [\rho]^\alpha [\Delta\rho]^\beta [\mu]^\gamma [\mu_g]^\zeta [\sigma]^\omega [g]^\eta [R]^\delta [L_b]^\pi. \quad (\text{A.2})$$

The units of all the variables are

$$\left[\frac{m}{s}\right] = \left[\frac{kg}{m^3}\right]^\alpha \left[\frac{kg}{m^3}\right]^\beta \left[\frac{kg}{ms}\right]^\gamma \left[\frac{kg}{ms}\right]^\zeta \left[\frac{kg}{s^2}\right]^\omega \left[\frac{m}{s^2}\right]^\eta [m]^\delta [m]^\pi. \quad (\text{A.3})$$

Balancing the units in equation A.3 gives

$$m : 1 = -3\alpha - 3\beta - \gamma - \zeta + \eta + \delta + \pi, \quad (\text{A.4a})$$

$$s : -1 = -\gamma - \zeta - 2\omega - 2\eta, \quad (\text{A.4b})$$

$$kg : 0 = \alpha + \beta + \gamma + \zeta + \omega. \quad (\text{A.4c})$$

Now three independent variables should be chosen to express the other variables in terms of the chosen variables. It is important to choose the right variables in order to obtain physically meaningful dimensionless numbers. The chosen independent variables were  $\Delta\rho$ ,  $g$  and  $R$ . Therefore, equation A.4b and A.4c gives

$$\eta = \frac{1}{2} - \frac{1}{2}\gamma - \frac{1}{2}\zeta - \omega, \quad (\text{A.5a})$$

$$\alpha = -\beta - \gamma - \zeta - \omega. \quad (\text{A.5b})$$

Substituting equation A.5a and A.5b in equation A.4a gives

$$\delta = \frac{1}{2} - \frac{3}{2}\gamma - \frac{3}{2}\zeta - 2\omega - \pi. \quad (\text{A.5c})$$

Inserting these three variables into equation A.2 results

$$w = [\Delta\rho]^{-\beta-\gamma-\zeta-\omega} [\rho]^\beta [\mu_g]^\gamma [\mu]^\zeta [\sigma]^\omega [g]^{\frac{1}{2}-\frac{1}{2}\gamma-\frac{1}{2}\zeta-\omega} [R]^{\frac{1}{2}-\frac{3}{2}\gamma-\frac{3}{2}\zeta-2\omega-\pi} [L_b]^\pi. \quad (\text{A.6})$$

By collecting similar terms the following six dimensionless numbers are obtained

$$\Pi_1 = \frac{\rho}{\Delta\rho} \quad (\text{A.7})$$

$$\Pi_2 = \frac{\mu_g}{\Delta\rho R \sqrt{gR}} \quad (\text{A.8})$$

$$\Pi_3 = \frac{\mu}{\Delta\rho R \sqrt{gR}} \quad (\text{A.9})$$

$$\Pi_4 = \frac{L_b}{R} \quad (\text{A.10})$$

$$\Pi_5 = \frac{\sigma}{\Delta\rho g R^2} = \frac{1}{\text{Eo}} \quad (\text{A.11})$$

$$\Pi_6 = \frac{w}{\sqrt{gR}} = \text{Fr} \quad (\text{A.12})$$

It is possible to construct different dimensionless groups by combining two or more dimensionless groups. For example,

$$\Pi_7 = \frac{\Pi_2}{\Pi_3} = \frac{\mu_g}{\mu} \quad (\text{A.13})$$

$$\Pi_8 = \frac{\Pi_3^4}{\Pi_4^3 \Pi_1^2} = \frac{\Delta\rho \mu^4 g}{\rho^2 \sigma^3} = \text{Mo} \quad (\text{A.14})$$

and

$$\Pi_9 = \frac{\Pi_1 \Pi_6}{\Pi_3} = \frac{\rho w R}{\mu} = \text{Re} \quad (\text{A.15})$$

The Eötvös number (Eo) and the Froude number (Fr) represent the ratio of surface forces over gravity forces and the ratio of inertial forces over gravity forces, respectively. While, the Morton number (Mo) is defined as the ratio of viscous forces over surface forces and the Reynolds number (Re) is defined as the ratio of inertia forces over viscous forces. In the case of gas bubbles rising through a liquid, the density and the viscosity of the gas are much smaller than the values for the liquid. Hence,  $\Delta\rho/\rho$  is close to unity and the viscosity ratio  $\mu_g/\mu$  is of minor importance. Furthermore, it is shown that for cylindrical bubbles the rise velocity is practically independent of the length of the bubble (White and Beardmore, 1962). In this case dimensional analysis will lead to three groups, namely the Eo, Fr and the Mo group. In the special case of inviscid flow and zero surface tension, the bubble rise velocity  $w$  depends only on three parameters (Dumitrescu, 1943) as

$$w = \lambda \rho^p g^q R^r \quad (\text{A.16})$$

where  $\lambda$  is a dimensionless constant. In this case the  $\pi$ -theorem of Buckingham will lead to one (4-3) dimensional group. The physical units of all the variables are

$$[m/s] = [kg/m^3]^p [m/s^2]^q [m]^r. \quad (\text{A.17})$$

Balancing similar units

$$\left. \begin{array}{l} [m] : 1 = -3p + q + r \\ [s] : -1 = -2q \\ [kg] : 0 = p \end{array} \right\} \begin{array}{l} p = 0 \\ q = \frac{1}{2} \\ r = \frac{1}{2} \end{array} \quad (\text{A.18})$$

and substituting the result of equation A.18 in equation A.16 gives

$$w = \lambda \rho^0 g^{1/2} R^{1/2}. \quad (\text{A.19})$$

Hence,  $w$  is proportional to the square root of the radius and the gravity

$$w = \lambda \sqrt{gR}. \quad (\text{A.20})$$

The dimensionless number that can be obtained from equation A.20 is the Froude number defined by equation A.12. It is remarkable that the rise velocity of the bubble does not depend on the density of the fluid in which it rises.

---

## Appendix B

# User Defined Function

The User Defined Function (UDF) used to patch an initial bubble shape for the Dumitrescu bubble is given below. Details of the DEFINE\_INIT function can be found in the UDF manual of FLUENT. Note that the amplitude of the cosine function was arbitrarily chosen, but it should be large enough to have a curved bubble nose. Further, the diameter of the pipe (0.05 m) appears in the cosine function.

```
#include "udf.h"
#include "sg_mphase.h"
#define PI 3.141592654

/*****
/* UDF for initializing the bubble shape */
*****/

DEFINE_INIT(my_init_function , domain)
{
    Thread *t;
    Thread **pt;
    Thread **st;
    cell_t c;
    Domain *pDomain = DOMAIN.SUB_DOMAIN(domain , P_PHASE);
    Domain *sDomain = DOMAIN.SUB_DOMAIN(domain , S_PHASE);

    real xc[ND_ND] , y , x , z;

    mp_thread_loop_c (t , domain , pt)
    if (FLUID_THREAD_P(t))
    {
        Thread *tp = pt[P_PHASE];

        begin_c_loop (c , t)
        {
            C_CENTROID(xc , c , t);
            x=xc[0];
            y=xc[1];
            z=xc[2];

            if ( z < 0.005 + 0.05*cos(PI*sqrt(x*x+y*y)/0.05) )
                C_VOF(c , tp) = 1;
            else
                C_VOF(c , tp) = 0;

        }
    }
}
```

```
        end_c_loop (c,t)
    }

    mp_thread_loop_c (t, domain, st)
if (FLUID.THREAD_P(t))
{
    Thread *sp = st[S_PHASE];

    begin_c_loop (c,t)
    {
    C_CENTROID(xc,c,t);
    x=xc[0];
    y=xc[1];
    z=xc[2];

    if ( z < 0.005 + 0.05*cos(PI*sqrt(x*x+y*y)/0.05) )
    C_VOF(c,sp) = 0;
    else
    C_VOF(c,sp) = 1;

    }
    end_c_loop (c,t)
}
}
```

## Appendix C

# Analysis of the falling film around a Dumitrescu bubble

The analysis of Brown (1965) for a single large gas bubble that rises in a stagnant and viscous liquid will be discussed below. Consider figure C.1. The analysis of Brown applies to the fully developed film region, which is marked with a circle in figure C.1. Moreover, the flow in the film is assumed to be laminar. The density and the viscosity of the gas can be neglected. In addition the effect of surface tension is assumed to be small. These assumptions imply that there is no pressure gradient along the film and that the interfacial shear stress  $\tau_i$  is equal to zero. The material balance for the flow of the

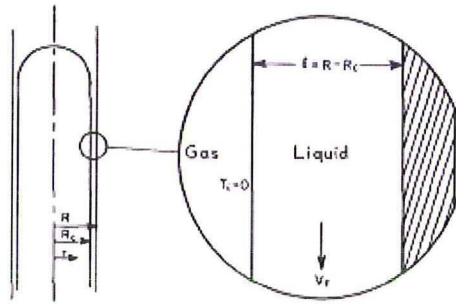


Figure C.1: *Equilibrium film (Brown, 1965).*

liquid in the film region relative to the bubble is given as

$$v_b R^2 = (v_b + v_f)(R^2 - R_c^2) \quad (\text{C.1})$$

or

$$v_b R_c^2 = v_f (R^2 - R_c^2) \quad (\text{C.2})$$

where  $v_b$  is the bubble rise velocity,  $v_f$  is the average liquid velocity in the film. The force balance on an element in the film is given by

$$\frac{1}{r} \frac{\partial(\tau r)}{\partial r} - \rho g = 0. \quad (\text{C.3})$$

Integration of equation C.3 from  $R_c$  to  $R$  gives

$$\tau r = \rho g \frac{r^2 - R_c^2}{2}. \quad (\text{C.4})$$

For laminar flow of a Newtonian liquid the shear stress can be expressed as

$$\tau = \mu \frac{dv_z}{dr}. \quad (\text{C.5})$$

Equation C.5 is substituted into equation C.4 and upon integration the velocity distribution in the film is obtained

$$-v_z = \frac{\rho g}{\mu} \left( \frac{R^2 - r^2}{4} - \frac{R_c^2}{2} \ln \frac{R}{r} \right). \quad (\text{C.6})$$

The average velocity of the liquid in the film can be obtained by integrating the velocity distribution across the film as

$$v_F = \frac{2}{R^2 - R_c^2} \int_{R_c}^R v_z r dr. \quad (\text{C.7})$$

Inserting equation C.6 into equation C.7 and integrating gives

$$v_F = \frac{\rho g}{\mu} \left( \frac{R_c^4}{2(R^2 - R_c^2)} \ln \frac{R}{R_c} + \frac{3R_c^2}{8} - \frac{R^2}{8} \right). \quad (\text{C.8})$$

Brown (1965) expressed equation C.8 in terms of the relative film thickness,  $\zeta = \delta/R$  and obtained

$$v_F = \frac{\rho g}{\mu} \frac{R^4}{(R^2 - R_c^2)} \left( \frac{2}{3} \zeta^3 (1 - \zeta) + \frac{1}{10} \zeta^5 + \frac{1}{60} \zeta^6 + \dots \right) \quad (\text{C.9})$$

Substitution of equation C.9 into equation C.2 gives the relation between the bubble velocity and the film thickness

$$v_b = \frac{\rho g}{\mu} \frac{R^2}{(1 - \zeta^2)} \left( \frac{2}{3} \zeta^3 (1 - \zeta) + \frac{1}{10} \zeta^5 + \frac{1}{60} \zeta^6 + \dots \right). \quad (\text{C.10})$$

Neglecting all terms of order greater than fourth gives

$$v_b = \frac{2}{3} \frac{\rho g}{\mu} R^2 \frac{\zeta^3}{(1 - \zeta)}. \quad (\text{C.11})$$

Furthermore Brown (1965) observed in his experiments that the frontal radius of the bubble, when the coordinates were normalized with  $R_c$ , was the same for the investigated liquids. Subsequently he showed that the bubble velocity correlates well by the equation

$$v_b = 0.496 \sqrt{g R_c}. \quad (\text{C.12})$$

Note that equation C.12 is a modification to the potential flow result of Dumitrescu (1943). Equation C.12 and equation C.11 both relate the film thickness and the bubble velocity. Hence eliminating the bubble velocity between these two equations gives the expression 7.4, in the main text, for the film thickness. Substituting this expression back into equation C.12 gives the bubble velocity equation 7.5 in the main text.

## P224 Multiphase Flow

### Exercise with Shell Flow Explorer

Note: conditions are the same as in the On-line Exercise number 3.

Oil and gas are transported in a pipeline with a diameter of 0.2 m and a hydraulic wall roughness of 0.06 mm. The pipeline can be assumed to be fully horizontal. At pressures of 50, 30, 20 and 10 bara the superficial gas velocities are 1.4, 2.4, 3.6 and 7.2 m/s and the gas densities are 35, 21, 14 and 7 kg/m<sup>3</sup>, respectively. The gas viscosity is 0.02 mPa.s. The liquid flows at a superficial velocity of 0.8 m/s and has a density of 800 kg/m<sup>3</sup> and a viscosity of 10 mPa.s. The surface tension is 0.025 N/m and the gravitational acceleration is  $g = 9.8 \text{ m/s}^2$ . Effects of condensation and evaporation can be neglected here. Also the acceleration contribution to the pressure gradient can be neglected.

- Use the SFE tool to calculate the flow regime, pressure drop, and liquid holdup for the 4 system pressures. Fill in the numbers in the table below.
- Compare SFE results with predictions using the homogeneous model and the Lockhart-Martinelli model. Explain the differences. Which model is most accurate and why?
- The 'manual' calculations of on-line exercise 3b assumed stratified flow for 10 bara pressure, which gave a liquid holdup fraction of 0.4 and a pressure drop of 111 Pa/m. Compare this with the SFE results. What happens if the superficial gas velocity is slightly increased from 7.2 m/s to 8 m/s. Explain the behaviour.
- Assume that the liquid volume fraction is fixed. Place the pipe with 10 bara system pressure under an upward inclination of 10 deg. What will happen with the liquid accumulation if the production rate is gradually decreased further and further. Same question for 10 deg downward inclination.

P bara	Homogeneous model		LM model		Shell Flow Explorer		
	liq. holdup alpha <sub>L</sub>	minus dp/dx Pa/m	liq. holdup alpha <sub>L</sub>	minus dp/dx Pa/m	Flow regime	liq. holdup alpha <sub>L</sub>	minus dp/dx Pa/m
50	0.36	88	0.54	247			
30	0.25	119	0.49	317			
20	0.18	155	0.46	381			
10	0.10	258	0.42	527			

